Alma Mater Studiorum · University of Bologna

School of Science
Department of Physics and Astronomy
Master Degree in Physics

A study of brain functional connectivity and cognitive processes in long COVID-19 patients

Supervisor:
Prof. Claudia Testa

Co-supervisor:
Dr. Micaela Mitolo

Submitted by:
Francesco Dalmonte

Academic Year 2020/2021

Abstract

In this work, a prospective study conducted at the IRCCS Istituto delle Scienze Neurologiche di Bologna (Bologna, Italy) is presented. The aim was to investigate the brain functional connectivity of a cohort of patients (N=23) suffering from persistent olfactory dysfunction after SARS-CoV-2 infection (so-called Post-COVID-19 syndrome), as compared to a matching group of healthy controls (N=26). In particular, starting from individual resting state functional Magnetic Resonance Imaging (rs-fMRI) data, different advanced analytical approaches were adopted in order to find potential alterations in the connectivity patterns of patients' brains. Analyses were conducted both at a whole-brain level and with a special focus on those brain regions directly or indirectly involved in the processing of olfactory stimuli (i.e. the Olfactory Network). Statistical correlations between functional connectivity alterations and the results of olfactory and neuropsychological tests were investigated, to explore also the associations with cognitive processes.
The three approaches implemented for the analysis were the seed-based correlation analysis, the group-level Independent Component Analysis (both investigating the correlation patterns of core Olfactory areas with the rest of the brain), and a graph-theoretical analysis of brain connectivity (implemented for both the whole-brain graph and for the olfactory network). Each of these approaches has been already applied in the context of rs-fMRI, but due to their relative novelty many implementation details and methodologies are not standardized yet, and currently represent active research fields.
Group-comparisons of the seed-based and group-ICA analyses' results showed no statistically significant differences between groups, while some relevant alterations emerged from the results of the graph-based analysis. In particular, patients' olfactory sub-graph appeared to have a less pronounced modular structure compared to the control group; locally, a hyper-connectivity of the right thalamus was observed in patients' Olfactory Network, with significant involvement of the right insula and hippocampus. Results of an exploratory correlation analysis showed a significant positive correlation between the graphs global modularity and the scores obtained in olfactory tests, consistently with the hypothesis that an impaired ability of segregating specific activities could negatively affect brain processes, and negative correlations between the thalamus hyper-connectivity and memory tests scores; this association could be interpreted in light of the critical importance of hippocampal-thalamic interactions for episodic memory.

Contents

Introduction

Different kinds of olfactory dysfunctions (ODs) were reported as some of the most characteristic early symptoms of SARS-CoV-2 infection. Moreover, in a considerable fraction of patients, OD is reported among its long-lasting effects, in the so-called Post-COVID-19 condition ("long-covid"). In these cases, ODs are often accompanied by a series of others neurological manifestations, ranging from various degrees of cognitive impairment, persistent headache, to fatigue and "brain fog", suggesting a general involvement of the Central Nervous System. This raises questions about the physiological mechanisms that underpin such symptomatology [1]. Actually, the neurotropic features of SARS-CoV-2 are not yet fully understood and it is not clear whether those neurological symptoms result from a direct viral invasion of tissues or from dysregulated and systemic inflammation [2]. Many efforts are being made in the study of these topics and works are continuously being published, addressing the clinical questions from different perspectives.

Neuroimaging has been extensively applied for this purpose, in order to detect potential brain-related abnormalities associated to the above mentioned symptoms and to help understanding the underlying pathogenesis. In particular, studies employing Magnetic Resonance Imaging (MRI) techniques offered important contributions; a recent study [3] combined the results obtained from MRI, DTI and task-based functional MRI (fMRI) investigations on a group of patients suffering from persistent COVID-19-related or generic post-infectious OD, to specifically address potential differences between the two groups in the brain structures involved in olfaction. In this study, structural and morphological differences were observed, as well as slight differences in the net trigeminal system's activity, highlighting some peculiarities of the COVID-19-related OD and suggesting an important role of olfactory bulb damage. Another study [4], involving a large number of patients with MRI examinations before and after subjects' infection, has revealed modest but significant structural and microstructural alterations (reduced grey matter thickness, reduction in global brain size and other markers of tissue damage), mainly affecting the limbic structures and the olfactory areas; such alterations could be signs of a possible degenerative spread of the disease through the olfactory pathways, of neuro-inflammation or also due to the loss of sensory-input due to the anosmia.

To date, studies focusing specifically on OD and symptoms of the Post-COVID-

19 conditions by means of fMRI techniques are few and with small cohorts of subjects, even though some interesting evidences were reported, suggesting possible impairment of the central olfactory pathway [5, 6]. In particular, the possibilities offered by resting state fMRI (rs-fMRI), in terms of fine-description of the general functional organization of brain, have not been fully exploited yet; with respect to fMRI, rs-fMRI could provide a more subtle characterization of the intrinsic connectivity patterns involving the brain regions that are related to olfaction, without limiting the analysis to the brain functional response connected to a specific task.

In 2021 such considerations inspired a study, conducted at the IRCCS Istituto delle Scienze Neurologiche di Bologna (Bologna, Italy), whose aim was to explore the integrity of the *Olfactory Network* - ON of a cohort of patients with COVID-19-related persistent OD. In particular, starting from structural and rs-fMRI examinations, a complete characterization of patients' brains from both a morphological and functional-connectivity points of view was obtained, with a special focus on the core-areas of the ON. Finally, results were integrated with individual neuropsychological profiles, in order to assess potential meaningful associations.
In this work the aspects of that study concerning the acquisition, the preprocessing and the analysis of rs-MRI data, for which I gave my personal contribution, are reported in detail. The goal of this part was two-fold: on one hand to localize and describe the ON from a functional-connectivity point of view in the available group of subjects, as a brain large-scale *resting-state network*; to date, only few (and quite recent) examples reporting this kind of attempts exist in literature, one of which was used as main reference for this work [7]; on the other hand, by comparing it with a matching healthy controls group, possible alterations in the patients' brain connectivity patterns were explored with different approaches of data analysis, requiring the application of some advanced methodologies.
The study of the brain's ON through rs-fMRI techniques presents a series of challenging technical difficulties due to its anatomical characteristics: olfactory core regions are in fact mainly sub-cortical, or placed near air-tissues interfaces of the frontal cortex (anterior- and Orbitofrontal-cortex), which are both critical positions for rs-fMRI-based examinations. For this reason high-quality raw data from a 3T scanner and high-performing sequences were required, as well as the adoption of a special pre-processing protocol employing the best noise-removal techniques available. The subsequent functional-connectivity analysis adopted three separated approaches, in order to give a range of perspectives on the experimental data set.

In the first Chapter of this work the phenomenology underlying the emergence of the BOLD signal and its measurement with MR techniques is briefly

presented, together with some details regarding the actual techniques currently employed for functional MRI. In Chapter 2 rs-fMRI data pre-processing and three of the possible approaches for the analysis of functional-connectivity patterns in this kind of data are discussed: the first one based on *Independent Component Analysis* of the signal, the second one based on a *seed-based* approach and the third one based on a *graph-theoretical* modelling of data. Further details about the clinical background and the motivations behind this study can be found in Chapter 3.
In the last three chapters the original experimental work is comprehensively presented. In particular, Chapter 4 describes the experimental materials and methods, Chapter 5 the relevant results obtained from the analysis and Chapter 6 the related discussion. Finally, the last section contains some final considerations about the limitations of the presented study and its future perspectives.

Chapter 1

BOLD signal magnetic resonance imaging

Functional Magnetic Resonance Imaging - fMRI is a non-invasive NMR-based imaging technique by which it is possible to indirectly map the activity of the brain. More properly, fMRI measures local hemodynamic changes after enhanced neural activity (exploiting the so-called *Blood-Oxygen-Level-Dependent* - BOLD signal) and uses this contrast to produce an image.
BOLD-fMRI is one of the main techniques used in cognitive neuroscience and related fields to investigate brain activity patterns; it is available in most hospital's MRI clinical scanners in which is used for both diagnostic and research purposes.
A typical BOLD-fMRI examination requires the acquisitions of a series of brain volumes, while the subject is at rest (rs-fMRI) or doing some particular task (task-fMRI). As a result, it will produce a time course of the fluctuations of tissues' MR signal, which can be indirectly linked to the actual neuronal activity. Even though it is not the only available technique to investigate human brain from a functional perspective, nor chronologically the first that was introduced, it certainly offers some exceptional and unique possibilities of investigation.
fMRI role in the description of the functional organization of the brain is somehow between those of PET/SPECT (which address the metabolic pathways of brain, following glucose metabolism) and EEG/MEG (which measure more directly the neuronal activity), offering a description of the so-called *hemodynamic response* to brain activity (see figure 1.1).
From a very general perspective, compared to PET/SPECT it has the advantage of being totally non-invasive (it doesn't involve ionizing radiation and doesn't need contrast agents or radiopharmaceuticals) and offers a higher spatial and temporal resolution; compared to EEG and MEG it has lower temporal resolution, but higher spatial resolution, allowing us to image the whole brain volume. However, each of these techniques has peculiarities making them "non-overlapping", and often they could bring complementary information (as in

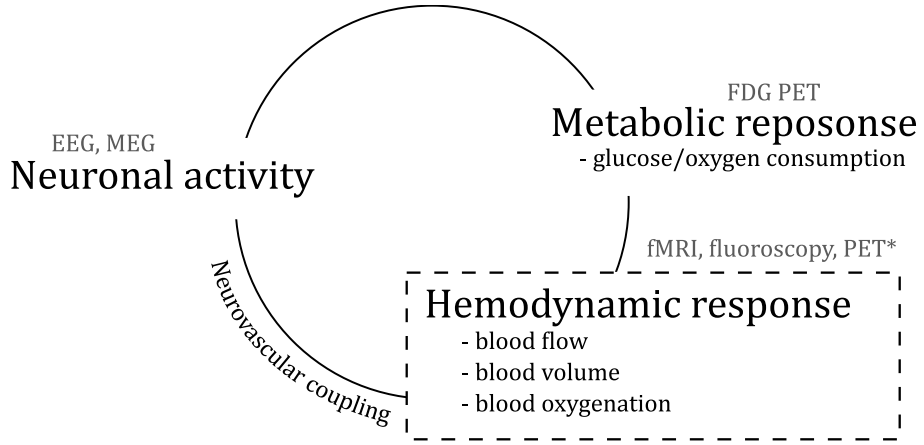

Figure 1.1: *Biological principles associated to some of the most common techniques for investigating brain activity. Functional-MRI offers a description of the hemodynamic response of the brain; it constitutes an indirect measure of the actual neuronal activity, to which it's related through the so-called neurovascular coupling.*

simultaneous EEG-fMRI experiments [8]).
In this chapter the fundamental neuro-physiological mechanisms connected to the emergence of BOLD signal will be introduced, together with the physical principles at the basis of its measurement and the sequences commonly used to acquire it.

1.1 MR-based measurement of brain activity

1.1.1 Brain metabolism

Information processing inside the brain is based on the coordinated activity of groups of neurons, which alternatively integrate incoming signals, and communicate a "response" (an outcome of the integrative process) to others groups. Both integrative and transmissive processes depend on a series of mechanisms that involve the active transport of charged ions across cellular membranes, such as creation and propagation of action potentials, or the exchange of neurotransmitters across synaptic gaps, and require a lot of energy to be carried out [9]. Activation of ions channels on external neurons' membrane in fact requires energy in the form of ATP, which in turn needs to be produced mainly through aerobic glycolysis (i.e. oxidation of glucose). Proportionally, for normal neural activity, brain tissue is metabolically incredibly expensive: weighting only about 2% of the body mass of a adult male human, it consumes up to 20% of oxygen and glucose body supply. On the other hand, differently from other high energy consumption-tissues such as muscles, brain tissue does not normally store glycogen inside, and then it constantly needs for blood from the vascular

system to supply oxygen (in the form of Oxyhemoglobin - HbO_2, in red blood cells) to produce glucose (from plasma). Furthermore, in order to make the energy supply efficient, the brain tissue is densely vascularized, with smallest capillaries size in the order of tens of micrometres.
Those considerations suggest that there should exists an important relation between local brain activity and the corresponding *haemodynamic response* - HR (i.e. arterial blood flow), and maybe that the latter could be used to localize and quantitatively measure brain activity: a first experimental observation pointing in this direction dates back to 1890, when the expansion of a dog's cerebral hemispheres (increase of *cerebral blood flow* - CBF, a condition known as *functional hyperemia*) was measured in association to stimulation of sciatic nerve [10]; many other observations of CBF increasing at a vessel scale were made in more recent years [11]. The mechanisms that trigger functional hyperemia are complex and still debated [12], but there is evidence that in first approximation CBF changes are correlated with both *Cerebral Metabolic Rate of glucose* - CMR_{glu} and *Cerebral Metabolic Rate of Oxygen* - $CMRO_2$, confirming the hypothesis that local HR is driven by brain activity.
However, while CBF and CMR_{glu} are almost perfectly coupled, many experiments [13, 14] have demonstrated a certain degree of uncoupling between CBF and $CMRO_2$ during local stimulation of brain regions: in particular the increase of CBF is not followed by a proportional increase of $CMRO_2$, resulting in a net increase of blood oxygenation level inside vessels. This imbalance have critical consequences, constituting the fundamental biophysical marker of brain activity for MR-based measurements; in this context the effect goes as *blood-oxygen-level-dependent* - BOLD signal.

1.1.2 BOLD signal

As the acronym suggests, BOLD signal basically depicts differences in blood oxygenation levels. It is possible to capture this contrast with MR measurements thanks to the magnetic properties of blood (hemoglobin in particular), which were discovered in 1936 by Linus Pauling (Nobel prize in 1955) with his student Charles Coryell. Oxygenated-hemoglobin (HbO_2) is in fact *diamagnetic* - no unpaired electrons in outer shell, while the de-oxygenated form (Deoxyhemoglobin- Hb) is paramagnetic - has unpaired electrons.
Having a significant magnetic moment, Hb slightly distort a surrounding magnetic field, affecting the spin-precession speed (*Larmor frequency*) of neighboring nuclei: from a MR point of view this means that the material will be characterized by a faster transverse magnetization relaxation (i.e. faster T_2 and T_2^* decay. See figure 1.2).
First measurements of differences in MR signals from in-vitro oxy- and deoxygenated hemoglobin samples revealed a clear dependence between $1/T_2$ constant and fraction of HbO_2 over Hb (as $1/T_2 \propto Hb^{-2}$), and no dependence between

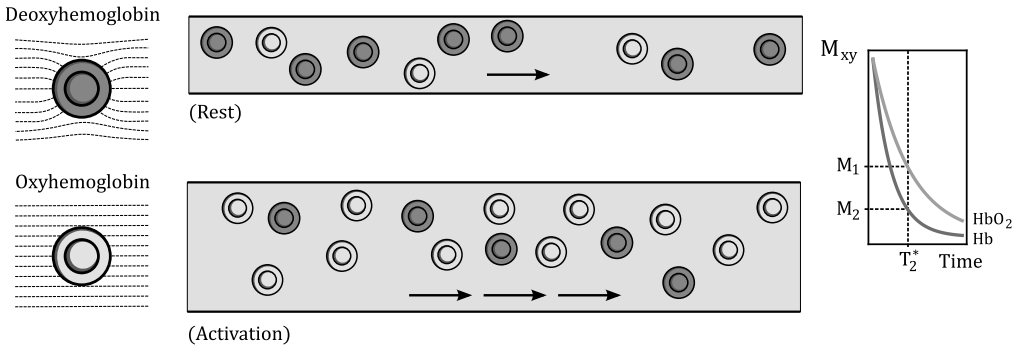

Figure 1.2: *Rest and active states of a vessel: in the active state blood flow and blood volume increase, as well as the concentration of HbO_2; due to the different magnetic characteristics of the Oxy- and Deoxy-hemoglobin, in the active state the net transverse magnetization experience a slower decay, so that for a fixed T_2^* the available signal is higher.*

$1/T_1$ constant (longitudinal relaxation time) and HbO_2/Hb [15]. Furthermore, a quadratic dependence between the increase of $1/T_2$ and the external magnetic field was demonstrated: for this reason BOLD signal is normally detected with high-field MR instruments ($\geq$ 1.5T).
These results inspired some important attempts of measuring such contrast in-vivo, e.g. [16], comparing MRI contrasts of vessels with blood at different levels of oxygen saturation, and then to the more ambitious goal of measuring the difference of saturation provoked by an increased brain activity (i.e. a BOLD signal) [17].
To sum up, BOLD signal originating from brain activity can be detected with appropriate MR measurements thanks to the dependence of parameter $1/T_2^*$ on the relative fractions of HbO_2 and Hb in blood; this relative abundance depends on the balance between consumption of oxygen and its supply from blood flow. As explained in the previous section, in presence of neural activity, the oxygen supply tends to exceed its consumption, increasing the fraction of HbO_2 over Hb, hence "flushing away" the major source of magnetic field inhomogeneity; this has the effect of increasing the $1/T_2^*$ parameter, and then of increasing the BOLD signal. Many experimental observations has proven the reliability of BOLD signal as an indirect measure of neuronal activity and the reproducibility of such a measure, and today it is at the basis of the most widely used techniques for brain activity measurements [18].

1.2 From BOLD signal to rs-fMRI

It has been shown how blood oxygen content affects the MR signal transverse component's decay rate; in particular, magnetic susceptibility of blood decreases as it becomes more oxygenated, affecting both T_2 and T_2^* relaxation processes:

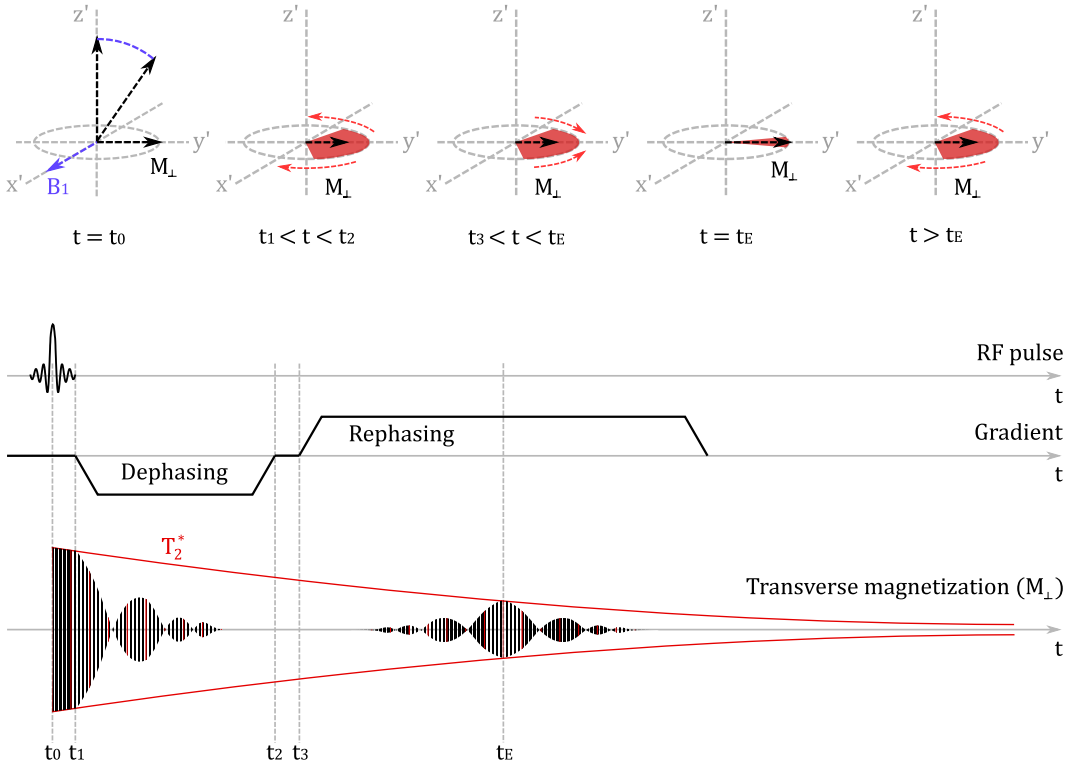

Figure 1.3: *Transverse magnetization change during gradient-echo formation. The "beat" pattern exhibited by M_{xy} when extra gradient is turned on is due to transient partial phase-coherent states of the spins.*

this dependence can be exploited in order to measure the BOLD signal.
In particular, for any practical purpose, T_2^*-weighted imaging is used, since it is more sensitive to oxygenation changes by at least a factor of 2 to 4; this is mainly because T_2^* contrast is affected by field inhomogeneities from small to large spatial scales, while Spin-Echo T_2 BOLD signal predominantly originates from small-sized ones [1][19, 20].
The most common acquisition sequence for T_2^*-weighted BOLD-fMRI is the *Gradient Echo* (GE) *Echo Planar Imaging* (EPI), by which it is possible to acquire a whole-brain volume in a fraction of a second.

1.2.1 GE-EPI sequence

Gradient Echo mechanism

Gradient Echo (GE) sequence is based on the application of an initial small flip angle pulse ($\leq 90°$) and the simultaneous application of a gradient, by which

[1] T_2 contrast relies on diffusion of protons across inhomogeneities: for the extravascular component of the signal this effect is larger near small vessels, but smaller near large venules, where susceptibility gradient is "smoother" then dephasing effect is partially refocused.

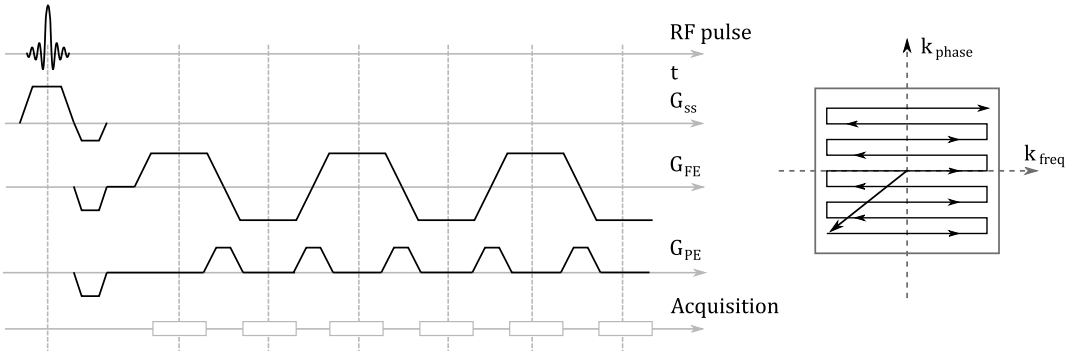

Figure 1.4: *Left - Blipped GE-EPI temporal sequence temporal scheme. Right - Sampling of the k-space, performed by sequential applications of the phase-encoding gradient while alternating the phase-encoding direction.*

it is possible to generate an echo of the initial transverse magnetization. An important difference with a spin echo sequence is that dephasing of protons occurs as a result of T_2^*-decay rather than a T_2 decay process, and is susceptible to static field inhomogeneities.
With respect to spin echo, GE acquisitions are much faster because longitudinal magnetization component is never inverted, then a smaller recovery time is required (shorter TR). In particular, when using small flip angles, one has the advantage that the amount of transverse magnetization gained is much greater than the longitudinal (i.e. as the flip angle get smaller, the transverse/longitudinal magnetization ratio increases).
Figure 1.3 summarizes how a GE sequence works: at t_0 an RF pulse with flip angle $\leq 90°$ excites the sample, so that longitudinal magnetization is partially tilted and a transverse magnetization is created; hydrogen spins precess at slightly different speeds, then the transverse magnetization starts to decrease (following a T_2^* relaxation, i.e. in a *free induction decay* - FID regime); at t_1 an extra gradient is applied, accelerating the dephasing process, until t_2, when no net transverse magnetization is left and the gradient is switched off; at t_3 an inverse gradient is applied (same magnitude and direction, opposite polarity), with the effect of restoring an aggregate transverse magnetization, so that an attenuated echo of the initial signal can be measured.
The main reason why GE is used in BOLD-fMRI sequences is that it allows to acquire T_2^*-weighted images (i.e. sensitive to magnetic field inhomogeneities and magnetic susceptibilities differences) with a very short TE (echo time), which in turn means that overall TR can be reduced, while keeping a relatively high SNR; clearly, in any functional-imaging modality reduction of TR is of crucial importance, since it directly determines the temporal-resolution of the sequence.

EPI acquisition

Even though GE sequence can offer very short TRs, in order to acquire entire 3D brain volumes in a fraction of a second an optimized image sampling approach must be adopted. The so-called *turbo* or *fast* sequences allow to collect multiple k-space rows per single RF pulse excitation. With the *Echo-Planar Imaging* (EPI) modalities it is possible to sample the entire k-space (i.e. an entire 2D MR slice) with a train of echoes following a single initial RF pulse stimulus.
A schematics of one of the most common EPI sequences is reported in figure 1.4 (commonly known as *blipped*-EPI). After the slice-selective RF excitation pulse, and after the rephasing lobe of the slice selection gradient (G_{ss}), a train of echoes is generated through an oscillatory gradient along the frequency encoding direction (G_{FE}, which in this case is actually the *readout* gradient), which alternately dephase and rephase the set of spins in the sample. During each G_{FE} inversion, a very short-lasting phase encoding gradient (G_{PE}, "blip") is applied, so as to shift the current sampling position along the phase-encoding direction. At the end, in practise k-space sampling is obtained by following a *zig-zag* trajectory, travelling frequency-encoding direction alternately in opposite directions, and skipping to the new line at each *blip* of the G_{PE}.

1.2.2 Spatial and temporal resolution

Fundamental parameters to be chosen for an fMRI experiment are the spatial resolution and the acquisition rate (or temporal resolution, which corresponds to TR - time for the acquisition of a single brain volume), depending on the particular requirements of the situation.
When using EPI techniques, TR directly depends on the number of slices forming a brain volume and on the the time each slice takes to be acquired in the EPI sequence; the latter is mainly determined by how rapidly gradients can be switched on and off, by how fast is the ADC and by the TE (echo time) one chooses to use.
In the context of BOLD-fMRI optimal TE is about 20 to 40 ms (equal to the T_2^* of tissue). Considering the time needed for the rest of the sequence, one single slice of volume can be acquired in 50 to 100 ms, allowing ten to twenty slices per second. Considerable improvements were made possible by the use of parallel imaging approaches [21, 22] and more recently by *multi-slice* (or *multi-band*) techniques (which simultaneously excites multiple slices by means of a single composite RF pulse, and then separate signals during image reconstruction [23]).
Nowadays fMRI examinations can reach TR of less than 1s at 3T, allowing a finer temporal sampling and, as a consequence, more effective noise removal.
On the other hand, spatial resolution is mainly determined by magnetic field gradients strength, digitizing rate and the time available before complete signal decay, which clearly is much more important in the case of EPI sequences,

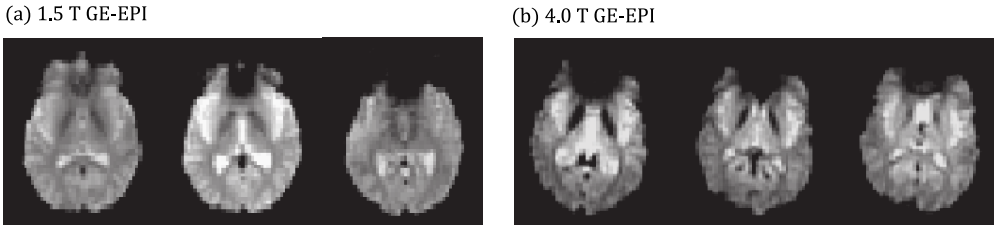

Figure 1.5: *Signal loss artifact due to magnetic susceptibility of air-tissue boundaries in the ventral frontal lobes, at different field strengths. Notice that this kind of artifact get worse for increasing field-strength.*

rather than "multi-shot" imaging methods (for this reason usually EPI images are characterized by a lower spatial resolution). However, with multi-band and parallel imaging techniques, also EPI images can reach a voxels size as small as 1 mm^3; common resolutions with 3T scanners are 2 to 3 mm^3.

1.2.3 Image quality and artifacts in fMRI

EPI artifacts

The quality of EPI images can be severely compromised by the presence of characteristic artifacts, which mainly originate as a consequence of field or gradients inhomogeneities when no proper *shimming* (adjusting with additional fields) is provided.
In particular it is worth mentioning the two main types of artifacts: geometrical distortions (spatial shifting of voxels in the image reconstruction) and signal losses, which are usually due, respectively, by small- and large-scale field inhomogeneities. Larmor frequencies of protons in fact directly depend on the magnetic field strength they experience, and since the position of a voxel in the image is encoded by its frequency, a voxel with incorrect resonant frequency will be displaced to an incorrect position; on the other hand, when there is a relatively long time between slice excitation and signal acquisition, magnetic field inhomogeneities can make spins inside a voxel accumulate different amounts of phase, leading to MR signal loss (see the example reported in figure 1.5).

Such artifacts are commonly observed in brain regions that are close to an air-tissue boundary (such as *ventral frontal lobes* and *inferior medial temporal lobes*, because of nasal, oral and auditory cavities) due the difference between air and tissue magnetic susceptibilities, which cause field distortions.
Solutions to these problems include: providing a better static field shim, mapping the static field to perform a correction based on this map, or try some kind of corrections after the image is reconstructed.

SNR and sources of noise

BOLD-fMRI experiments rely on very small and transient (but meaningful) changes in a signal which is affected by a high spatial and temporal variability. Part of such variability is due to inherently random causes, such as scanner or patients thermal fluctuations, while another part is typically due to physiological effects that could be temporally and spatially correlated with the "true" signal, making it more difficult to get rid of. Typical sources of potentially correlated noise are: imperfections in scanner hardware, patient head motion, physiological processes such as respiration and heart beat.
Increasing the static field strength directly increases the amount of net magnetization in the sample, hence increases the detected signal, but simultaneously amplifies artifacts and makes inhomogeneities harder to correct. For these reasons a series of appropriate pre-processing steps on the reconstructed images are always required, targeting specifically each source of noise and artifact. More details on this topic will be given in the next chapter.

Chapter 2

Analysis of rs-fMRI data

The first fMRI studies adopted so-called *task-induced* protocols, meaning that they focused on responses in the BOLD signal as induced by a task performed by the subject [24]. In typical task-induced examinations, a simple and short task (e.g. finger-tapping) is performed by the subject multiple times during the acquisition time, then the BOLD signal measured during the task is compared with baseline signal measured at rest.
Resting state-fMRI (rs-fMRI) is a more recent trend in functional neuroimaging and consists in observing human brain activity when the subject is awake and not performing any particular task.
From the point of view of the MR acquisition, apart from the task-protocols, task-fMRI and rs-fMRI do not differ much, but subsequent data processing and analysis methods are essentially different.
In typical rs-fMRI the examined brain is supposed to be in a "stationary" state [1], where distinct brain regions, rather than being totally silent, show a weak but coherent (i.e. temporally similar) low-frequency BOLD signal fluctuations. The similarity of their signal time courses can be considered a measure of *functional connectivity* (FC). The choice of the metric used for quantifying the similarity between two time courses clearly has a fundamental importance for the interpretation of the results. Resting-state FC between specific anatomical regions was shown to be so reproducible (*between-* and *within*-subjects) that inspired the definition of so-called independent *resting-state networks* (RSNs), which can be isolated from the whole-brain signal. RSNs have been extensively studied and accurately described [26], and offer an opportunity to compare functional organization of different subjects brains.
Analysis of rs-fMRI data can follow different approaches, among which the most widely used are the seed-based correlation analysis (SBA, based on a strong *a priori* assumption about the spatial localization of a region of interest for

[1] in recent years some studies have investigated the hypothesis that a non-static behaviour could be observed even in conventional rs-fMRI experiments [25]; however, there is general agreement that trends in functional connectivity are a "higher order" effect, and the stationary hypothesis is appropriate for most of the cases.

the network) and the independent components analysis (ICA, a data-driven approach); often research experiments aim to highlight some group-based differences between cohorts of subjects, thus require additional steps for making data comparable.
In this chapter both the fundamental steps typically required for rs-fMRI data preparation and standardization (pre-processing) and some different approaches that can be applied for subsequent data analysis will be presented.

2.1 Pre-processing and denoising techniques

Data preparation in rs-fMRI is the set of procedures performed after the acquisition and before the proper data analysis. Such procedures include corrections directly related to the acquisition method, true *de-noising* of data, and often (as in the case of cohort-studies, when average characteristics of groups of subjects are compared) *registration* of brain volumes to a standard space (MNI-ICBM152 brain template [27]).
As it was already mentioned, due to the intrinsically low effective SNR of raw BOLD-fMRI data, the application of an appropriate and targeted series of denoising steps can drastically affect the quality of data; for this reason, at least the very first part of such procedure is essentially standardized.
Common correction and de-noising steps include:

1. **Correction for slice-timing differences** - as shown in figure 1.4, acquisition of each slice of the brain volume is performed separately, hence at slightly different times. In order to virtually "synchronize" the acquisition time-points, a temporal interpolation of the signal from each voxel at common time-points is performed.

2. **Correction for head motion** - patient's head motion during acquisition time is one of the main problems for fMRI studies, and if not adequately corrected can considerably worsen signal spatial resolution and eventually lead to incorrect results [28]. Head motion can be partially prevented by carefully instructing the subject, by maximizing their comfort and through some sort of head restraints; residual motion is corrected by spatially aligning all the image volumes to a single reference volume (usually the first or the central acquisition time-point). Co-registration is usually performed by fitting the parameters of a rigid-body transformation through a cost function minimization.

3. **Spatial filtering** (low pass) - 3D spatial smoothing of each brain volume has been demonstrated to increase SNR; in particular, there is evidence that at higher fields ($\geq 3T$) it is convenient to collect high-resolution data and then perform spatial smoothing rather than acquiring at lower

resolution [29]. Usually spatial smoothing is performed by applying a Gaussian filter of FWHM $\approx 4mm$ to $8mm$ (i.e. approximately expected activations extent).

4. **Temporal filtering** (band-pass) - the use of temporal filters on each voxel's time series can substantially improve the quality of the acquired data: BOLD signal is in fact characterized by predominantly low frequency fluctuations ($0.01 - 0.1$Hz, with minor higher components), while physiological noise spectrum is usually centered at higher frequencies (e.g. cardiac $1.0 - 1.5$Hz and respiratory ($0.3 - 0.5$Hz), then they can be isolated by the application of a low-pass filter. Usually a high-pass filter is also used in order to remove the presence of slow hardware/scanner related drifts or apparent aliased signal generated by physiological noise with frequency similar to the acquisition rate [30].

Other denoising approaches have been developed in recent years, trying to more precisely address structured noise and the well-known artifacts which typically affect functional images, and concurrently preserving true signal. For example, for physiological artifacts, it is possible to exploit external recordings of the physiological state, and then retrospectively regressing out those components from the total signal. However, since this kind of monitoring is usually not available, fully data-driven approaches are required: one of the most effective examples of such techniques is based on *Independent Components* signal decomposition [31], which will be presented in the next section.

2.1.1 ICs signal decomposition-based data denoising

ICA - Independent Component Analysis

ICA formally refers to a class of *latent variable* models, commonly used for the linear decomposition of a multivariate signal into maximally independent components (*blind source separation* problems) [32, 33]; similarly to Principal Component Analysis, ICA provides a new representation for the data (i.e. a new vector basis) through a linear transformation, but maximizing the statistical independence of the components rather than minimizing their mutual correlation [34]. In fMRI context ICA algorithms are used to separate independent components of 4D data (3 spatial dimensions and time) each characterized by a 3D spatial map and a common time course.
Classical ICA algorithms (such as in [35]) assume a decomposition of fMRI data $t \times n$ matrix X (t is the number of timepoints, n is the number of voxels of a single brain volume) such that

$$X = A\,S \tag{2.1}$$

Where S is a $t \times n$ matrix in which each row identify a statistically independent spatial map of the brain, and A is a $t \times p$ matrix containing characteristic

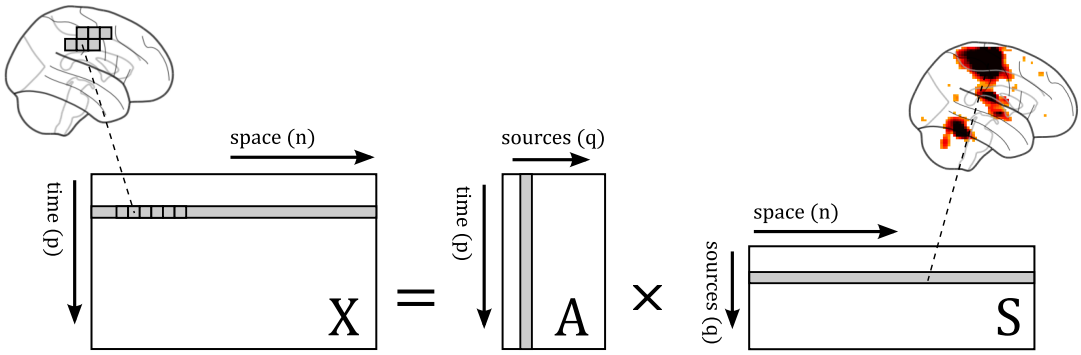

Figure 2.1: *Classical ICA decomposition scheme: an initial 4D signal is reshaped onto a 2D matrix (p timepoints × n voxels); ICA decomposes it as a set of q statistically independent components, each one characterized by a spatial map (represented in the 2D matrix S) and a time series (represented in the 2D matrix A).*

time courses of each independent map as column vectors (*mixing matrix*). ICA goal is then to estimate an *unmixing matrix* $W = A^{-1}$ so that $S = W\,X$ has independent rows, by means of an iterative optimization algorithm (e.g. *infomax* algorithm). In figure 2.1 the classical ICA main idea is illustrated with a simplified scheme.

The model presented above is the simplest possible, but has two important limitations: first, the mixing matrix is constrained to be squared (i.e. the number of independent components is equal to the number of time-points); and second, there is no explicit assumption for the presence of pure noise components (data is assumed to be completely characterized by estimated spatial maps and mixing matrix). For practical implementations then, a more sophisticated model called *Probabilistic*-ICA (PICA) [36] is employed.
PICA assumes that the original signal measured in i-th voxel can be represented as a p-dimensional vector

$$x_i = A\,s_i + \mu + \eta_i\ , \qquad \eta_i \sim \mathcal{N}(0,\, \sigma^2 \cdot \Sigma_i) \tag{2.2}$$

with s_i representing the q-dimensional vector of the independent signal components contained in data from i-th voxel, η_i representing the Gaussian noise and μ the average signal of x_i. Covariance of the noise is assumed to be voxel-dependent for generalization. Then similarly to the previous case, solving the blind separation problem correspond to find the *unmixing* matrix W such that

$$\hat{s} = W\,x \tag{2.3}$$

is a good approximation for the real signal s.
In practical implementations of PICA (such as MELODIC, released as part of

the FMRIB Software Library) data is required to be normalized to unit noise variance before estimating the unmixing matrix, and noise covariances Σ_i are obviously not known in advance; for this reason, original data is iteratively split into noise and signal sub-spaces through PCA application, and normalized according to the progressively more accurate estimation of noise component. Further details on ICA decomposition algorithms and implementations can be found in [34, 36, 31].

Classification of artefactual components

In the context of rs-fMRI, at single subject-level, ICA was proven to be a powerful tool for artifacts removal during data pre-processing, for its ability to separate true neural signals from many different sources of stochastic or structured noise as distinct independent components (ICs). In practice there are at least two ways in which ICA decomposition could be exploited for noise removal: to select "good" ICs (representing true neural signal) and sum them to reconstruct true-global signal, or to select "bad" ICs (artifactual and noisy components) and regress them out from the starting data (the latter being considered the most conservative approach, hence the most common) [37]. However, independently from the denoising approach, each IC resulting from the decomposition must be classified as signal (S-IC) or noise (N-IC) based on its spatial map and its average time course (examples of "good" and "bad" components, as they can be observed by running the ICA decomposition for a subject, are reported in figure 2.2 and 2.3).
Classification of noise components can be performed by hand but requires expert knowledge about BOLD signal typical spatial and temporal characteristics, about noise and artifacts peculiarities as well as neuroanatomy and physiology notions; in practice this means that the procedure is strongly time-consuming and can be operator dependent if no adequate training is provided.
In recent years many publications addressed the problem of giving objective guidelines for hand classification in order to make results reproducible, such as [38], [39] and [40]. In general there is agreement that a classification based on visual inspection of spatial maps (e.g. activation peaks must be in gray matter tissue, activation should not present alternating slices or alternating positive and negative scattered peaks), inspection of characteristic time series (e.g. should not contain sudden oscillations) and of its power spectrum (e.g. must contain mainly low-frequency signal), together with the knowledge of the most common noise components characteristics, can guarantee good cleaning results, removing most of the artifacts while preserving the original true signal. Clearly, there is high interest in the automation of such procedure with classification algorithms, and a number of tools have been developed (FMRIB's ICA-based X-noiseifier (FIX) [41]), reaching high levels of accuracy, even though the gold-standard remains hand classification.

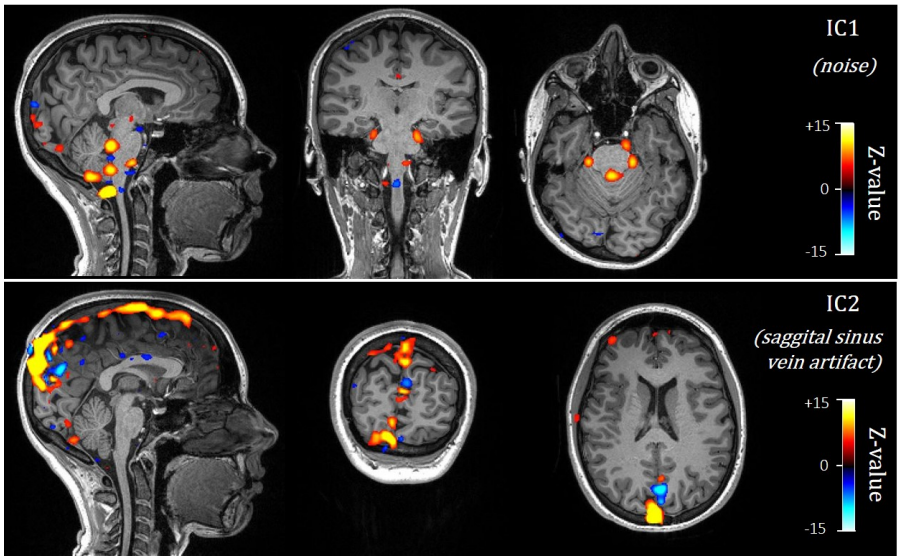

Figure 2.2: *Examples of two artifactual ICs, produced by applying MELODIC ICA decomposition on a subject's real data (intensity threshold at* $|Z| > 3.1$*). Component IC1 (top) cannot represent true neural signal, as the peaks of intensity do not overlay with grey matter, or are even outside the brain volume. Component IC2 (below) is a typical example of signal produced by the large vein in the superior sagittal sinus, which is a very common artifact. In these figures the power-spectrum and the time course of each IC, which are also examined in order to classify the components, are not reported for simplicity.*

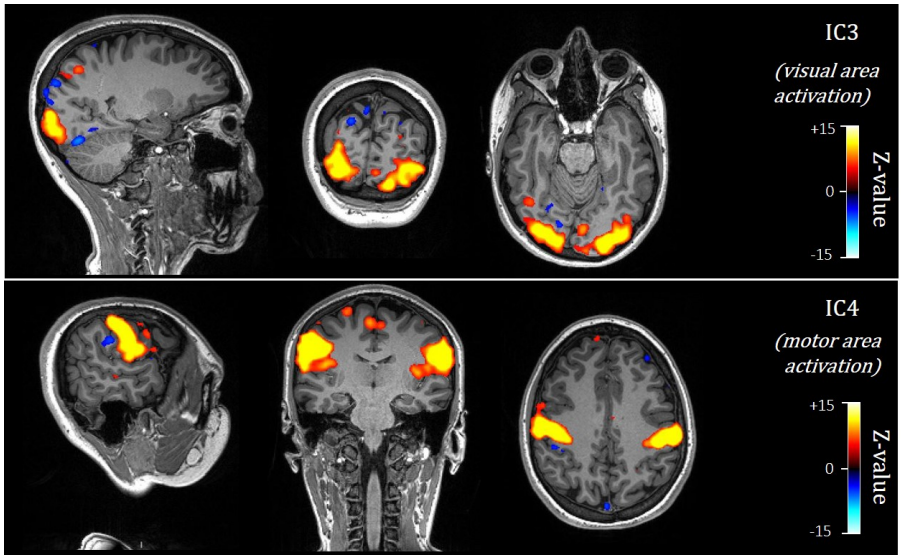

Figure 2.3: *Example of two ICs representing true neural signals, produced by applying MELODIC ICA decomposition on a subject's real data (intensity threshold at* $|Z| > 3.1$*). Peaks of intensity are placed on gray matter and well-represent a bilateral correlation between regions of the motor cortex.*

2.2 ICA-based approaches and Dual-Regression

Generally speaking, rs-fMRI experiments are focused on observing correlation patterns within the brain or specific parts of it, and eventually compare them with other subject's data. Data analysis, once pre-processing and noise removal steps are performed, can follow different approaches depending on the particular aspects one is interested in and on the prior hypotheses that are done.
ICA-based approaches are examples of fully data-driven methods for the investigation of whole-brain correlation patterns, interpreted as functional connectivity. In fact, when ICA is performed on cleaned data from a single subject, and in particular when the number of ICs components is limited (20 to 100 components), it is possible to identify among those components functionally connected networks, and eventually recognize them as portions of or entire RSNs. The number of ICs (*dimension* of the ICA) is an important parameter which indirectly determines the scale of the networks that will be observed: by using a small number of components, each IC will bring a larger portion of the total signal variance, so larger networks will be returned (more rough description of the connectivity patterns), while by using a very large number of components it is more probable to end up with RSNs divided into different sub-components.
ICA can be exploited in the frame of group-studies, when different cohorts of subjects are compared, by running a single ICs decomposition on the temporally-concatenated data from all the subjects of a group at the same time. This technique is known as *group*-ICA (or *concat*-ICA, see figure 2.4), and allows the identification of common ICs spatial-maps for the whole group; in this way it is possible to obtain more robust ICs maps for each cohort and to make formal statistical testing of group-differences between correspondent ICs.
One way to do this is with a so-called *dual-regression* analysis [42, 43], in which:

1. group-specific ICs are used as spatial regressors to extract subject-specific characteristic time series associated to those maps.
   By calling $Y \in R^{n \times t}$ the 2D matrix of a subject's time courses (n voxels, t timepoints), $\hat{S} \in R^{n \times m}$ the set of group-level ICs spatial maps (m components), $E_1 \in R^{n \times t}$ the errors matrix, then $\hat{S}$ are the predictors in a multivariate linear regression such as

   $$Y = \hat{S} \cdot B_{TC} + E_1 \tag{2.4}$$

   where $B_{TC} \in R^{m \times t}$ is the matrix of the subject's time courses associated to each IC map.

2. these subject-specific time courses are used then as a set of temporal regressors to find subject-specific maps associated to the group-level ICs. This second regression reads

   $$Y = \hat{B}_{TC} \cdot B_{SM} + E_2 \tag{2.5}$$

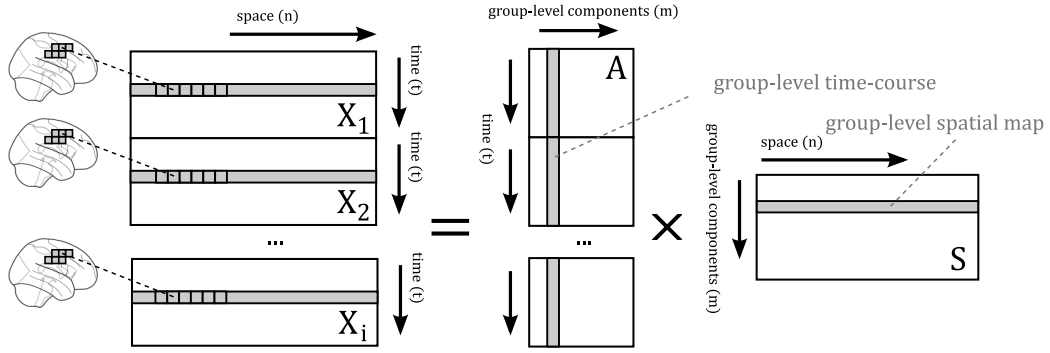

Figure 2.4: *Group-ICA analysis scheme: individual EPI volume sequences are registered to a common space and temporally concatenated (X_1, X_2 ... X_i); ICA is performed on the total sequence; common (group) ICs spatial maps are identified (in matrix S), and can be used for subsequent analyses (e.g. a dual-regression analysis, for obtaining subject-specific maps associated to the group-level ICs).*

where $\hat{B}_{SM} \in R^{n \times m}$ will contain the estimated spatial maps corresponding to each group-level IC.

With the set of subject-specific spatial maps it is then possible to test for group-differences at voxel level.

2.3 Seed-based approaches

A different and conceptually simpler type of commonly used approaches, are the so-called *seed-based* approaches, which focus on the functional connectivity between one or more *Regions of Interest* - ROIs (or *seeds*) and the rest of the brain. A seed-based correlation analysis hence requires the *a priori* definition of the ROIs (which can be either anatomical regions or spherical seeds), making it in general more dependent on prior assumptions with respect to ICA-based methods.

In practice in a seed-based analysis the time series of all the voxels inside a ROI are averaged to obtain a characteristic time course of the region; then this data are used as a regressor in a linear correlation analysis (or in a General Linear Model - GLM) in order to calculate voxel-wise functional connectivity maps of covariance with the selected ROI (for this reason is sometimes called seed-*voxels* correlation analysis); the result is then a whole-brain connectivity map indicating how strongly each voxel is functionally associated to the seed region. Seed-based approaches have been largely used for revealing intrinsic connectivity patterns of specific brain regions, and were demonstrated to be highly reliable methods [44].

With respect to ICA-based approaches, seed-based connectivity analysis addresses the functional connectivity of specific ROIs, rather than giving infor-

mation about whole-brain intrinsic functional networks, making it a valuable solution when one is interested in a more direct and focused analysis of the connectivity of a specific brain region.
For group-level comparisons, different methodologies may be adopted, as a statistical comparison between two sets of subject-specific spatial maps of correlation coefficients may be differently implemented [45]. A common approach is to convert the individual correlation maps to Z-statistics and submit them to a GLM to fit a previously specified model, followed by a hypothesis testing.

2.4 Graph-based analysis

Graph-modelling of brain functional networks exploits concepts from graph-theory to explore and describe its organization. With respect to those introduced in the last sections, graph-approach presents further levels of complexity from the implementation point of view, as well as for the interpretation of results, but can also offer a richer description of the organization of the brain.
In order to implement a graph-based analysis of rs-fMRI data a series of assumptions must be made, starting from the definition of the nodes and links of the graph itself.

2.4.1 Definitions

A graph is defined by a number of *nodes* (or *vertexes*), variously connected by *links* (or *edges*). Each link can be characterized by a strength (or *weight*; in this case the graph is said to be *weighted*), and can be undirected or directed (whether the links can be travelled in both directions or not); in graph-modelling of the brain nodes are usually imagined as concrete and delimited volumes of brain, while links describe the functional connectivity between them (therefore will essentially depend on the BOLD signal associated to the nodes).
The definition of nodes depends on both the scope and the data available in the particular experiment for which the analysis is required. One could think that the most natural choice would be to take each single rs-fMRI voxel as an independent node of the graph, but even with a relatively low data resolution this would inevitably bring to a very large graph (making each operations computationally expensive) and based on less significant data (due to the typically low SNR of BOLD signal). In practice the simplest choice is to define nodes as spherical volumes centered in specific meaningful positions of the brain (with radius depending on resolution and effective SNR of the data); more effective choices are based on pre-defined brain parcellations (based on either functional, structural or simply anatomical atlases) or on parcellations computed from the data itself through clustering algorithms [46, 47].
The definition of links reflects the important assumptions made about the con-

cept of functional connectivity: how is it defined and how can be quantified. The most common choice is to define functional connectivity between two nodes as the full Pearson's correlation coefficient between the two characteristic time series (defined as the average time course of the voxels belonging to each node), which quantifies a linear time-domain dependency; this approach has the advantage of being rather simple, computationally fast and experimentally was shown to give solid and reliable results [48]. Furthermore, the most common choice when using full Pearson's correlation is to neglect the potential negative values of correlation, and treat them as zeros, as their interpretation is unclear but there exists evidence that they could be linked to statistical artifacts or emerge from certain steps in data pre-processing [49]. Many other approaches have been studied and discussed, such as partial Pearson's correlation, methods based on Wavelet decomposition, Mutual Information, Euclidean distance or Dynamic Time Warping; in general results obtained with different functional connectivity definitions should not be considered as comparable, but there is evidence that all the previous metrics results are consistent, and none of those in general clearly outperform the others [50]. Some studies have suggested the possibility that a combination of different metrics, based on different definitions of connectivity, could give a meaningful and more complete description [51].
From a mathematical point of view, a graph can be represented by its *adjacency matrix*, i.e. a square matrix in which the value of element (i, j) will represent the strength of the link (the weight) between i-th and j-th elements (so that binary graphs will be described by binary adjacency matrices and undirected graphs by symmetric matrices). A different, hence equivalent, graph representation is the so-called *incidence matrix*; in this case rows are associated to the nodes of the graph, and columns to its edges: (i, j) element value indicates the connection of j-th link to the i-th node (each column will always contain two non-zero values). In the next chapters of this work, graphs will be always represented through their adjacency matrices.

2.4.2 Graph properties

Once a graph is defined, it is possible to describe many aspects of its topological organization through the evaluation of specific *global properties* (or *measures*); on the other hand, *local properties* can help characterizing the role of each node in the network. In this section some of the most relevant properties for the graph-modelling of brain functional networks are illustrated [52].
The most basic (local) property of a graph is the *degree*, defined as the number of links connected to a certain node, or equivalently the number of *neighbors* of that node. The distribution of the degrees of the nodes in a network is a first global-level property which can help characterizing the graph, together with the *Giant-Component Size* for disconnected graphs (i.e. the size of the largest connected component of a graph); the global property defined as the average

value of such a distribution is usually called *density* of the network. In weighted graphs nodes' *strength*, i.e. the sum of the weights of all the links connected to the node, is usually more relevant than degree, but conceptually analogue.
Other neurobiologically meaningful measures are listed below[2].

- **Properties of integration**
  According to M. Rubinov and O. Sporns, *functional integration* for a brain network can be described as "the ability to rapidly combine specialized information from distributed brain regions" [52], implicitly assuming that nodes of a graph are conceptualized as entities exchanging *information* through the links they're connected to; consequently, the measures addressing functional integration are based on the *paths* which can be built by joining sets of links. Paths are then naturally characterized by their length, considering inverse of the weight of a node as its individual length.
  Notice that, despite the intuitiveness of those definitions, in the case of functional connectivity graphs, links represent a kind of correlation between neural activity of two brain regions rather than an effective flow of information, then measures of integration should be interpreted accordingly.
  The most important global measure of integration is the *Characteristic Path Length*, defined as the average length of the shortest paths between every pair of regions of the brain; the average of the inverse length of shortest paths is usually called *Global Efficiency*.
  For the purposes of this work Characteristic Path Length of a graph was defined as
  $$CPL = \frac{n(n-1)}{\sum_{i \neq j} d_{ij}^{-1}} \tag{2.6}$$
  where $d_{i,j}^{w}$ is the i-j weighted shortest path length; Global Efficiency is defined as its inverse.

- **Properties of segregation**
  Brain *functional segregation* is the ability of isolating specialized processing within densely interconnected bundles of nodes. The presence of highly separated clusters of nodes, or a well-defined modular structure in functional networks suggests an organization of statistical dependencies indicative of segregated neural processing.
  Clustering Coefficient is a local property defined as the number of triangular structures that can be drawn in the neighborhood of a certain node (or equivalently, the number of a node's neighbors that are also neighbors of each other), normalized by the node's degree [53]. Globally, the average Clustering Coefficient of a graph reflects the prevalence of clustered connectivity around nodes; notice that due to the normalizing factor on

[2] here we focus on the case of weighted networks; for binary networks definitions are usually equivalent, considering all the links weights equal 1.

the denominator, Clustering Coefficient could be disproportionally higher in the case of low-Degree nodes.
Clustering coefficient can be computed as

$$C = \frac{1}{n} \cdot \sum_i \frac{2t_i^w}{k_i^w \left(k_i^w - 1\right)} \tag{2.7}$$

where n is the number of nodes in the network, k_i^w is the i-th node's Strength, and t_i^w represents the number of triangles that can be built around i-th node (weighted according to their internal links weights). A more sophisticated global measure of segregation is *Modularity*, which quantifies how well a graph can be subdivided into separated modules (groups of nodes highly interconnected between each other, with few outwards connections). Modularity coefficient is usually computed as

$$Q = \frac{1}{m} \cdot \sum_{i,j} \left[w_{ij} - \frac{{k^w}_i \, {k^w}_j}{m} \right] \delta(c_i, c_j) \tag{2.8}$$

where m is the sum of weights in the graphs, w_{ij} is the weight of i-j link, c_i identifies the module containing i-th node. Modules must be estimated through optimization procedures; one of the most famous (and most computationally efficient) algorithms for community detection is the so-called Louvain method [54].
A local-level version of the Global Efficiency (previously defined) is often used for measuring the efficiency of information transfer within local subgraphs or neighbour nodes, and is called (*Local Efficiency*). Similarly to the Global version, it is defined as the inverse of the average shortest path length, computed with all the neighbours of a node among themselves; notice that *Local Efficiency* only reflects a "local integration" of the graph (in the neighbourhood of a node), hence it represents something more similar to a *segregating* property, rather than integrating.

- **Small-Worldness**
  Brain networks are observed to efficiently combine the presence of a well-defined modular structure (functional segregation of specialized activity) and of a strong inter-modular connectivity (integration) [55]; graphs with such characteristics (more precisely, graphs which shows a better combination of these two counter-trending aspects with respect to a random graph appropriately defined) are typically called *small-world*-networks. A possible measures of Small-Worldness, as defined in [56], is

$$SW = \left(\frac{C}{C_r} \right) \cdot \left(\frac{CPL}{CPL_r} \right)^{-1} \tag{2.9}$$

where C and CPL are respectively the Clustering coefficient and the Characteristic Path length of the graph; C_r and CPL_r are the same measures computed on a random graph (therefore the choice of the latter will be determinant).

- **Assortativity Coefficient** *Assortativity coefficient* is a global measure defined as the Pearson correlation coefficient between the Degrees of the two nodes which are connected by a link (for all the links in the network). Interpretation of this metric is less straight-forward than those of the previous ones, but in general graphs with positive values of Assortativity coefficient are likely to be more resilient to network modifications (due to the presence of interconnected high-degree hubs), while the contrary may indicate a more fragile network (high-degree hubs are tendentially separated, hence each of them has a greater importance for network topology).

- **Centrality measures**
  Centrality measures aim at characterizing the role of each node in the networks topology, testing its importance for functional integration and for network resilience to perturbations.
  Degree and Strength of a node can be regarded as the most basic examples of centrality measures, expressing directly its contribute to graph integration, in the most general sense. The so-called *within-module Z-Score*, or simply Z-Score, is a within-module version of the Degree, being defined (for i-th node) as

$$z_i^w = \frac{k_i^w\left(m_i\right) - \hat{k}^w\left(m_i\right)}{\sigma\left(m_i\right)} \tag{2.10}$$

  where $k_i^w\left(m_i\right)$ is the within-module m_i strength of the i-th node, $\hat{k}^w\left(m_i\right)$ being the average within-strength of the nodes in the module and $\sigma\left(m_i\right)$ the corresponding standard deviation.
  Participation coefficient is somehow a complementary metrics, quantifying the between-module degree centrality (assessing the intermodular interconnection of a node), and can be defined as

$$p_i^w = 1 - \sum_m \left(\frac{k_i^w\left(m\right)}{k_i^w}\right)^2 \tag{2.11}$$

  with sum ranging over the entire set of modules m. *Z-Score* and *Participation coefficient* together can be useful for identifying provincial hubs (contributing to module segregation) and/or connector hubs (contributing to inter-modular integration). Notice that, at a local level, *Z-Score* can be interpreted as a *segregating* property while *Participation coefficient* an *integrating* one.

Another important centrality measure is the so-called *Betweenness Centrality*, which doesn't rely on modules definition, and represents the fraction of all shortest paths in the network that pass through a certain node (then nodes with a high Betweenness centrality are easy to be bridges, having important roles for inter-modular integration).

It is important to consider that the density of a graph usually directly affects the computed values of other properties. This could represent a problem when a thresholding is applied on link values (always done for graph binarization, but also in weighted graphs to remove links representing weak correlations, which are likely to represent spurious connection is experimental situations [57]), since it is not usually clear what is the optimal density at which properties should be measured (and compared, when dealing with multiple graphs comparison); a common solution, if no prior information about optimal density is available, is to evaluate graph properties at different values of density [58].

Chapter 3

Olfactory Network resting-state connectivity

In the last two decades the development of efficient MRI experimental techniques allowed substantial progresses in the description of the neurobiological mechanisms that underpin the sense of smell.
The early portion of the olfactory sensory pathway has been precisely mapped from an anatomical point of view; in humans, it starts from the olfactory mucosa situated on the roof of the nasal cavity, in which are present the primary sensing neurons. Their axons form the *olfactory nerve*, which connects to the *olfactory bulb* [59]; from there, information is sent through a set of primary olfactory cortex areas (*Piriform cortex*, *Olfactory Tubercle*, *Cortical Amygdala*, *Periamygdaloid cortex*) and then distributed towards the so-called secondary olfactory sensory areas, not directly connected to the olfactory bulb. Regions which are strongly involved in the secondary processing of the stimulus are the *Hypothalamus*, *Thalamus*, *Caudal Orbitofrontal cortex*, *Prefrontal Cortex*, *Insular cortex*, *Amygdala*, *Hippocampus* and the *Nucleus Accumbens* [60]. Orbitofrontal cortex can be considered the final recipient of olfactory sensory information, being involved in reward and emotional value of stimuli [61] and decision making in olfactory-driven food intake [62] (see figure 3.1). In contrast to this detailed structural understanding of the olfactory sensory pathways, the functional organization of this circuit has not been understood in detail yet, and its description in literature is less coherent, also due to the diversity of the approaches employed and paradigms employed. The application of rs-fMRI techniques, with respect to task-based experiments, has offered a more direct approach for exploring the functional organization of olfactory-related areas and for delineating an intrinsic brain *Olfactory-Network* - ON.
With respect to other intrinsic brain networks, the measurement of ON spontaneous activations can be a much harder piece of work due to the largely subcortical composition of the network and the presence of important nodes near air-tissue interfaces [7]; in particular, in rs-fMRI whole-brain connectivity

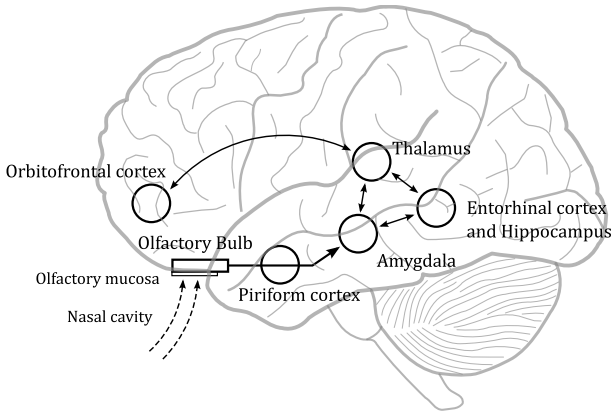

Figure 3.1: *Sketch of the major brain regions involved in early olfactory processing (lateral view). Olfactory stimuli from nasal cavity are collected by sensory neuro-epithelium cells in the olfactory mucosa and sent through the Piriform cortex.*

analyses, the olfactory-network activation can be really hard to observe and high-quality functional data is required.

3.1 Research overview

A localization of brain functional ON was described in the meta-analysis [63], which combined the results from 45 studies employing different imaging methods using the *activation likelihood estimation* - ALE method; the study identified some core regions directly connected to the olfactory bulb, including the *Piriform cortex*, *Amygdala*, *Orbitofrontal cortex* and the *anterior Insula*. These conclusions were confirmed by some more recent publications such as [64], which attempted to observe ON with rs-fMRI on a group of healthy subjects, obtaining coherent results.
In the last years, some studies have focused on the observation of ON differences between groups of patients and healthy subjects. Interesting results were found, for example, in ON connectivity of Parkinson's Disease patients [65, 66]; in these patients in fact, *olfactory-dysfunction* - OD is often observed as one of the earliest non-motor symptoms, though responsible mechanisms are currently unknown.
A recent interesting study from T. Campbell Arnold et Al. [7] (2020) exploited an extraordinary large rs-fMRI dataset (900 subjects, from the *Human Connectome Project*) to infer a meticulous description of an ON graph-model organization. By defining a set of 28 ROIs in regions supposed to be strongly involved in the olfactory primary and secondary processing, the authors of the study illustrated the construction of a group-averaged binary connectivity graph and its characterization using a graph-teoretical approach. In particular, by

means of a series of graph metrics and algorithms commonly adopted for brain connectivity-networks analyses (some of which were introduced in the previous chapter of this work), a tripartite modular organization of the graph was proposed, together with a characterization of the topological role of its most important nodes.
The main results of the study can be summarized as follows: (1) the functional olfactory network was identified as composed by 6 *key olfactory regions* and 16 *secondary regions* closely connected to them (listed in table 3.1); the identified network showed a pronounced modality specificity (i.e. segregation), with few connections to occipital visual areas; (2) within the network, three robust subnetworks were distinguished (modularity optimization was repeated with slightly different initial graphs for assessing reliability of the modular structure). It should be noticed that a certain degree of modularity is considered as a common feature of "optimized" functional networks, as it reduces overall complexity and may insulate local "errors". Nevertheless, direct estimations of Small-Worldness confirmed the high level of optimization of the network; (3) based on a set of node centrality measure, the Amygdala - AMY and the anterior Insula - INSa leaped out as major *hubs* of the network, with important roles also in inter-modular integration. The set up of the graph-based connectivity analysis described in 4.4.3 exploited these results as a major source, as they offer a reliable description of the human ON starting from rs-fMRI data. One of the limitations of the study was that it confined the analysis to the right hemisphere, in light of the predominantly ipsilaterality of olfactory pathways, assuming no differences between the hemispheres.

3.2 Olfactory dysfunction and COVID-19

During the 2020-2021 COVID-19 pandemic, Olfactory Dysfunction (OD) was found to be one of the most frequent and easily distinguishable symptoms of SARS-CoV-2 infection, affecting 50 to 70% of the infected. In most cases recovery of olfactory normal functions is relatively rapid, occurring within a median of 10 days, in parallel with the receding of other symptoms; instead, in a fraction of patients (approximately one tenth) OD persists up to several months from the infection, sometimes accompanied by a certain degree of cognitive impairment and other neurological symptoms, in the so-called *post-COVID-19 condition* (or *long-COVID*) [2, 67, 68].
Despite a growing body of evidences, the patophysiology undelying COVID-19 related OD is still debated and may involve disruption of the olfactory system at different levels, from the olfactory neurons located in the roof of the nasal cavity, to the neurons of the olfactory bulb and those in the olfactory cortices; in general, evidence suggests that COVID-19 OD could have a different etiology with respect to the OD in other viral upper respiratory tract infections

Table 3.1: *22 anatomical regions belonging to the Olfactory Network, according to [7]. The last column indicates the sub-network assigned to each node (nomenclature as in the original paper), based on the results of a modularity analysis.*

Key regions	APC	Ant. Piriform cortex	Sensory
	PPC	Post. Piriform cortex	Sensory
	AMY	Amygdala	Limbic
	ENT	Entorhinal cortex	Limbic
	OTB	Olfactory Tubercle	Limbic
	Oolf	Olfactory Orbitrofront. cortex	Frontal
Secondary	aHIP	Ant. Hippocampus	Limbic
	pHIP	Post. Hippocampus	Limbic
	Nacc	Nucleus Accumbens	Limbic
	HYP	Hypothalamus	Limbic
	INSp	Posterior Insula	Sensory
	INSd	Dorsal Insula	Sensory
	INSv	Ventral Insula	Sensory
	INSa	Anterior Insula	Frontal
	THLvp	Ventral Posterior Thalamus	Sensory
	Omm	Middle Medial OFC	Frontal
	Opm	Posterior Medial OFC	Frontal
	Omp	Middle Posterior OFC	Limbic
	Oc	Central OFC	Frontal
	Oapc	Anterior-APC OFC	Frontal
	Oml	Medial Lateral OFC	Frontal
	Oolfl	Lateral Olfactory OFC	Frontal

(frequently due to the obstruction of the olfactory cleft), as in COVID-19 OD there is a lower prevalence of sinonasal symptoms [69].
The use of different neuroimaging techniques is required in order to separately investigate the structures potentially involved in the mechanisms that originates OD: x-Ray CT can be exploited to exclude obstructive causes, whereas structural MRI may provide information about olfactory nerve, olfactory bulb and olfactory cortices morphology (and potentially detect abnormalities, such as in [70], suggesting that central mechanisms may play a role in persistent OD); diffusion weighted imaging (DWI) can be used to assess microstructural properties of white matter in ON-related brain regions (e.g. [71]); finally, functional MRI techniques have demonstrated to provide valuable contributions in the study of OD in neurodegenerative disease and post-traumatic anosmia (e.g. [72]).
In the next chapters of this work will be presented an experimental attempt of depicting the ON functional organization of patients suffering from persistent OD after COVID-19 infection, starting from rs-fMRI data, as to date few similar experiments are reported in literature. Some task-based fMRI experiments have measured a reduced activity of olfactory-related regions in patients with COVID-19 induced OD (for example, a case was reported in [5]), or different patterns of activation when comparing patients with OD originated from COVID-19 and patients who developed it after other infections (as in [3]). In a recent paper a reduced connectivity of the anterior Piriform cortex with respect to other ON-related regions, in patients with persistent OD after COVID-19 infection was measured, exploiting a brain connectivity graph-modelling based on rs-fMRI data [6]; this is actually the publication which is closer to what reported in the current work, but there are some key differences (such as the choice of the initial parcellation) which make a proper comparison of the results difficult (further details on that will be given in the dicussion, in section 6).

Chapter 4

Experimental materials and methods

4.1 Study cohorts and clinical assessment

A group of patients (23), suffering from persistent OD after COVID-19, were prospectively recruited from February to November 2021 at the IRCCS Istituto delle Scienze Neurologiche di Bologna. Inclusion criteria were: OD onset during SARS-CoV-2 infection (confirmed by a specific molecular or antigen test); OD duration longer that 1 month; no declared pre-existing OD or chronic rhinosinusitis. Each participant, after a clinical interview, underwent a neurological examination, olfactory assessment and MRI examination in the same day. A control group of healthy subjects (26) was recruited as well, matched for age and sex; control subjects declared no OD symptoms and underwent the same MRI protocol as the patients (see table 4.1 for further details about the study cohorts).

During the clinical interview patients were asked to describe OD symptoms either on quantitative scales (hyposmia, anosmia) or qualitatively (dysosmia). Olfactory performance was then evaluated through *Sniffin' Sticks* test, which is a widely used objective method for this kind of evaluation [73]. Results of the olfactory test are expressed with three scores (*olfactory threshold* - T, *odor discrimination* - D and *identification* - I); depending on the total sum of the three scores (TDI score - ranging from 3 to 48), olfactory performance is categorized

Table 4.1: *Demographic details of the cohort of subjects involved in the study.*

	F/M	**Age (years)**	**Education (years)**
Patients	12/11	$37 \pm 14 \quad (21 - 63)$	16.00 ± 3.06
Controls	13/13	$39 \pm 14 \quad (14 - 64)$	-

as *anosmia* if $TDI \leq 16.0$, *hyposmia* if $16.25 \leq TDI \leq 30.5$ or *normosmia* if $TDI \geq 30.75$. Neuropsychological evaluation included: handedness dominance evaluation (through the Edinburgh Handedness Inventory - EDI [74]), an ad-hoc battery of neuropsychological tests, including Montreal Cognitive Assessment MoCA [75]), language skills assessments, verbal and visuospatial memory tests, and attention and executive functions assessments; finally, emotional states and fatigue were evaluated with ad hoc scales.

4.2 rs-fMRI acquisition and pre-processing

4.2.1 Acquisition protocol

Each participant underwent a standardized brain MR examination, performed with a Siemens MAGNETOM Skyra 3T MRI scanner, equipped with a 64-channels high-density head/neck array coil. Before the acquisition participants were instructed about duration of the exam, they were asked to stay awake, with eyes closed, fixed in a comfortable position.
The MR protocol included a high-resolution volumetric T1-weighted acquisition (T1 MPRAGE; magnetization-prepared rapid gradient-echo; sagittal acquisition; isotropic voxel $1 \times 1 \times 1\,mm^3$; acquisition matrix 256×256; FOV $256\,mm$; repetition time $TR = 2300\,ms$; echo time $TE = 2.98\,ms$; inversion time $TI = 900\,ms$; flip angle $9°$; acquisition time 5 minutes and 21 seconds), followed by the rs-fMRI acquisition. For the latter a GRE-EPI sequence was used, with resolution $2.5 \times 2.5 \times 2.5\,mm^3$ (isotropic voxels), FOV $235\,mm$, repetition time was set to $TR = 735\,ms$, echo time to $TE = 37\,ms$ and flip angle to $53°$ (the choice of those parameters is optimized to achieve the best contrast with short TRs); the total acquisition time of the sequence was 10 minutes, corresponding to a total of $N = 816$ brain volumes.

4.2.2 Functional data pre-processing protocol

Concerning rs-fMRI data, for each subject a semi-automatic pre-processing pipeline was applied, following a well-established and standard protocol, specifically designed and optimized at the IRCCS Istituto delle Scienze Neurologiche di Bologna for this kind of data. First of all, GRE-EPI volumes (among the 816 of each sequence) that were displaced more than $1.5\,mm$ in any direction, or rotated more than $1.5°$ with respect to the central volume of the temporal sequence were detected and labelled as "displaced", as motion correction algorithms will likely fail to appropriately realign the images. Each sequence containing displaced volumes was then manually examined: if one exam contained more than one hundred consecutive displaced volumes, then exclusion of the subject should be considered. Successive steps of the EPI images pre-

processing were performed with the tools of the FMRIB Software Library - FSL, and included:

- **Motion correction** - performed with MCFLIRT [76] (part of FLIRT, which is a set of tools for linear intra- and inter-modal brain volumes registration), which exploits a trilinear interpolation to optimize a registration to the middle volume of the sequence, taken as reference;
- **Susceptibility distortions correction** - performed with the *topup* tool [77] from FSL, which generates a distortion field map obtained by acquiring volumes with opposite phase encoding directions for correcting the induced susceptibility artifacts;
- **Brain extraction** - to segment the brain volume and separate it from surrounding tissues, whose MR signal must be removed before next processing steps (BET [78]).
- **Intensity normalization** - computing the median intensity (I_m) among the whole sequence, and scaling the intensities of each volume by a factor $10000/I_m$.
- **Spatial smoothing** - using a $5\,mm$-FWHM Gaussian filter, to improve SNR [79]
- **High-pass temporal filtering** - using a $60\,s$ cut-off
- **Co-registration to T1-structural image** - using FLIRT, which optimizes the parameters of a linear transformation and applies it to the EPI images. This is needed for an easier visualization, and therefore interpretation, of the functional maps.
- **Registration to standard space** - using FNIRT, i.e. performing a non-linear registration, with the warping parameters previously optimized for a registration from T1-structural image to MNI-152 standard space. This step is performed so that all the subjects of the study can be referred to a common space.

After the data pre-processing four subjects from the patents group were excluded due to excessive motion or for the presence of intractable artifacts; analyses were then carried out on a group of 19 patients and a group of 26 control subjects.

4.3 Data de-noising: FIX-aided manual ICs classification

An ICA decomposition with no restrictions on the number of components (dimension) was run each subject's pre-processed rs-fMRI data. An automatic classification of the components was performed using FIX [41], which was pre-trained for feature classification on a group of 30 healthy controls (not part of this study; the trained algorithm was available from a previous project of the research group), who underwent the same acquisition protocol and pre-processing as the subjects recruited for this study. By a preliminary inspection of the results, the obtained labelling of the components was considered as not satisfying enough, probably because of the small number of subjects available for training the classifier; a manual re-classification was then performed (though aided by the FIX results, taken as a starting point for the components labelling) following the guidelines of L. Griffanti et Al. (2017) [40]. In particular, for this work, an initial training period under the supervision of a Neuro-radiologist has been necessary, as specific knowledge of the physiological and artifactual-related fMRI effects is required and this step can greatly influence the quality of the data available for the analyses, followed by the actual re-labelling work. At the end, a rough estimation of the algorithm performances, obtained by comparing FIX labelling with a ground-truth from the manual classification, highlighted a relatively low accuracy, with True Positive Rate (signal correctly classified as such) $\sim 93\%$ and True Negative Rate (noise correctly classified as such) $\sim 53\%$.

4.4 Data analysis

For the analysis of rs-fMRI data three different approaches were adopted: group-ICA, seed-based connectivity and graph-based analysis. The main target was to characterize the functional connectivity of each subjects cohort, and eventually to highlight the measured group-level differences; both internal ON connectivity and connectivity between the ON focal regions with the rest of the brain were studied.
The three approaches implemented, even though addressing the same functional connectivity between brain regions (defined as time-correlation between signals), are based on different assumptions and have different characteristics, hence can produce apparently different results, the meaning and the consistency of which will be discussed in chapter 6.

4.4.1 Group-ICA analysis

For each of the two groups, the cleaned data (already registered to the MNI space), were temporally concatenated, then, on each of the two stacks was per-

formed an ICA to find group-level robust correlation maps, using MELODIC tool from FSL [80]. The decomposition was repeated for different ICA dimensions (20, 30, 50, 100) and without the restriction of a specific number of components, since the optimal value for this parameter strongly depends on the particular goals of the analyses and is not easily predictable. However, the most significant results (relatively to the objectives of this work, i.e. identifying and characterizing the ON network) were found with a relatively low number of ICs ($\leq 30-50$. Some resulting ICs from the 50-dimensional ICA are represented in figure 4.1); with larger numbers, resulting components were indeed small and scattered, and it wasn't possible to recognize complete RSNs.

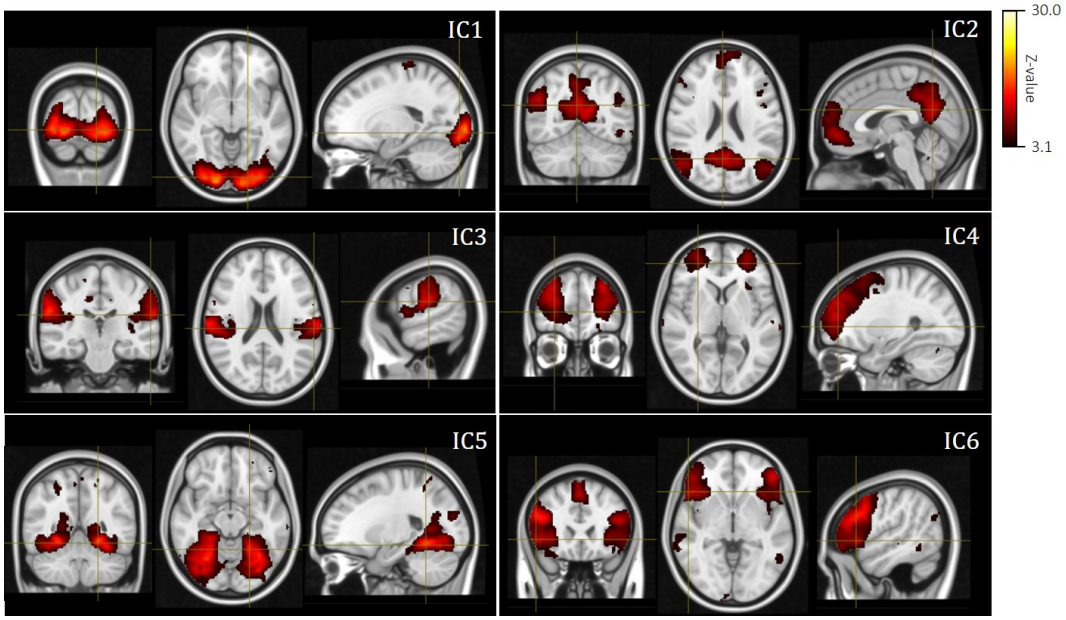

Figure 4.1: *Example of group-level ICs as produced by MELODIC algorithm (order is not the original); images intensity represents Z-values, thresholded at 3.1. All the ICs represents meaningful patterns of correlated activations, e.g. IC2 almost completely reproduce the Default Mode Network.*

The obtained group-level ICs were manually inspected in order to select those clearly attributable to the ON and eventually identify an entire reconstructions of the network of each cohort of subjects (this can be considered the first attempt of localization of the ONs).
In order to statistically test for any ON-related difference between the two groups, the group-level components selected from those of the healthy controls' group-ICA were then fed into a Dual-Regression to find subject-specific maps (as explained previously in this work, in section 4.4.1), which were finally used for inferring statistical differences between groups. This second part was realized by means of the Dual-Regression tool implemented in FSL [42]. Non-

parametric statistical testing was performed through a permutation testing, so the final results were spatial maps of group-differences statistical significance (and should be thresholded).

4.4.2 Seed-based ON analysis

The position of the seeds required for this type of analysis were determined according to literature, and in particular referring to [63]. Starting from these positions two possible approaches may be adopted to draw the seeds: (1) a simpler solution is to create a spherical volumes of fixed radius and centered at the coordinates provided by literature, (2) a more sophisticated solution is to use an appropriate pre-defined brain parcellation and to select the ROIs based on the overlap with the location provided by literature. The main advantages of solution (1) are that hypotheses are more general and all the seeds have equal volume; the main disadvantage is that a spherical volume may include a significant portion of white matter and/or cerebrospinal fluid (CSF), whose signal is expected to be predominantly noise. For this work, both the solutions were attempted.
In the first case, the pre-processed rs-fMRI data of all subjects were warped to the standard MNI template. Spherical seeds of $5\,mm$ radius were drawn on the MNI and centered at the absolute positions reported in table 4.2 (see figure 4.2). First, `dual_regression` (from FSL) was applied on each subject's data with a mask containing all the 6 seeds together, to derive individual spatial maps of correlation. On one hand, these maps were then combined to derive statistically significant group-level connectivity maps (which can be considered as a first attempt to spatially "localize" the ON); on the other hand, a group-comparison between the two sets of individual correlation maps was performed. In practice, the group-level correlation maps (*average* maps) and the group-differences maps (*contrasts*), both expressed in terms of statistical significance levels (corrected p-values), were produced with the `randomise` tool (from FSL) provided with a design matrix and the set of desired contrasts: 2 for the average map of each group and 2 for difference estimation (HC>PAT and PAT>HC). `randomise` is a tool for non-parametric permutations testing, specifically designed for inference on neuroimaging data; it performs random permutations on a set of provided images to generate a null-distribution for the voxel-wise comparison of the same data, and then produces spatial maps of statistical significance (corrected p-values) for the particular hypothesis to be tested (i.e. one-sample t-test for *average* maps of each group and 2-samples t-tests for *contrasts* maps). Further details regarding this tool can be found in [81] and [82].
A similar attempt with the spherical seeds was made by using the 6 seeds masks separately (*stacked* on different volumes of a unique image file). Also in

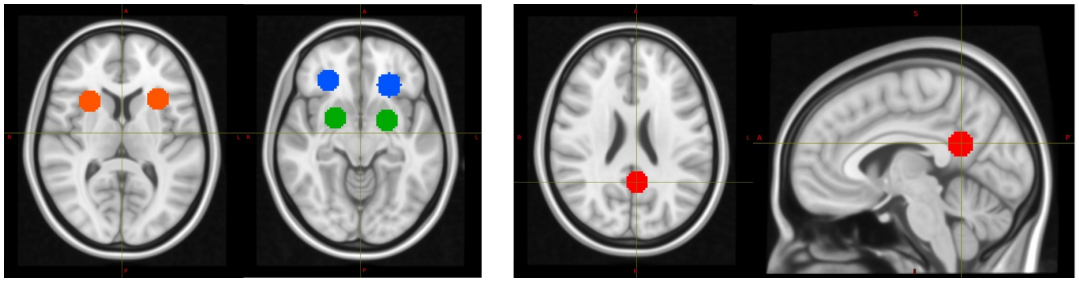

Figure 4.2: *Left - Spherical ON seeds used for the seed-based analysis, axial view (registered to the MNI). Orange: anterior Insula; blue: orbitofrontal olfactory cortex; green: piriform cortex.*
Right - Spherical seed used for the seed-based analysis of the DMN, corresponding to the Posterior Cingulate cortex (axial and sagittal views).

Table 4.2: *Centers of the spherical ROIs selected for the seed-based analysis of the ON (in MNI coordinates).*

Anatomical region	**Hemisphere**	**Abbr.**	**x**	**y**	**z**
Piriform cortex	L	PC_L	-22	0	-14
	R	PC_R	22	2	-12
Anterior Insula	L	$INSa_L$	-36	18	6
	R	$INSa_R$	28	16	8
Orbitofrontal olfactory cortex	L	$Oolf_L$	-24	30	-10
	R	$Oolf_R$	28	34	-12

this case, after having computed individual (subject-specific) spatial maps of correlation for each of the seeds with the `dual_regression` command, group differences were assessed.
As a control network, an equivalent version of seed-based analysis was repeated starting from a single spherical seed placed in a focal region (*Posterior Cingulate Cortex* - PCC) for the *Default Mode Network* - DMN, which is one of the main and most easily detectable RSNs.

The analysis (both the localization of the ON, performed by running a Dual Regression with a unique mask with all the seeds, and all the seeds separately) was then repeated starting from 6 anatomically segmented seeds. The seeds were obtained from the subject-specific volumetric segmentation of T1-structural images performed with Freesurfer [83], and in particular from the Destrieux anatomical atlas. The 6 selected regions were: the *Amygdala* - AMY (L/R, corresponding to regions 18/54 of the atlas), the *anterior Insula* - INSa (L/R, 12118/11118) and 2 ROIs were obtained by merging *Orbital medial olfactory cortex* regions (L/R, 12164/12124), and the *Orbital frontal cortex* (L/R,

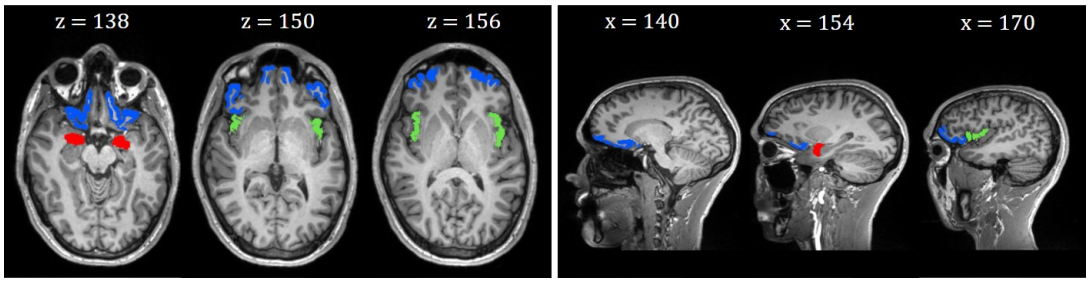

Figure 4.3: *Example of anatomical ON seeds used for the seed-based analysis, as segmented on a subject's T1-structural image (right - axial view, left - sagittal view; z and x indicate MNI coordinates of the slices). Blue: orbitofrontal cortex; red: Amygdala; green: anterior Insula.*

11164/11124) - OFC (see figure 4.3).

4.4.3 ON-restricted graph-based analysis

Graphs construction

For the ON-restricted graph construction, a set of 25 bilateral anatomical ROIs were selected from the Brainnetome Atlas parcellation ([84]); the choice of this atlas among the many available was due to its fine-grained subdivision of the brain in 246 ROIs, and to the fact that the parcellation was derived from a consensus of structural and functional connectivity (which makes it more suitable than anatomy-based atlases for the analysis of rs-fMRI data). On the other hand, the choice of the ROIs was based on the related publications found in literature (mainly [7, 64, 66]). Some ROIs of the Brainnetome Atlas (amygdala and thalamus) were merged to define a single node to better replicate the graphs used in the mentioned publications. At the end, the ON-restricted graph was composed by a total of 34 nodes (17 bilateral), listed in table 4.3.
For each subject's rs-fMRI data registered to the MNI standard space, average signal time courses from each of the 34 ROIs was extracted (using FSL tools, by averaging the BOLD signal of all the voxels in the ROI). The 34×34 connectivity matrix (*adjacency matrix* of the graph) was then obtained by computing the Pearson's full correlation coefficient between each pair of time series, after filtering them with a Gaussian kernel (5 time-points moving window - approximately $3.7\,s$) to further suppress high-frequency components of the signal spectrum. Negative correlations values were set to 0, as their interpretation in functional networks is still debated, since there is evidence that their inclusion could negatively affect test-retest reliability [85]. Finally, the values of each of the 45 obtained matrices (19 patients, 26 healthy controls) were transformed into a Normal-distribution with a Fisher's r-to-z transformation (i.e. inverse hyperbolic tangent of the r value). Network properties were then evaluated both on binarized and weighted versions of these graphs.

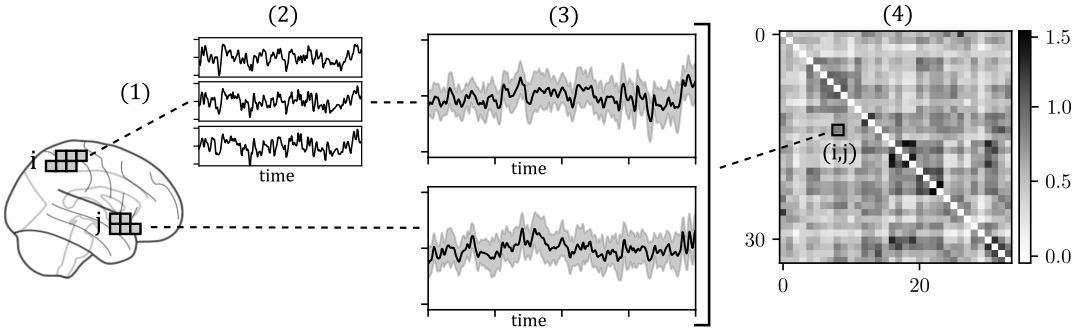

Figure 4.4: *Schematics of the steps required for graph construction: (1) Extraction of single voxels' time series from EPI data; (2) Computing ROIs average time series; (3) Pearson correlation between time series, removing negative correlation values and Z-transformation.*

All the steps required for the graphs construction (and the subsequent analysis), after the extraction of average time series, were performed using MATLAB R2021b, and in particular with the tools implemented in the *Brain Connectivity Toolbox* - BCT [86], and in the *Statistics and Machine Learning Toolbox*. A schematics summarizing the graphs construction is represented in figure 4.4.

Graphs properties evaluation

For each patient, a set of 40 adjacency matrices at increasing density were generated, by applying a *proportional thresholding* on the full Pearson's correlation matrix in the density range $1 - 80\%$ with a step of 2%. Such matrices were also binarized and the analysis was preliminary conducted on this set, before evaluating the weighted one. Finally, a corresponding random version of each matrix was computed by randomly "rewiring" each link 10000 times (so that original density and degree distribution were conserved); such randomized versions of the matrices were then used to normalize property values. Links permutation was performed using the function `randmio_und` implemented in the BCT [87].
On each binary graph a set of 12 properties, at global or local level, were evaluated. Global measures included: Small-Worldness, Global Efficiency, Giant Component Size, Characteristic Path Length and Modularity Coefficient; locally, instead, the Degree, Local Efficiency, Clustering Coefficient and Betweenness Centrality of each node. Furthermore, average values of Local Efficiency, Clustering Coefficient and Betweenness Centrality were computed for all the nodes of each network. For weighted graph the same 12 properties, plus the nodes' Strength, Participation coefficient and within-module Z-Score, (at a local level) and the graph Assortativity Coefficient (global) were calculated.
By integrating the property values over a range of meaningful densities, it was then possible to characterize each subject with a robust set of values, not de-

Table 4.3: *ROIs of the Brainnetome Atlas selected as nodes for the ON-restricted graph; corresponding anatomical names and Brainnetome Atlas identification numbers (BA number) are reported.*

Anatomical region	**Abbr.**	**BA number**
Orbitofrontal Olfactory cortex	$Oolf_R$	46
	$Oolf_L$	45
Anterior Piriform cortex	APC_R	50
	APC_L	49
Amygdala	AMY_R	212-214
	AMY_L	211-213
Anterior Hippocampus	$aHIP_R$	216
	$aHIP_L$	215
Posterior Hippocampus	$pHIP_R$	218
	$pHIP_L$	217
Entorhinal cortex	ENT_R	116
	ENT_L	115
Thalamus	THL_R	232-234-236-238-240-242-244-246
	THL_L	231-233-235-237-239-241-243-245
Anterior Insular cortex (internal)	$INSai_R$	166
	$INSai_L$	165
Anterior Insular cortex	$INSa_R$	168
	$INSa_L$	167
Anterior Insular cortex (dorsal)	$INSd_R$	38
	$INSd_L$	37
Anterior Insular cortex (ventral)	$INSv_R$	172
	$INSv_L$	171
Posterior Insular cortex	$INSp_R$	164
	$INSp_L$	163
Anterior-lateral Olfactory cortex	Oal_R	28
	Oal_L	27
Medial-lateral Olfactory cortex	Oml_R	44
	Oml_L	43
Nucleus Accumbens	$NAcc_R$	224
	$NAcc_L$	223
Anterior Cingulate cortex	$CINa_R$	180
	$CINa_L$	179
Rostral Cingulate cortex	$CINr_R$	188
	$CINr_L$	187

pending on a particular density. The choice of the range of densities was mainly based on the observed average Small-Worldness curve trend. In fact, on one hand one expects that most informative densities are those where the graphs exhibits Small-World characteristics (i.e. Small-Worldness should be larger than one), but it must be considered also that at very low densities graphs are sparse and some measures could present strong discontinuities (particularly for small graphs). At the end for ON-restricted analysis a range $10-50\%$ was used, while for whole-brain graphs analysis a $4-50\%$ was chosen.

Group comparisons

With the measures obtained, characterizing each individual functional network, a group-level comparison was set up. In particular, after having verified the Normality hypothesis for each group of measures to be compared with a *Kolmogorov-Smirnov* Normality Test [88], an *ANaysis of COVAriances* - ANCOVA was applied using patients age as covariate regressor; the choice of using an ANCOVA instead of a simple ANOVA was motivated by the fact that effects on ageing on brain activity and in particular in functional connectivity have been extensively demonstrated (e.g. [89]). In particular, the `aoctool` function from the Statistical and Machine Learning Toolbox was used, with a *parallel lines* modelling (i.e. assuming that response variable dependence with respect to the covariate is the same across groups) such as

$$y = (\alpha + \alpha_i) + \beta \cdot x + \epsilon \tag{4.1}$$

where y is the response (measured values), x the covariate, β the slope describing dependence on the covariate and $(\alpha + \alpha_i)$ the intercept of i-th group.
The Benjamini and Hochberg method was applied for controlling the *False Discovery Rate* - FDR [90], being particularly important in the case of local measures, for which a large number of comparisons are performed; Bonferroni correction for multiple comparisons, which can considered a more conservative test, gave comparable results.
Statistical significance was considered at corrected p-vales < 0.05.

Network Based Statistics - NBS

The set of ON-graphs were analyzed also with the *Network Based Statistics* - NBS method [91] (implemented in the NBS Connectome MatLAB package). NBS is a validated tool for identifying statistically significant group-differences in the links of a graph. In practice, starting from the set of subject-specific connectivity matrices, this tool allows to massively test a certain hypothesis on all the entries of the matrices, automatically controlling for the family-wise-error-rate - FWER (i.e. multiple comparisons).
NBS can be seen as the graph analogue of cluster-based statistical methods commonly used in mass-univariate testing on the pixels of an image; instead of

peforming clustering in physical image-space, the NBS clusters in the graph-topological space (i.e. each connected component is considered as the equivalent of a cluster). FWER-corrected p-values are calculated for each component using permutation testing.
In practise the algorithm operation can be summarized in four main steps (more details are available in [92]):

1. Independently test the same hypothesis of interest at every connection of the graph (e.g. connections strengths are equal); each connection is therefore characterized with a single test-statistic value.

2. Perform a first threshold on these values to select the most significant connections.

3. Identify topological clusters among these; discard sparse supra-threshold connections (notice that NBS cannot detect alterations of isolated links, and this is a limitation of the method).

4. Compute FWER-corrected p-value using permutation testing, for each identified connected component (in practice the first three steps are repeated many times, for different random permutations of data in the initial matrices; the size of the largest component is recorded for each permutation, so that an empirical null distribution for the size of the largest component size is estimated; with such a distribution FWER-corrected p-vale can be computed)

The first threshold on single test-statistics values was set at 3.1 (equivalent to $p = 0.001$); $N = 5000$ permutations were performed, and a significance threshold of $p = 0.05$ was selected at the end. Among the different measures available for the components' size the "extent" was chosen (i.e. the size is simply defined as the number of connected nodes).
The NBS analysis was repeated with graphs at different densities ($10 - 50\%$, step 2%); each time, nodes belonging to altered components were assigned with a score proportional to the estimated significance of the alteration; at the end the mean-score for each node was computed. Final *alteration score* - AS for i-th node

$$AS_i = \frac{1}{N} \cdot \sum_d \left(\frac{p_{i,d}}{0.05} \right)^{-1} \tag{4.2}$$

whit d ranging over the set of densities (N in total), p representing the p-values of each component as computed by NBS.

4.4.4 Whole-brain graph-based analysis

A similar graph-based analysis was performed at a whole-brain level, including all the 246 ROIs identified by the Brainnetome parcellation (hence including

also the ON-subgraph). Also in this case graphs were evaluated at different values of density, in both binary and weighted versions, and corresponding random graphs were computed as well with the random permutation of links.
The metrics employed were the same of the ON-restricted analysis, with a difference in the definition of the modules used for Z-Score and Participation Coefficient computation: in this case were used the modules found by the `community_louvain` algorithm (already used for Modularity Coefficient estimation).
Even though the analysis was analogue to the ON-restricted case, results obtained with whole-brain graphs are not expected to be the same, and will require a separate discussion.

4.4.5 Correlations with clinical scales

All the statistically significant group-level alterations detected by the previous ON-restricted and whole-brain analyses were correlated with the clinical scores obtained by each patient. In practice, for each patient, the partial (Pearson's) correlation coefficient between the measures of the properties which were found to be altered at a group-level and the results in the olfactory function assessment, neuropsychological tests, emotional states and fatigue scales was evaluated; age of the subjects was used as single confounding variable for correlating the Sniff-tests results, while age and education were used in the correlations with neurospychological scores. Statistical significance of the correlations was set at $p < 0.05$; no correction for multiple comparisons was adopted at this stage, as it was intended to be an exploratory analysis.

4.5 Subject-specific ROIs segmentation improvement (algorithm prototype)

An original algorithm for subject-specific improvement of ROIs segmentation was developed (*rs-Data Parcellation Improvement* - rsDPI) and run on the available data. The algorithm addresses the problems arising from potentially imperfect registrations of the ROIs of the selected parcellation onto individual functional EPI data. When using fine-grained anatomical parcellations in fact, a precise registration of the ROIs masks is fundamental in order to avoid the inclusion of signal from adjacent regions, and consequent SNR loss when average time series are computed. Following a similar rationale of the method proposed in [47], the algorithm analyzes the internal correlation of each ROI, sorts the voxels according to their individual correlation with the others and removes the least correlated ones when they are on the borders of the ROI's

volume. The application of a voxels-removal step, when performing ROIs- or parcellation-based analyses with fMRI data, is not part of the main standardized data pre-processing workflows but there exists many examples in literature adopting a similar step, such as in [7].
A python implementation of a prototype version of DPI algorithm was made freely available in a dedicated GitHub public repository.

4.5.1 rsDPI algorithm

The rsDPI algorithm is based on the fundamental assumption that the input parcellation should theoretically insulate functionally homogeneous regions, i.e. each individual voxel inside the volume of the region should have a similar BOLD signal time course. The algorithm targets those voxels which are on the edges of the volume and show a low correlation with the rest of the region, hence probably erroneously included for mis-registration or individual variability reasons; its working principle can be summarized as follows:

1. Individual time series from voxels in each region of the parcellation are extracted from EPI data, possibly before the application of the Gaussian spatial filter.

2. Internal-connectivity matrix of each region is computed according to the chosen metric of functional-connectivity (in our case Pearson correlation between time courses); each voxel's internal connectivity is then computed as column-average values.

3. A fraction p of the least correlated voxels are selected (set A); if the resulting thresholding value is lower than t, more voxels are iteratively added to A until their maximum value of connectivity reaches t.

4. external voxels of each region are selected by performing n morphological *erosions* on the 3D volumes (set B).

5. Sets A and B are intersected, and resulting voxels are removed from the region volume.

Optimal values for each of the parameters clearly depends on the data available; after some preliminary attempts, for the current work $p = 0.20$, $t = 0.05$ and $n = 2$ were used (despite the appearance $p = 0.20$ was a quite conservative value; $n = 2$ was a more aggressive choice, considered the small size of the regions in the adopted parcellation).
The rsDPI algorithm was used to refine the set of 34 ROIs from the Brainnetome parcellation used for the ON-restricted graph analysis, for each of the subjects in the PATs and HCs groups; with these new ROIs, average time series were extracted from EPI images, a new set of connectivity matrices was drived and

the whole ON-graph analysis repeated. The results obtained with the new ROIs were then variously compared with those obtained with the common parcellation. A parameter used to characterized the new time courses is the *raw*-time averaged SNR, computed as

$$SNR = \frac{1}{N_t} \cdot \sum_t \frac{\mu_t}{\sigma_t} \tag{4.3}$$

where N_t is the number of time-points, and μ and σ respectively the standard deviation and the average value of instantaneous signal values from the voxels inside a given region.
Other comparisons were focused mainly on the weights' distributions of the matrices obtained in the normal analysis and the new ones.

Chapter 5

Results

5.1 Seed-based analysis

5.1.1 DMN localization and group-differences

Individual spatial maps obtained with the seed-based correlation analysis using the PCC spherical seeds were combined and *randomized*, to obtain group-level maps (expressed in terms of corrected p-values); by applying a threshold $p < 0.05$ (statistical significant correspondence within the group), as expected, for both groups the resulting maps showed a great correspondence with the DMN descriptions found in literature: significant peaks were observed with the Medial and Dorsal-Medial Prefrontal Cortex (mPFC, dmPFC), left/right Angular Gyri, left/right Temporal Poles, left/right Hippocampus and Parahippocampus (see figure 5.1).

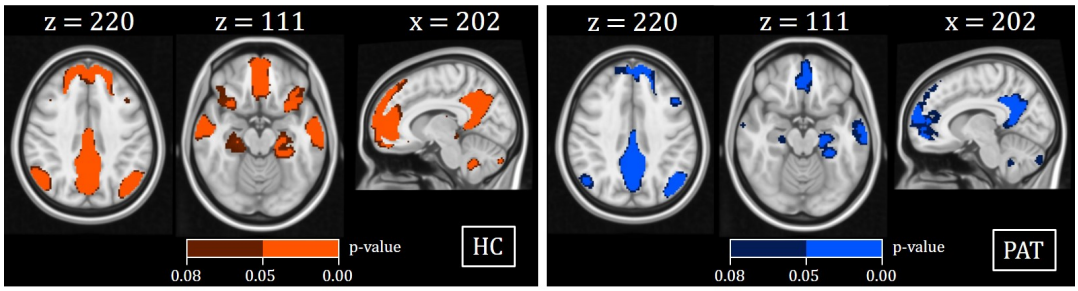

Figure 5.1: *Corrected p-value maps for DMN localization, axial and saggital views (Left - patients group, right - healthy controls group). Brighter blue/orange refers to a threshold o p<0.05 (statistically significant correspondence within the group); darker blu/orange refers to a threshold of p<0.08 (for a better visualization of the maps).*

From the group comparison performed by means of the dual-regression, no statistically relevant differences were detected between the set of connectivity

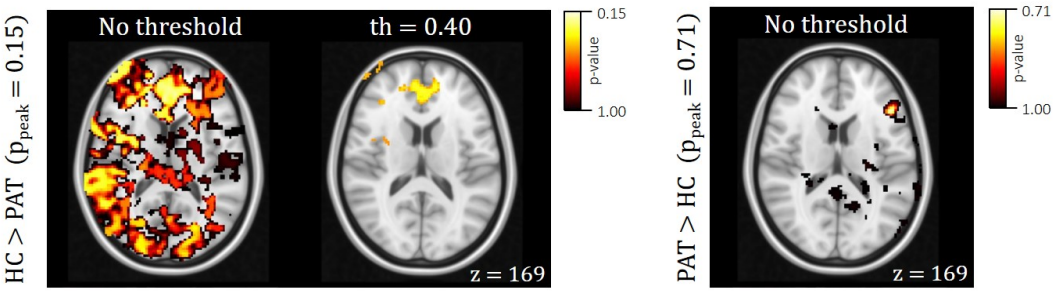

Figure 5.2: *Corrected p-value maps for DMN groups alterations, axial views. Left - maps relative to contrast HC>PAT, without thresholding and at p<0.40; right - contrast PAT>HC. Brighter colors represents lower p-values. Peak of significance was 0.15 in the first case and 0.71 in the second, hence these differences are not considerable as statistically relevant.*

maps of the patients and those of the healthy controls; in other words: none of the peaks of intensity of the maps of corrected p-values, representing the statistical significance of the observed difference between the two groups, managed to survive to the application of the threshold. The difference maps are reported, as examples, in figure 5.2; in the next sections we will always refer to the peak values of such maps as *peaks of difference significance*.

5.1.2 ON - Spherical seeds

From a first qualitative inspection of the individual spatial-maps of correlation obtained with the mask containing all the 6 ON spherical seeds together, a great *dispersion* of the maps was noticed, with broad and weak correlations of regions not always corresponding to the ON core areas. The resulting group-level maps, once randomization was performed, showed no signal surviving to the $p < 0.05$ thresholding, meaning that consistency between the individual maps wasn't sufficient to robustly localize the ON in these group; just as an exploratory attempt, the procedure was repeated on restricted groups composed by the 6 subjects from the PATs and the 7 from the HCs which showed better results at individual level (i.e. better correlation maps, with discrete correspondence with the expected ON[1]), but even in this case no statistical significance was reached at group-level (figure 5.3).

The analysis conducted then with the 6 seeds separately (stacked). In figure 5.4, as examples, the individual maps of connectivity (expressed as Z-statistics) of a subject from the HCs group, and of one from the PATs group, for each of the 6 ROIs (even though it should be mentioned that a great variability was found

[1]Evaluations were only qualitative, obviously the results of this attempt are reported for demonstration purposes and should not be considered as relevant.

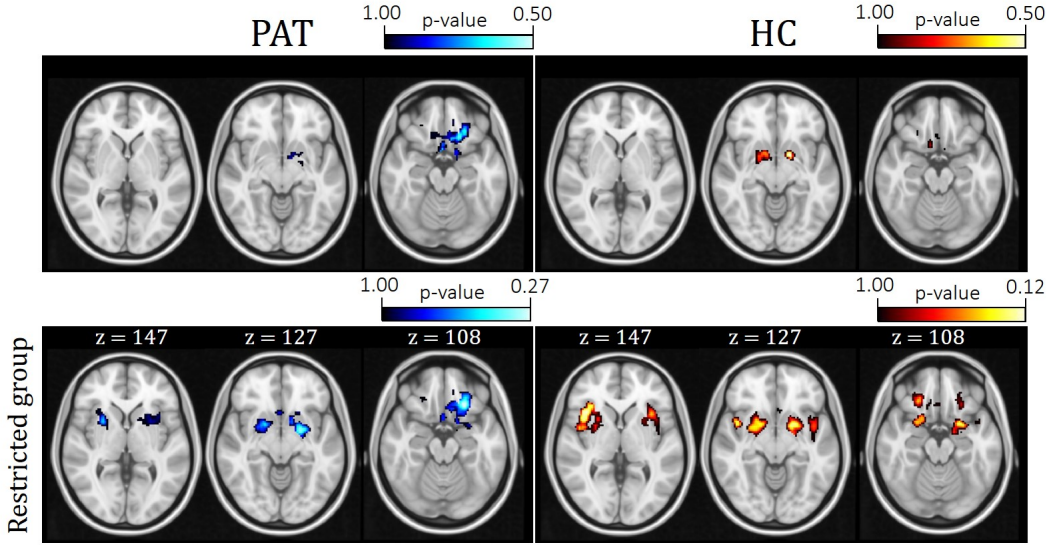

Figure 5.3: *Localization of the ON by means of the 6 spherical seeds, for PATs (left) and HCs (right) total groups (top), and for reduced groups (bottom; only as exploratory attempt. These maps were obtained as average group-level maps from the seed-based analysis. Intensity represent statistical significance in terms of corrected p-values; z values represent the MNI axial coordinate of the visualized slice. None of the peaks in these maps reached the p=0.05 level.*

in the set of correlation maps relative to the same seeds) are reported. Even in this case, the analysis did not reveal any significant group difference in the connectivity of any of the regions with the rest of the brain; lowest corrected p-values were reached in the Oolf_L and Oolf_R connectivity comparisons, for opposite contrasts (spatial distribution of p-values are represented in figure 5.5). Table 5.1 summarized the peaks of significance resulting from each comparison.

Table 5.1: *Peaks of significance (corrected p-values) resulting from the comparison of the connectivity of each of the 6 spherical seeds between the two groups. None of the comparisons found any significant alteration.*

Contrast	$\mathbf{PC_L}$	$\mathbf{PC_R}$	$\mathbf{INSa_L}$	$\mathbf{INSa_R}$	$\mathbf{Oolf_L}$	$\mathbf{Oolf_R}$
HC>PAT	0.65	0.10	0.48	0.46	0.063	0.94
PAT>HC	0.11	0.89	0.55	0.13	0.49	0.092

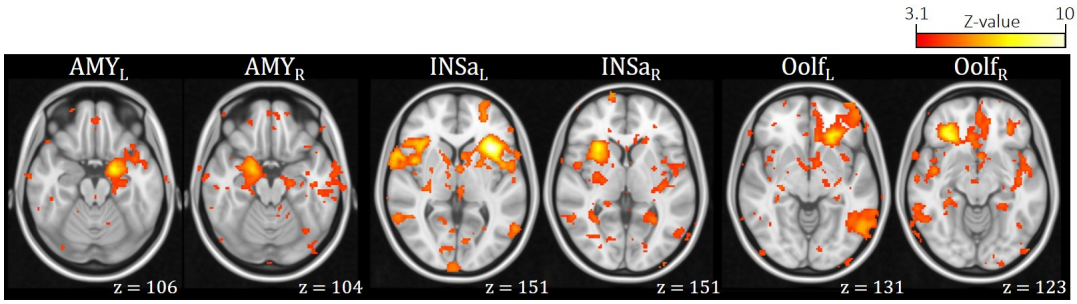

Figure 5.4: *Example of individual correlation maps (from a subject of the HCs group) derived with the 6 spherical seeds, obtained with the dual-regression. Intensity reflects Z-statistics, thresholded at 3.1; positions of the peaks of correlation essentially reproduce the positions of original spherical seeds. z values indicate the MNI axial coordinate of each slice.*

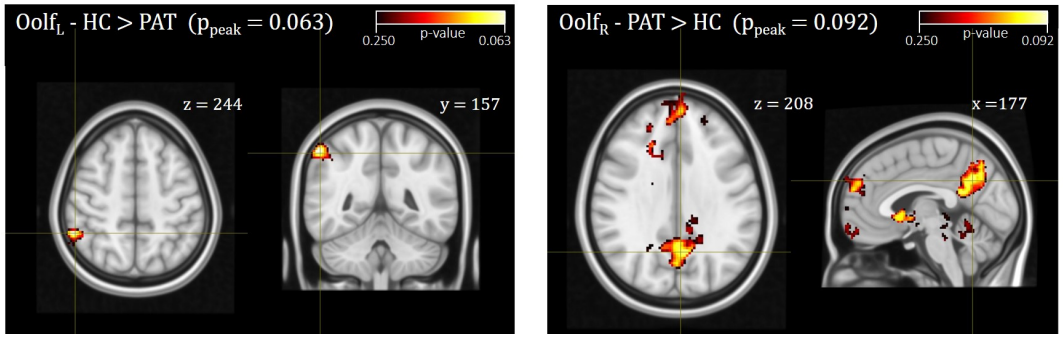

Figure 5.5: *Differences of the connectivity of the Oolf$_L$ (left image) and of the Oolf$_R$ (right) spherical seeds, in terms of corrected p-values. Both the maps are thresholded at p<0.25 and do not represent statistically significant differences. By thresholding the same maps at p<0.10, only few single scattered voxels would remain in the images. z, y and x values indicate MNI axial and sagittal coordinates of each slice.*

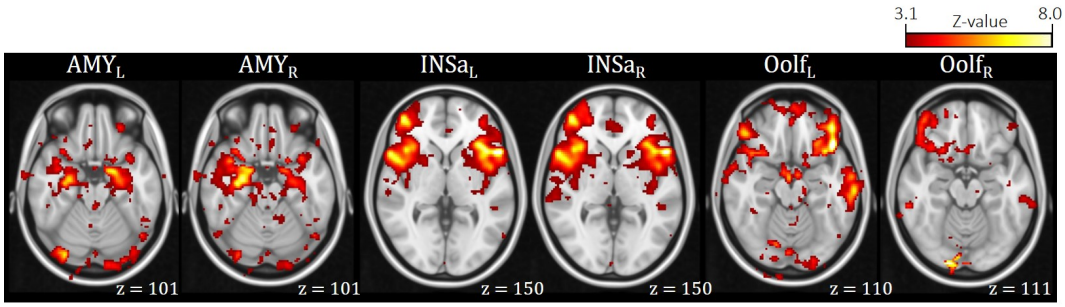

Figure 5.6: *Example of individual correlation maps (from a subject of the HCs group) derived with the 6 anatomical seeds. Intensity reflects Z-statistics, thresholded at 3.1; peaks of correlation are found mainly in the original seeds, but also in other regions (e.g. are often bilateral). In the Oolf$_R$ case, the map is worse, and has a peak which probably is due to noisy signal in the seed. z values indicate MNI axial coordinates of each slice.*

5.1.3 ON - Anatomical seeds

Even by using anatomical seeds, it wasn't possible to obtain a better ON localization by running the analysis with all the seeds at the same time; peaks of intensity of the average maps, after the randomise step, did not reach the statistical significance of p=0.05.
The individual maps obtained in the dual-regression analysis with the 6 seeds separately, were generally better than in the previous case (spherical seeds) in terms of peaks of correlation and grey-matter overlapping and "plausibility" of the observed patterns of correlation (e.g. bilateral activations were much more frequently observed with anatomical seeds. Some examples) are reported in figure 5.6. As in the previous analysis however, also in this case the group comparison of connectivity maps relative to the stacked seeds didn't show any statistically significant differences. Peaks of significance (in terms of corrected p-values) reached for each of the contrasts are summarized in table 5.2 (noticed that are even higher - i.e. lower significance - than those relative to spherical seeds, previously reported in table 5.1).

Table 5.2: *Peaks of significance (corrected p-values) resulting from the comparison of the connectivity of each of the 6 anatomical seeds. No statistically significant differences were found between the two groups.*

Contrast	**AMY$_L$**	**AMY$_R$**	**INSa$_L$**	**INSa$_R$**	**OFC$_L$**	**OFC$_R$**
HC>PAT	0.39	0.37	0.32	0.12	0.34	0.39
PAT>HC	0.41	0.39	0.60	0.85	0.47	0.17

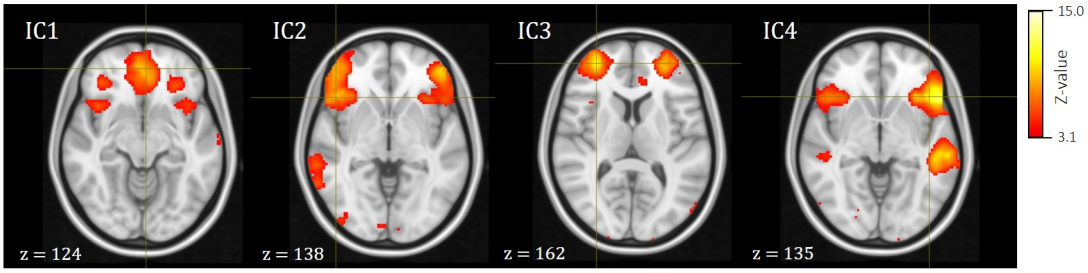

Figure 5.7: *ICs selected from the group-ICA as attributable to the ON from the group-ICA; intensity represents Z-values, thresholding was set at Z-value* > 3.1*. Indicated z represent the MNI coordinates of the visualized slices. None of the ICs completely reproduced the ON.*

5.2 Group-ICA

Among the results of the different group-ICAs performed at different dimensions, those from the 50-ICs decomposition were established to be the best for our purposes. In figure 5.7 the 4 ICs selected as attributable to the ON are represented. Each of these components in fact presented peaks in regions considered to be potentially involved in the ON: the first component (IC1) near the CINa, OFC and INSa; the second (IC2) in the inferior frontal and middle temporal gyri; the third one (IC3) in the middle frontal gyrus; the last one (IC4) near the INSa and in the middle temporal gyrus. After running the dual-regression, and having performed the group comparison between the obtained subject-specific maps of correlation, no statistically significant difference was found. Details about the results of the comparison are reported in table 5.3. Maps of the most significant alterations are represented in figure 5.8

Table 5.3: *Peaks of significance (in terms of corrected p-values) of the difference between groups resulting from the dual-regression after group-ICA; none of the 8 comparisons reached the critical level of significance of p=0.05, hence no alterations between the groups was detected.*

Contrast	**IC1**	**IC2**	**IC3**	**IC4**
HC>PAT	0.35	0.83	0.45	0.12
PAT>HC	0.57	0.11	0.17	0.47

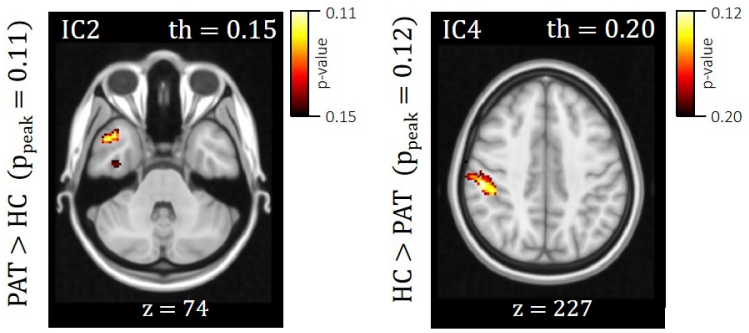

Figure 5.8: *Most significant alterations found using the ICA-based comparison. None of the detected differences reached the significance level of p=0.05 (intensity represents corrected p-values; th values are the p-value thresholds applied).*

5.3 Graph analysis results

The graph-based analysis, given the broad range of measurement possibilities offered, was the approach which gave the most significant results. In the next sections are reported the main ones, with a particular focus on the ON-restricted weighted graph-analysis (section 5.3.1), which highlighted the most significant differences between the patients (PATs) and healthy controls (HCs) groups. In section 5.3.2 the results obtained with the binarized versions of the graphs are briefly summarized, while in section 5.3.3 those of the whole-brain graph analysis are reported.

5.3.1 ON-restricted weighted graphs

Some examples of connectivity matrices representing the full weighted ON-restricted graphs are represented in figure 5.9; alongside the relative histograms of weights (representing Z-transformed correlation values, as explained above) are reported. The first thing to notice is the high individual variability affecting these matrices, even though common patterns of connectivity can be identified. To exclude potential biases introduced by overall connectivity strength differences between the two groups, both the total weights distributions (5.10) and the subject-specific average weight values distributions were compared with two-samples Kolmogorov-Smirnov tests, and no differences were observed ($p > 0.1$). As explained in the previous chapter, starting from each correlation matrix a set of thresholds were applied, so that measurements were performed at different link density values. In the next sections, for each global measure, representative group-averaged trends will be reported; as previously explained, the actual group comparison was performed with the results of the integration of individual trends, in the range of densities $10 - 50\%$.

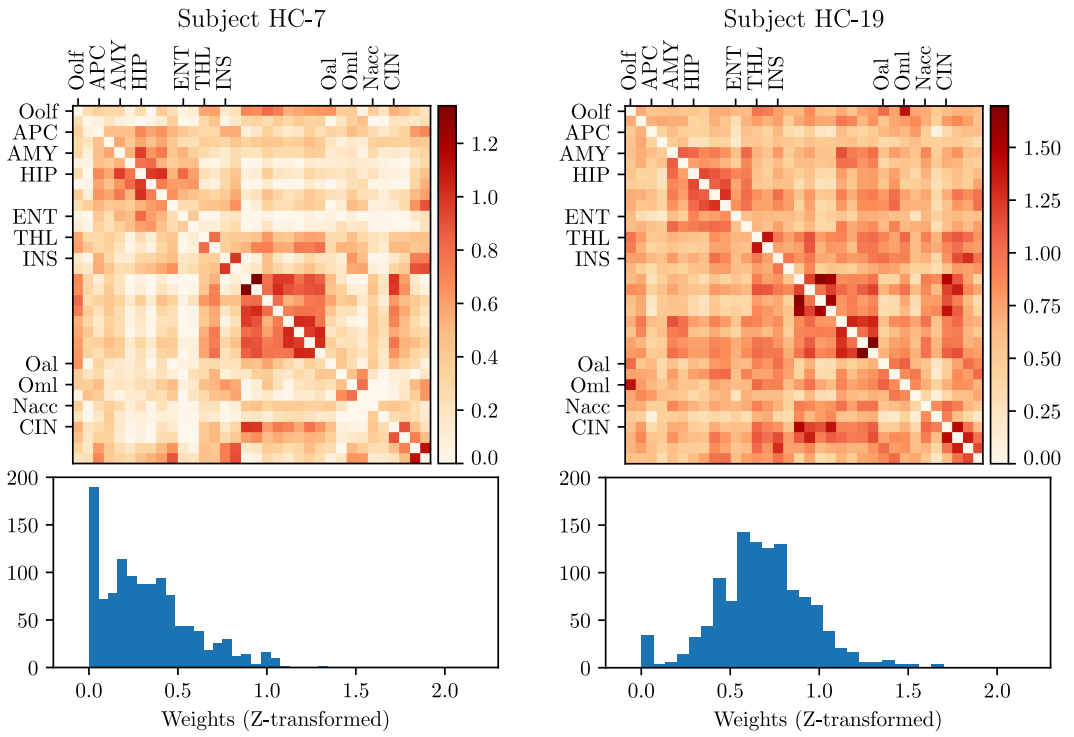

Figure 5.9: *Examples of connectivity matrices from two subjects from the healthy controls group, with corresponding histograms of links weights; a great variability was observed among the individual matrices, even though common patterns of connectivity can be recognized.*

Global properties

One global property (Modularity coefficient), out of the 6 evaluated as functions of the graphs density, was found to be significantly altered in the PATs group with respect to HCs. Statistical significance of the differences measured in each group comparison (assessed after regressing-out the age-related contribute to variance the ANCOVA) is reported in these sections in term of p-values indicating probability of the null-hypothesis $\alpha_i = 0$, referring to the model in equation 4.1).
Results of the measure of Giant-component size as a function of the density are reported in the plots in figure 5.11, for both the subjects groups. As expected, in both cases, as densities reach $\sim 50\%$ almost all the graphs are fully connected, and giant-component size approaches its maximum value (34). In the figure also the results obtained with the randomized graphs (dashed colored lines) are reported; interestingly, they are systematically slightly higher, indicating a pronounced modularity of the ON graphs (and a minor overall integration), with respect to the randomized ones. The comparison between the two groups showed no statistically significant difference.
In figure 5.12 the average values of Global Efficiency are represented as a func-

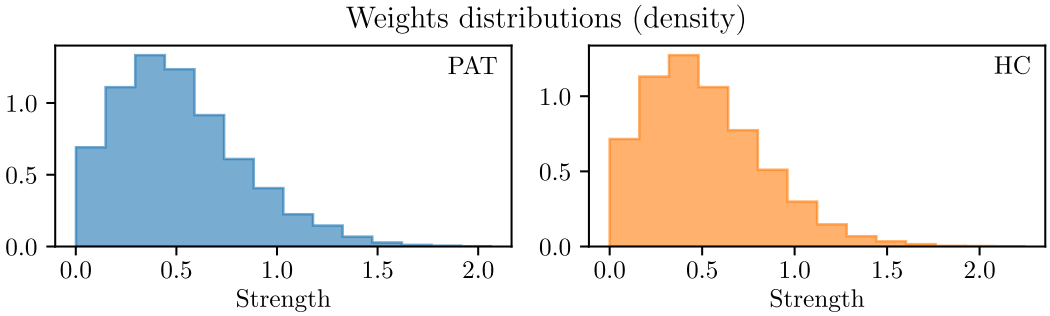

Figure 5.10: *Distributions of weights in the total set of PATs and HCs matrices (normalized; zero-weights were not considered). The two distributions do not differ significantly.*

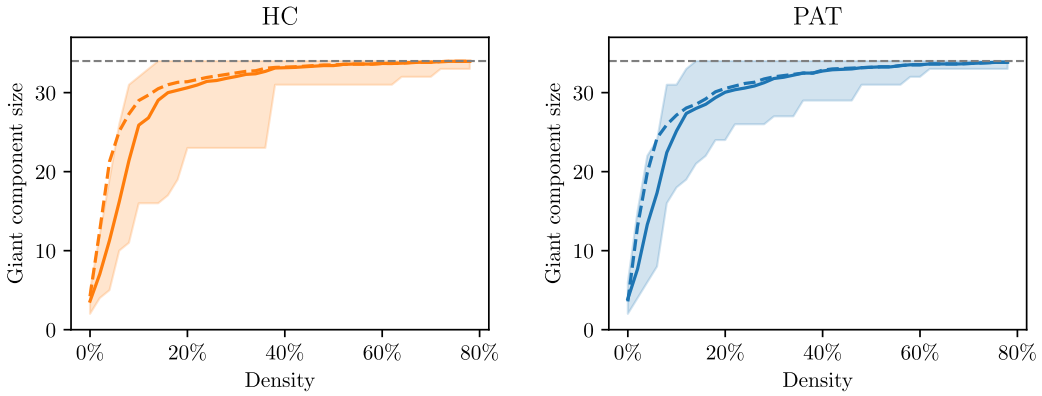

Figure 5.11: *Giant component size vs density. Dashed lines indicates the values obtained with the randomized matrices; hues represents whole intervals between minimum and maximum values.*

tion of the density, obtained for the two groups; values relative to randomized graphs are plotted as well. A direct comparison between the absolute integral values of the two groups seems to indicate no differences (in the considered interval of densities); by comparing normalized results instead, a difference with a statistical significance close to the p=0.05 threshold is observed (PAT > HC : $p = 0.051$). Notice that, even though not always seriously affecting the results, in some cases normalization of graph-metrics with appropriate random equivalents can be decisive, and normalized results should be considered more reliable than the absolute ones. In figure 5.13 the normalized values and the integral values used for comparison are plotted.

Characteristic path length, being an inverse but essentially equivalent measure of Global Efficiency, also presents a relevant difference between the groups, though not statistically significant (HC > PAT : $p = 0.052$). In figure 5.14 the average trends, the average normalized trends and the comparison between the

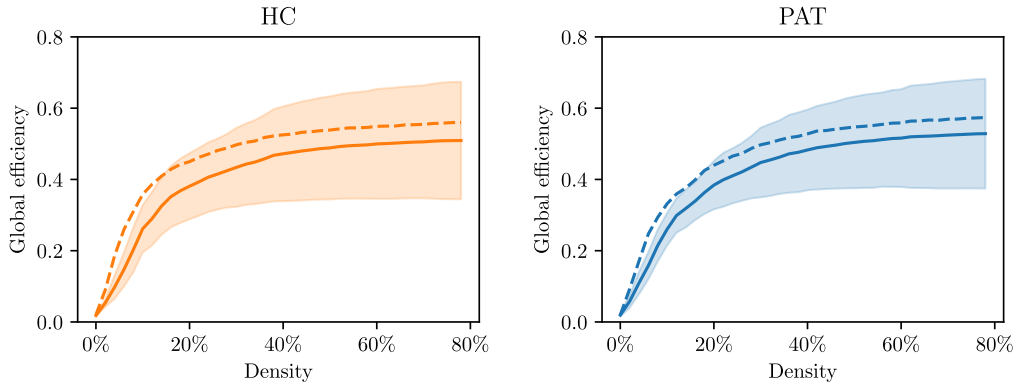

Figure 5.12: *Global Efficiency of ON-restricted graphs, as a function of the density. Dashed lines indicates the values obtained with the randomized matrices; hues represents intervals between minimum and maximum values.*

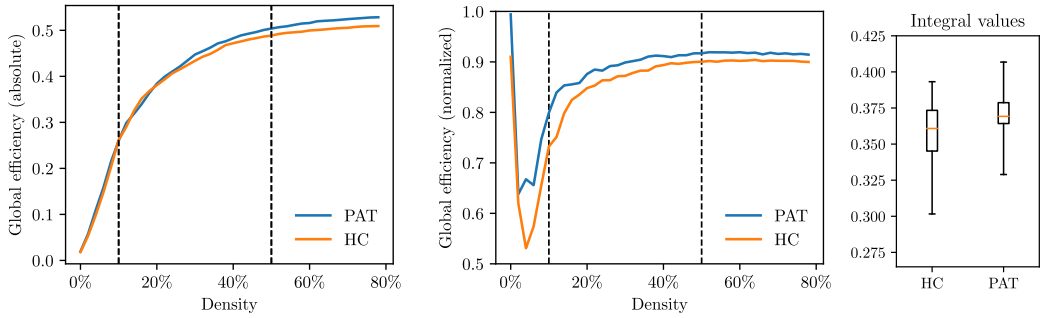

Figure 5.13: *Comparison between Global Efficiency average values of the two groups of ON-restricted graphs, for absolute and normalized measures; the boxplots on the right shows the comparison between integral values. PATs group seemed to show slightly higher values, but the difference was not significant.*

integral values are represented.
These results indicate that functional networks of the PAT group seems to be characterized by slightly higher level of integration with respect to HC, which in graph-theory is commonly interpreted as a more efficient information transfer between topologically distant regions. However this difference wasn't found to be statistically significant.

Consistently with the previous results, the comparison of the Modularity Coefficients of the graphs showed a statistically significant difference (HC $>$ PAT : $p = 0.019$), highlighting a more pronounced modular structure in the HCs group, with respect to the PATs; in figure 5.15 the results obtained for this metrics (absolute and normalized trends) and the relative comparison between integral values are shown.

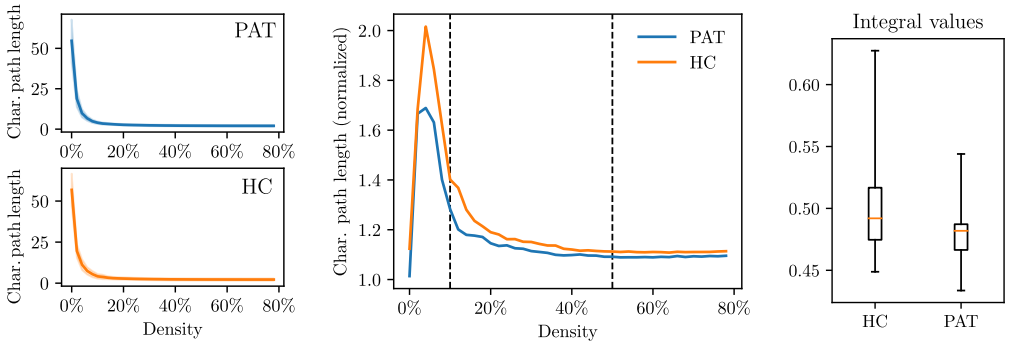

Figure 5.14: *Comparison between Characteristic Path Length average values of the two groups, for absolute and normalized measures. From the comparison between integral values, no statistically significant differences were highlighted.*

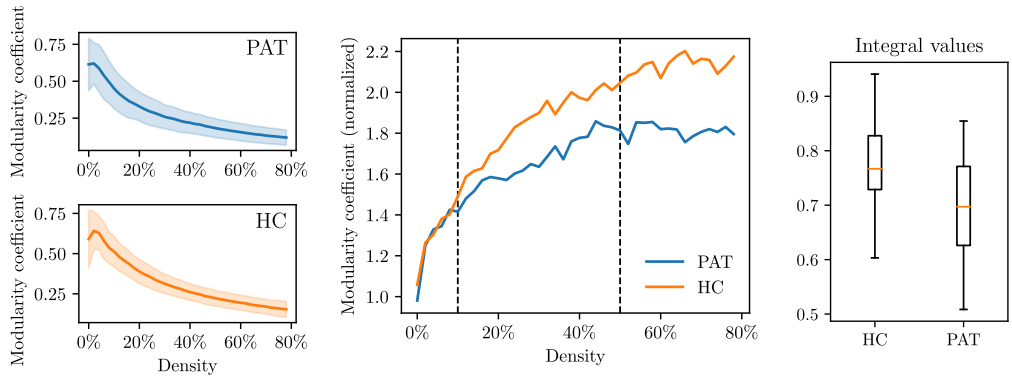

Figure 5.15: *Comparison between Modularity coefficient average values of the two groups, for absolute and normalized measures. From the comparison between integral values, a statistically significqant difference emerges (HC>PAT).*

Results of the measurement of Small-Worldness and Assortativity Coefficient (absolute values) are reported in figure 5.16 and 5.17. Small-Worldness is defined by means of normalized values of Clustering Coefficient and Characteristic Path Length, hence it doesn't need to be normalized and it can be directly compared; normalization wasn't performed on Assortativity Coefficients because, due to the presence of small values ($< 10^{-4}$), it would make them oscillate abruptly. For both groups Assortativity Coefficients are characterized by a high within-group variabiliy (noisy measure), but are mainly distributed at low positive values (graphs are weakly *assortative*). Small-Worldness on the other hand is significantly higher than one, decreasing as a function of the density. The results of the comparisons of integral values computed in the above-mentioned range of densities are plotted as well. In these two cases no statistically significant differences were appreciated.

In table 5.4 are summarized the results of the between-group comparison and details about statistical signifcance, as computed with the ANCOVA.

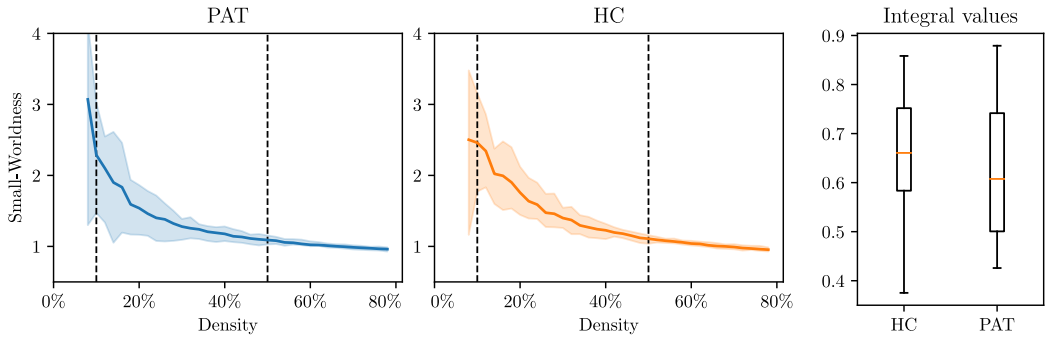

Figure 5.16: *Small-Worldness values computed for the two groups, as function of the density of the graphs; as expected, the graphs showed moderate Small-World characteristics (as this values is strictly larger that one). From the comparison between integral values, no statistically significant differences were found.*

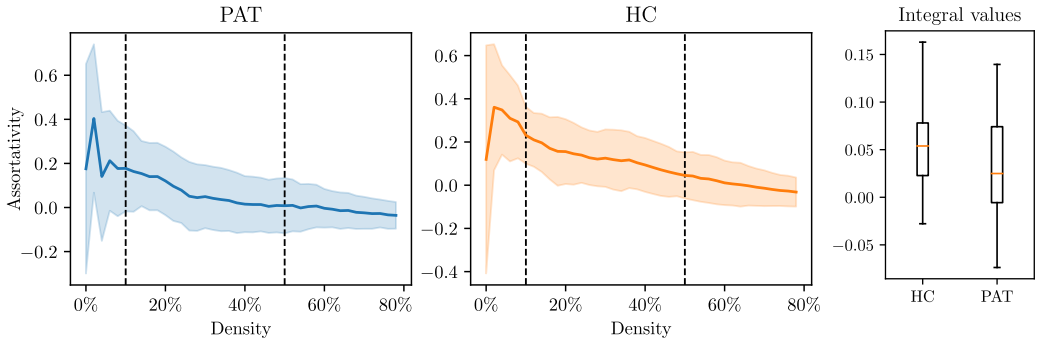

Figure 5.17: *Assortativity coefficient values computed for the two groups, as functions of the density of the graphs; no statistically significant differences were found in the comparison between the integral values.*

Table 5.4: *Results of the between-groups comparison of weighted graphs' global measures. The values estimated for PATs and HCs, the difference between the two, and the p-value representing the significance of the difference are reported.*

Property	PAT	HC	$\lvert\hat{D}\rvert$	p-value	Direction
Giant Component Size	0.4176	0.4128	0.005	0.300	PAT>HC
Global Efficiency	0.3734	0.3608	0.013	0.051	PAT>HC
Characteristic Path Length	0.4771	0.4979	0.02	0.052	HC>PAT
Modularity coeficient	0.6982	0.7730	0.07	0.019	HC>PAT
Small-Worldness	0.6844	0.7346	0.05	0.202	HC>PAT
Assortativity coefficient	0.0378	0.0638	0.026	0.107	HC>PAT

Local properties

The 6 considered local properties of weighted graphs were: node's Degree and Strength, Local Efficiency, node's Betweenness Centrality, Clustering Coefficient, Participation Coefficient and Z-Score (the last two based on a a-priori defined modular structure from Campbell Arnold et al. results [7]).
At a local level individual variability turned out to be even more pronounced than it was for global measures, in particular for the most complex metrics such as Betweenness Centrality. As an example, in figure 5.18 the trends of the 6 local measures obtained for the 33th node (*right rostral Cingulate Cortex* - CINr_R), averaged among all the subjects of each group, are reported: despite individual variability, common courses can be recognized. The Degree and Strength trends are actually much similar to those observed for all the other nodes of the network, for understandable reasons (they tend to grow for increasing graph Density, with slight differences depending on topological characteristics); Participation Coefficient and Z-Score behaviours can be noticeably different among different nodes of the networks, since they also depend on the internal organization of the module they belong to; Betwenness Centrality, Clustering Coefficient and Local Efficiency trends are generally similar across nodes, showing characteristic peak values at low densities and then stabilizing on slowly varying values.

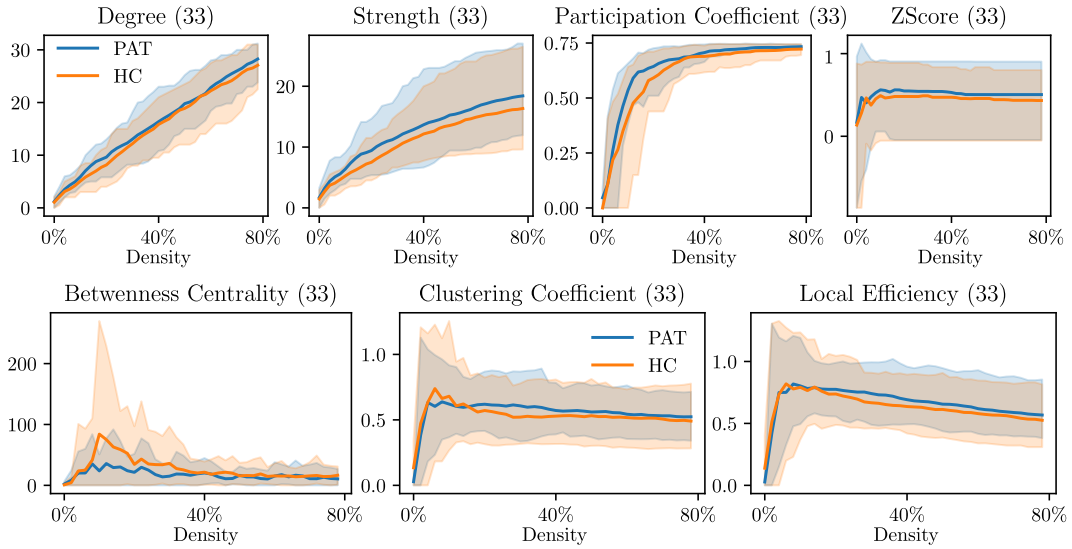

Figure 5.18: *Local properties measured for node 33 (rostral cingulate cortex - CINr) as functions of the graph densities, for PATs and HCs.*

In figure 5.19 the measured values for node 17 (*right anterior Insula* - INSa_R) are shown, for comparison. The group comparison of local measures (as previously explained, performed by comparing integral values of the measures as functions of the density, through an ANCOVA with age as regression variable) identified a number of differences reaching the uncorrected $p = 0.05$ level of

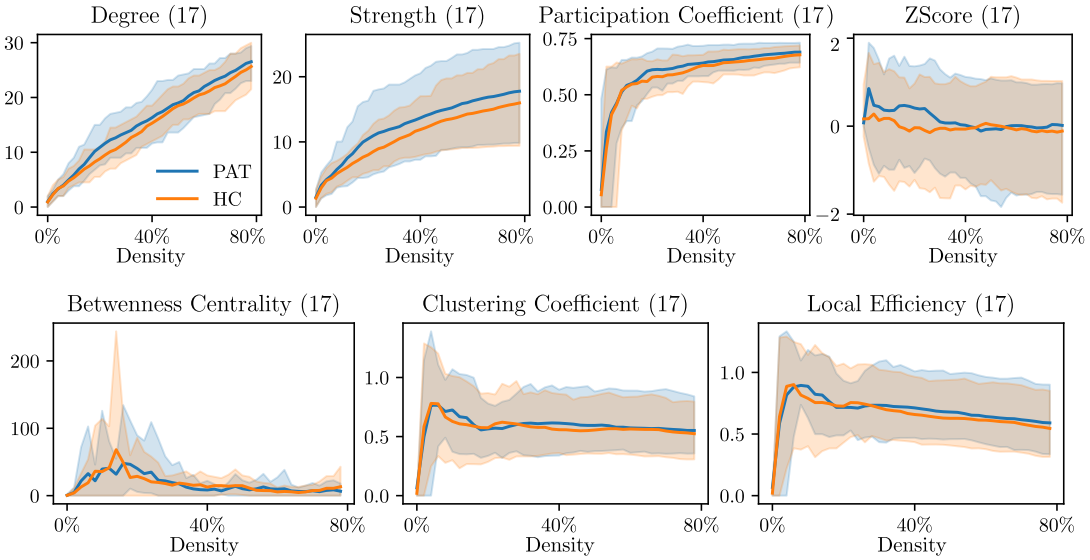

Figure 5.19: *Local properties measured for node 17 (anterior Insula - INSa) as functions of graph densities, for PATs and HCs.*

significance; two of them, regarding the Degree and the Strength of the right Thalamus (THL_R), were found to be statistically significant after the multiple-comparisons correction. A summary of the most relevant detected differences is reported in tab. 5.5. Relatively to the local alterations of connectivity involving the THL_R, two aspects should be highlighted. First, measures of Degree and Strength of graph nodes are clearly not independent, as they both reflect the overall connectivity of a node; being highly correlated measures, it is easy to find similar alterations. Second, it is interesting to notice that in its corresponding bilateral node (THL_L), a trend towards a similar alteration is observed, though not statistically significant. In figure 5.20 the plots of $THL_{R\text{-}L}$ Degree and the relative integral-values comparison are reported; in figure 5.21 those of their Strength.

Average values of Local Efficiency and Clustering Coefficient were computed as well (averaging the results obtained for all the nodes of a single subject's graphs), as they can give further characterization to the topology of networks at a global level. These measures should be considered as *indirect*-global properties. Their trends, as functions of the density, are reported in figure 5.22, together with the results of the group comparisons (no differences were detected between PATs and HCs).

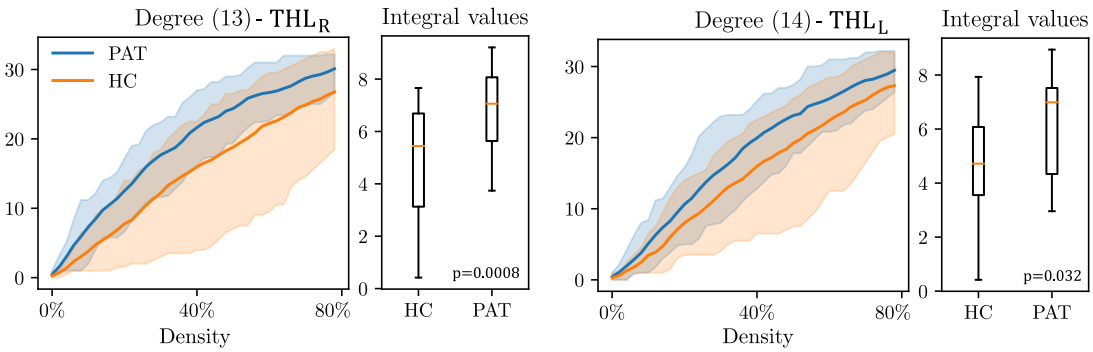

Figure 5.20: *Values measured for the Degree of the left and right Thalamus ($THL_{L\text{-}R}$), as functions of the density; in case of THL_R, a statistical significant difference was found.*

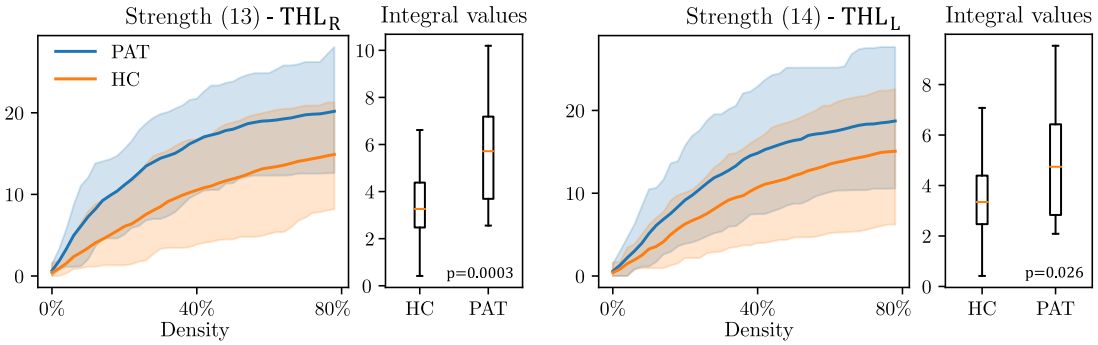

Figure 5.21: *Values measured for the Strength of the left and right Thalamus ($THL_{L\text{-}R}$), as functions of the density; in case of THL_R, a statistical significant difference was found.*

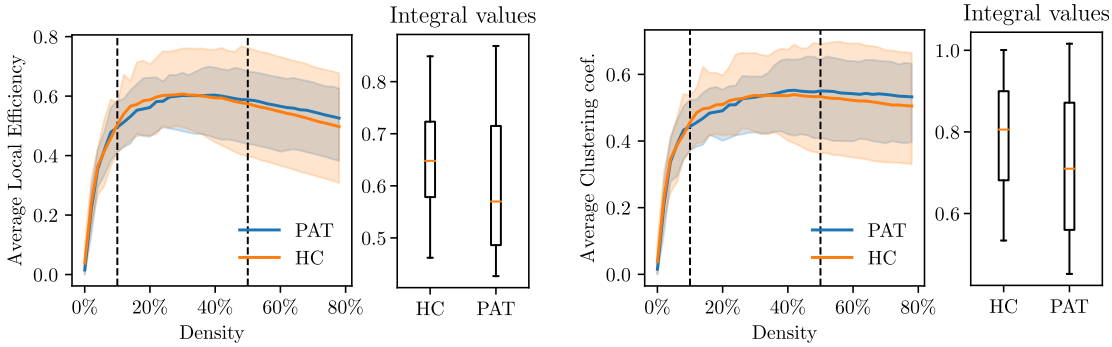

Figure 5.22: *Average trends of local properties as functions of the density: Left - Local Efficiency; Right - Clustering Coefficient; no statistically significant difference was found from the comparison of the integral values.*

Table 5.5: *Results of the between-groups comparison of weighted ON graphs' local measures, in terms of uncorrected p-values. Highlighted p-values are those which were significant after multiple-comparisons correction.*

ROI (node)	Property	p-value	Direction
Oolf_L (2)	Betweenness c.	0.049	HC>PAT
APC_L (4)	Degree	0.045	HC>PAT
AMY_R (5)	Clustering coef.	0.018	HC>PAT
	Local Efficiency	0.021	HC>PAT
aHIP_L (8)	Strength	0.039	HC>PAT
	Z-Score	0.0052	HC>PAT
$\mathbf{THL_R}$ (13)	**Degree**	0.00079	PAT>HC
	Particip. coef.	0.020	PAT>HC
	Strength	0.00026	PAT>HC
	Z-Score	0.0030	PAT>HC
THL_L (14)	Degree	0.031	PAT>HC
	Strength	0.026	PAT>HC
INSai_R (15)	Particip. coef.	0.027	PAT>HC
INSd_L (20)	Degree	0.034	PAT>HC
INSv_L (22)	Particip. coef.	0.012	HC>PAT
	Z-Score	0.0090	HC>PAT
CINa_R (31)	Particip. coef.	0.022	PAT>HC
CINa_L (32)	Betweenness c.	0.0081	HC>PAT

NBS

As explained in section 4.4.3, NBS analysis was performed on the graphs in the range of densities $10 - 50\%$, comparing connectivity matrices of PATs and HCs. At the end, each link was characterized with a *alteration score* - AS (> 0 for each link found altered at least at one density. AS was previously defined in equation 4.2). Non-zero ASs are summarized in table 5.6; notice that, even though formally ASs does not indicate a level of statistical significance, all of these links resulted significantly altered for at least one density in the considered range.
These NBS results globally indicate a cluster of alteration which in most cases involved the THL_R as a central node, hence are consistent with the results obtained from the comparison between the graph's topological measures comparisons (in particular the local measures). The cluster of alteration also strongly

involved anterior and posterior portions of the right Insula ($INSai_R$, $INSa_R$, $INSp_R$, $INSv_R$), of the right Hippocampus ($aHIP_R$, $pHIP_R$) and of the Cingulate cortex ($CINa_R$, $CINr_R$); some alterations were found also in the bilateral counterpart, but in general with much greater statistical significance in the right-hemisphere. The most significant alteration was detected in the connectivity between THL_R and the $pHIP_R$.
Figure 5.23 reports a schematic of the most significant alterations, according to the measured ASs. The set of altered connections is also represented on the average connectivity matrices of PATs and HCs in figure 5.24.

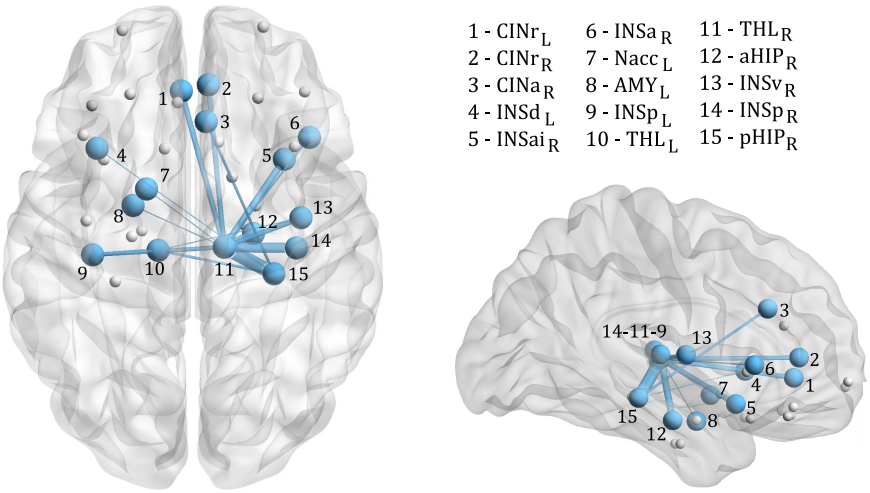

Figure 5.23: *Representation of the altered connections of the weighted ON-restricted graphs, as found by the NBS analysis. Blue nodes are those having at least one connections with $AS > 0$ (grey nodes represent the other ON regions, having all the connections with $AS = 0$); width of the connections represents the AS. This plot was realized with the BrainNet Viewer software [93].*

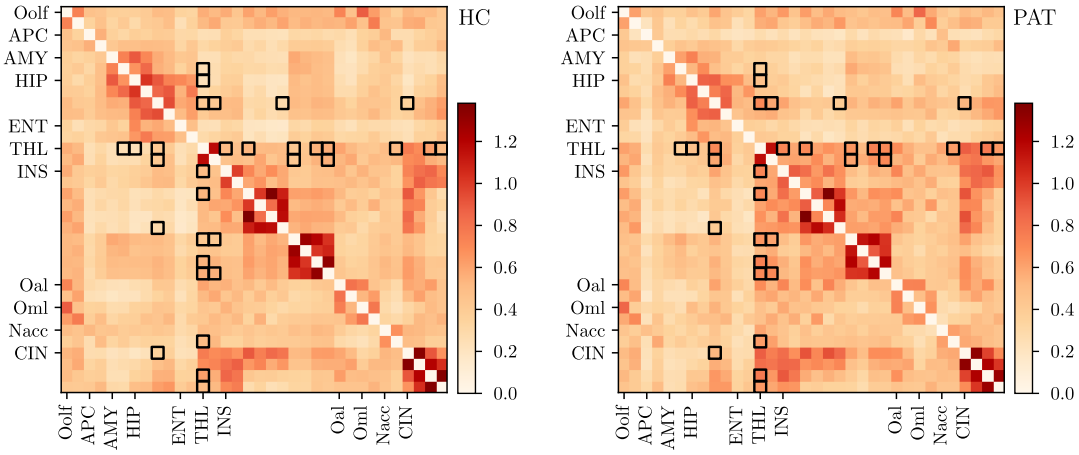

Figure 5.24: *ASs altered connections, as found by NBS analysis, visualized on the average connectivity matrices of PATs and HCs. All the connections found to have a AS* > 0 *are highlighted with black squares.*

Table 5.6: *Results of the NBS analysis in terms of alteration scores. All the altered connections are represented with corresponding AS value; those with AS* > 1.0 *are highlighted.*

Connection	AS
AMY_L (6) $\leftrightarrow$ THL_R (13)	0.1465
$aHIP_R$ (7) $\leftrightarrow$ THL_R (13)	1.5025
$pHIP_R$ (9) $\leftrightarrow$ THL_R (13)	2.6265
$pHIP_R$ (9) $\leftrightarrow$ THL_L (14)	0.4960
THL_R (13) $\leftrightarrow$ $INSai_R$ (15)	1.2329
THL_R (13) $\leftrightarrow$ $INSa_R$ (17)	0.3347
$pHIP_R$ (9) $\leftrightarrow$ $INSd_L$ (20)	0.1829
THL_R (13) $\leftrightarrow$ $INSv_R$ (21)	0.9835
THL_L (14) $\leftrightarrow$ $INSv_R$ (21)	0.0871
THL_R (13) $\leftrightarrow$ $INSp_R$ (23)	1.8775
THL_R (13) $\leftrightarrow$ $INSp_L$ (24)	0.7978
THL_R (14) $\leftrightarrow$ $INSp_L$ (24)	0.7355
THL_R (13) $\leftrightarrow$ $NAcc_L$ (30)	0.0599
$pHIP_R$ (9) $\leftrightarrow$ $CINa_R$ (31)	0.5323
THL_R (13) $\leftrightarrow$ $CINr_R$ (33)	0.9485
THL_R (13) $\leftrightarrow$ $CINr_R$ (34)	1.0192

5.3.2 ON-restricted binary graphs

As expected, the measures computed on the binary versions of graphs were generally consistent with the corresponding from weighted graphs. Similar behaviours can be noticed in all the global properties trends.
Most of the comparisons between the measurements performed on binary graphs didn't reach the statistical level of significance, with the exceptions of the THL_R Degree (Degree measure is in fact totally equivalent in weighted and binary graphs) and of the Modularity Coefficients at a global level ($p = 0.021$, hence with a lower significance with respect to the weighted networks case); in general, considering the alterations with $p < 0.05$ (not corrected), it can be observed that they were all highlighted in the weighted analysis as well, with equal or lower statistical significance, except for Local Efficiency and Clustering coefficient of the $CINa_L$ (node 22).
In figure 5.25 the measured trends of Global Efficiency, Characteristic Path Length, Small-Worldness and Modularity Coefficient as functions of the density of the graphs are plotted (plot of the Giant Component size corresponds to the one reported in figure 5.11, for the weighted case).
In table 5.7 the results of the comparisons between local measures of the two groups are reported.

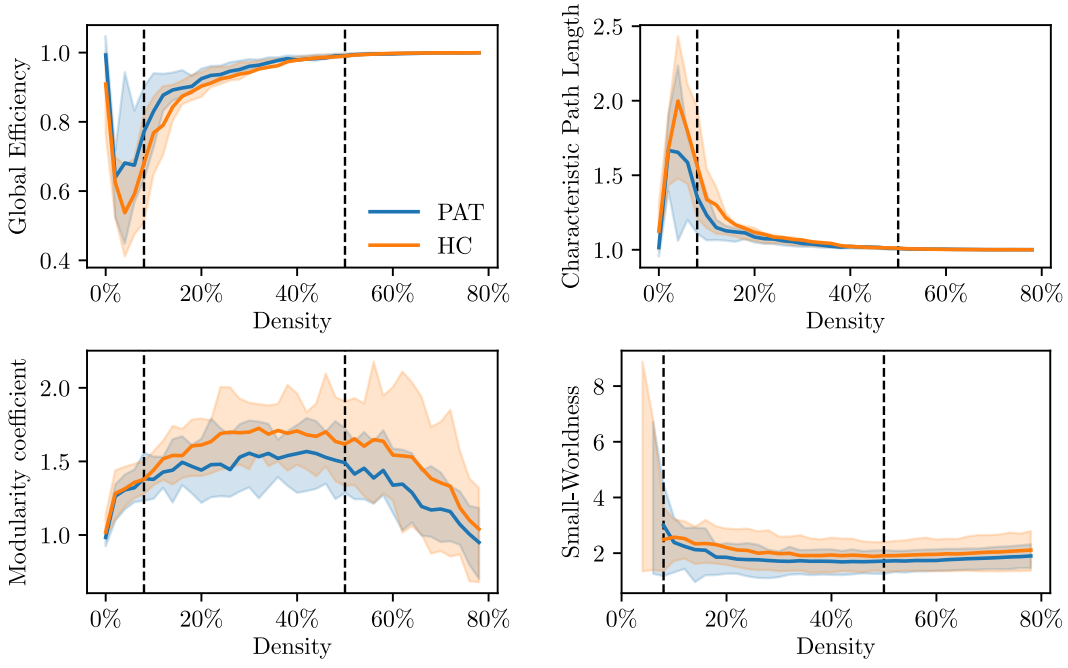

Figure 5.25: *Binary graphs global measurements as functions of the graphs density: Global Efficiency, Characteristic Path Length, Small Worldness, Modularity Coefficient; hues represents intervals between minimum and maximum values.*

Table 5.7: *Results of the between-groups comparison of binary ON graphs' local measures. The highlighted p-values are those which remained after multiple-comparisons correction.*

ROI (node)	Property	p-value	Direction
APC_L (4)	Degree	0.045	HC>PAT
AMY_R (5)	Clustering coef.	0.020	HC>PAT
	Local Efficiency	0.025	HC>PAT
THL_R (13)	**Degree**	0.00079	PAT>HC
THL_L (14)	Degree	0.031	PAT>HC
$INSd_L$ (20)	Degree	0.034	PAT>HC
$CINa_L$ (32)	Betweenness c.	0.0045	HC>PAT
	Clustering coef.	0.029	HC>PAT

5.3.3 Whole-brain graphs

An example of whole-brain connectivity matrix (246×246, Z-transformed values) is represented in figure 5.26 (average connectivity matrix of the HCs group). Also in this case, average connectivity values of PATs and HCs groups were compared and submitted to a t-test for assessing potential group-differences, which highlighted no statistical significance.
In figure 5.27 the observed trends of Giant Component Size versus the graphs density for PATs and HCs are represented; from the comparison of the integral values computed in the range of densities $5 - 50\%$, after regressing-out the nuisance variables with the ANCOVA, no relevant difference was found.
In figure 5.28 the measures of Global Efficiency and Characteristic Path Length are reported; in figure 5.29 and 5.30, respectively, the trends of Modularity Coefficient and Small-Worldness are represented; even in these cases no statistically significant alteration was found between the two groups. Therefore, from our measurements, no alteration could be observed in the global topological organization of whole-brain graphs. The results of group comparisons of global measures are summarized in table 5.8.

For what concerns graph topological properties at a local level, some differences were highlighted in the ANCOVA regressions, though not significant when corrected for multiple-comparisons (notice that in this case corrections where much more severe than in the ON-analysis, due to the larger number of comparisons performed). However, it should be mentioned that alterations consistent with those reported by the previous ON-analysis were observed: in particular, two of the ROIs (nodes 232-238, mPFtha_r and tTtha_r using Brainnettome de-

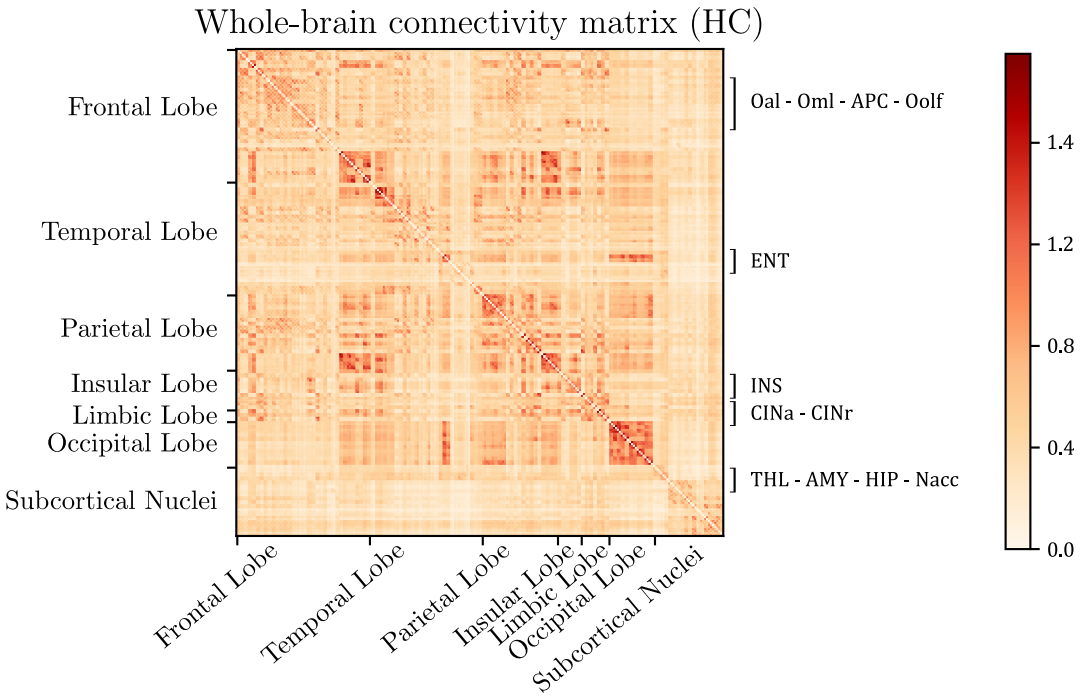

Figure 5.26: *Example of whole-brain connectivity matrix (average connectivity matrix of the HCs group; correlation coefficients expressed as Z-transformed values). Nodes are ordered following the anatomical areas they belong to, indicated on the left (and below). Regions which are part of the ON are indicated on the right.*

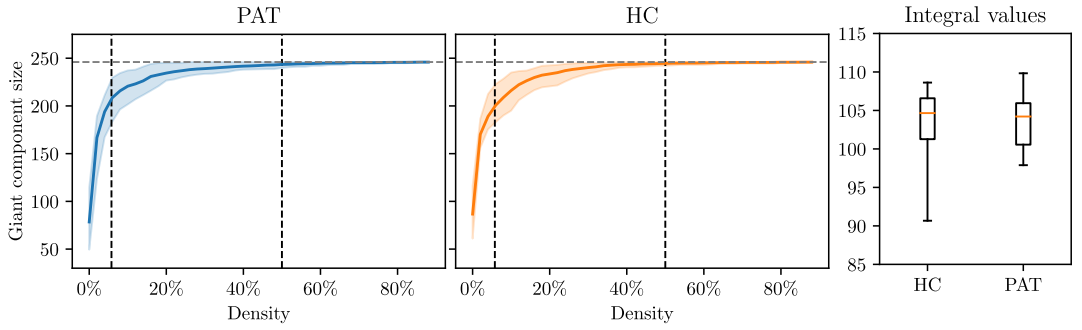

Figure 5.27: *Giant Component Size values as functions of the density, for PATs and HCs groups (solid lines are the average values; vertical dashed lines represent the interval of integration; horizontal dashed line is the maximum value - 246). Box-plot represent the comparison between integral values. Difference was not statistically significant.*

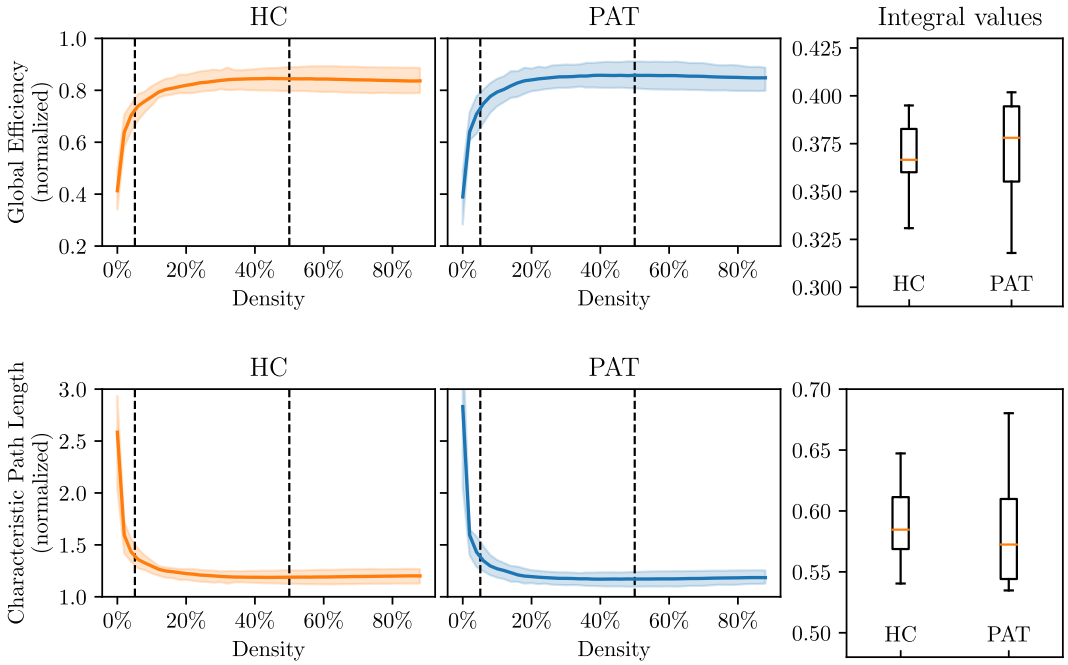

Figure 5.28: *Global Efficiency and Characteristic Path Length values as functions of the density, for PATs and HCs groups (solid lines are the average values; dashed lines represent the interval of integration). Box-plots represent the comparisons between integral values. Differences were not statistically significant.*

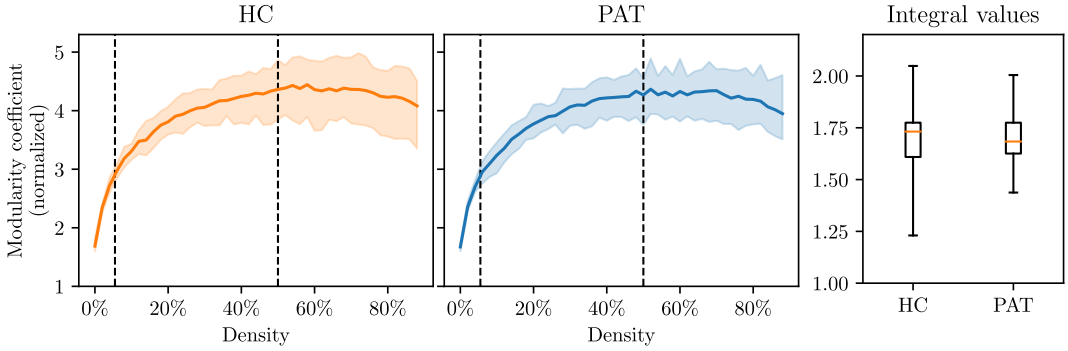

Figure 5.29: *Modularity coefficient values as functions of the density, for PATs and HCs groups (solid lines are the average values; dashed lines represent the interval of integration). Box-plot represent the comparison between integral values. Discrepancy was not statistically significant.*

Table 5.8: *Results of the between-groups comparison of weighted WB graphs' global measures. No differences were detected.*

Property	p-value	Direction
Giant Component Size	0.74	HC>PAT
Global Efficiency	0.82	PAT>HC
Characteristic Path Length	0.79	HC>PAT
Modularity coeficient.	0.72	HC>PAT
Small-Worldness	0.81	PAT>HC

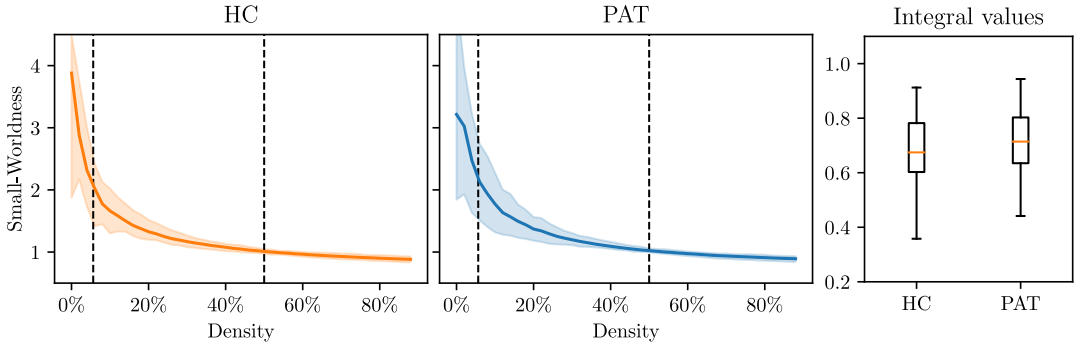

Figure 5.30: *Small-Worldness values as functions of the density, for PATs and HCs groups (solid lines are the average values; dashed lines represent the interval of integration). Box-plot represent the comparison between integral values. Discrepancy was not statistically significant.*

nominations [84]) corresponding to the THL_R region used for the ON-restricted analysis, were observed to have an increased connectivity in the PATs group. The results of the comparisons of local measures are summarized in table 5.9.

The same NBS analysis performed on ON-restricted graphs was repeated on the set of whole-brain matrices, but in this case no clusters of alteration were detected (for any density in the range $10 - 50\%$); this result is consistent with those obtained for the local topological properties (i.e. no p-value overcoming the multiple-comparisons correction).

Table 5.9: *Results of the between-groups comparison of weighted whole-brain graphs' local measures: most relevant alterations. ROI denonomination is taken from Brainnetome Atlas, please refer to [84] (annotations in bold format indicate that the ROI was included in a region selected also for the ON-restricted graph). None of the reported differences was found to be statistically significant after correction for multiple comparisons.*

ROI (Node)		**Property**	**p-value**	**Direction**
A8dl_r (4)		Particip. coef.	0.013	PAT>HC
A44d_r (30)		Degree	0.018	PAT>HC
A38m_l (69)		Degree	0.018	HC>PAT
A20cl_l (99)		Clustering coef.	0.0066	HC>PAT
		Local Efficiency	0.0030	HC>PAT
A5l_l (129)		Degree	0.014	HC>PAT
A40rd_l (139)		Degree	0.0072	HC>PAT
A24cd_r (184)		Degree	0.015	PAT>HC
rCunG_r (192)		Betweenness c.	0.013	HC>PAT
dlPu_l (229)		Clustering coef.	0.015	PAT>HC
dlPu_r (230)		Clustering coef.	0.011	PAT>HC
		Local Efficiency	0.012	PAT>HC
		Particip. coef.	0.017	PAT>HC
mPFtha_r (232)	$\mathbf{THL_R}$	Degree	0.011	PAT>HC
rTtha_r (238)	$\mathbf{THL_R}$	Betweenness c.	0.010	PAT>HC
		Degree	0.0091	PAT>HC
		Particip. coef.	0.0023	PAT>HC

5.3.4 Results after parcellation improvement

Final results obtained from the ON-restricted graph-analysis performed with the new set of ROIs (after the subject-specific improvement performed with the rsDPI algorithm) were essentially analogue to those illustrated before and highlighted the same alterations, with minor differences in the obtained p-values (for this reason they will not be reported extensively in this section; for those results please refer to section 5.3.1). However, some interesting results were obtained in a series of exploratory comparisons made between the average ROIs time courses and the connectivity matrices obtained with the standard method and those obtained with the inclusion of the parcellation improvement step.

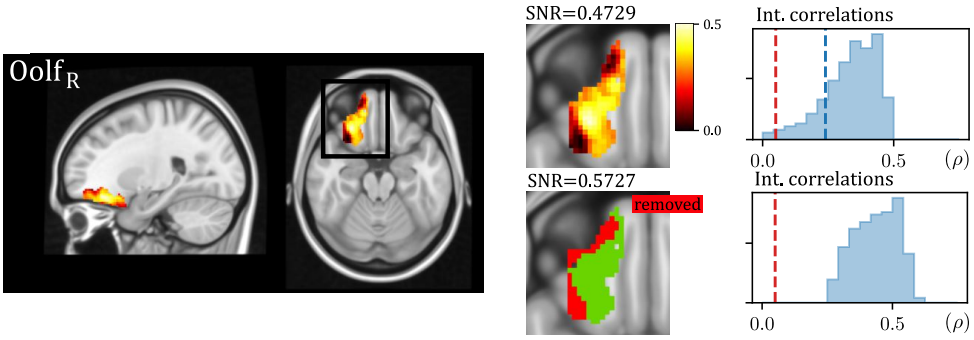

Figure 5.31: *Application of rsDPI algorithm on $Oolf_R$ of a subject from the HCs group: the heat-map indicating the measured internal correlation of each voxel inside the ROI is represented. Green-red map indicates the portions of the ROI preserved and removed after refining. Internal correlations before and after ROI finishing are reported in histograms (red line indicates $\rho = 0.05$; blue line the 20% inferior quantile).*

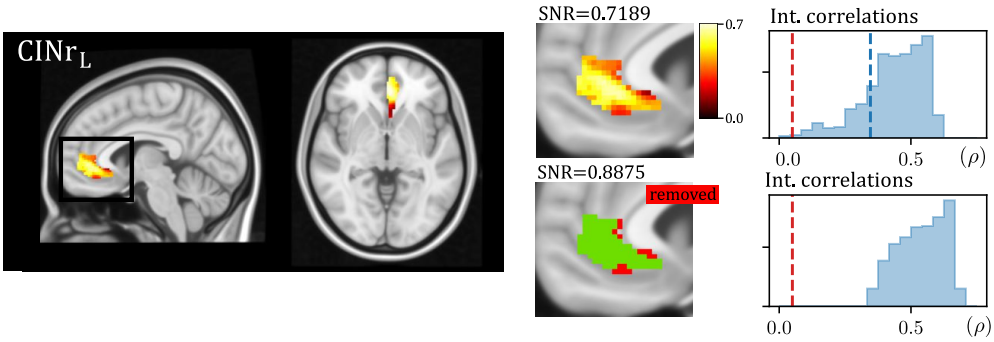

Figure 5.32: *Application of rsDPI algorithm on $CINr_R$ of a subject from the HCs group: the heat-map indicating the measured internal correlation of each voxel inside the ROI is represented. Green-red map indicates the portions of the ROI preserved and removed after refining. Internal correlations before and after finishing are reported in histograms (red line indicates $\rho = 0.05$; blue line the 20% inferior quantile).*

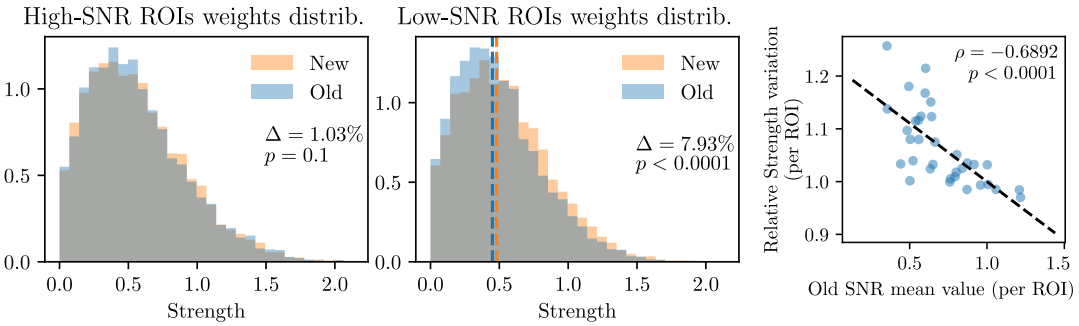

Figure 5.33: *Left: weights distributions of nodes corresponding the 6 highest-SNR ROIs, before and after parcellation improvement (no difference between the two). Center: weights distributions of nodes corresponding the the 6 lowest-SNR ROIs, before and after parcellation improvement (significant difference). Right - correlation between SNR of a ROI before the finishing and relative variation of its strength after finishing.*

Two examples of ROIs from the ON (Oolf_R and CINr_L) before and after parcellation improvement are represented in figures 5.31 and 5.32 (data taken as an example from a subject of the HCs group), together with the histograms representing the distributions of average correlation coefficients of the voxels inside each region. As it can be noticed, the most relevant effect is that raw-SNR increases after application of the algorithm: on average, each ROI's relative raw-SNR increase was +20.4% ($p < 0.0001$).
From the comparison between the total weights' distribution of the old set of matrices (obtained without the rsDPI step) and the new one (correlation matrices derived with the new time series), a statistically significant increase of the average connectivity value was observed ($+5.1\%; p < 0.0001$). An interesting alteration was found by analyzing separately the weights of the connections of the 6 ROIs with lowest raw-SNR (on average, before the application of the algorithm) and those of the 6 ROIs with highest SNR: in new matrices, weights of the connections of the ROIs with lower SNR were found to be significantly increased; weights of the ROIs with higher SNR did not (figure 5.33 - left); this observation was formalized by computing the correlation between the average raw-SNR of each ROI (before ROIs finishing) and the relative variation of the ROI Strength (after), which was shown to be significant (figure 5.33 - right). Finally, by comparing each ROIs' average raw-SNR before the application of the algorithm and the relative raw-SNR variation (new matrices/old matrices), a statistically significant correlation was observed (figure 5.34, left). No significant correlation was observed by comparing each subject's average SNR versus the same quantity (figure 5.34, right). A complete discussion of these results will be found in the next chapter.

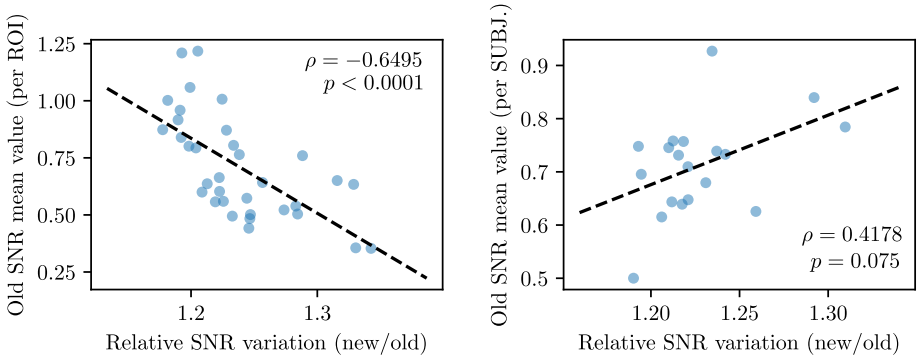

Figure 5.34: *Left - correlation between relative SNR variation after the parcellation improvement and old SNR of each ROI (statistically significant). Right - correlation between relative SNR variation after SNR variation and old average SNR of each subject (not significant).*

5.3.5 Results of the clinical evaluation

As assessed through the Sniffin' Sticks test, out of the total group of 23 patients, one had functional anosmia, twenty-one had hyposmia, and one patient had normosmia. The group average total score was 23.6±5.3, with normosmia cut-off being at 30.75 total score. Mean neuropsychological scores, corrected by age and education, are reported in Table 3 with the percentage of patients exhibiting impaired outcomes, defined as ≥95% of the tolerance limit of the normal population distribution. Memory and executive functions were the two cognitive domains mainly impaired. Specifically, short-term and long-term verbal memory were impaired in 9% and 13% of patients, while short-term and long-term visuospatial memory were impaired in 9% and 17% of patients. Moreover, in the executive function domain, deficits in the ability to inhibit cognitive interference and working memory deficits were found respectively in 10% and 13% of patients. Almost one-third of the patients had a pathological depression score, while three-fourth of patients had a pathological fatigue score, which is frequently reported in the long-COVID population.

Domain	NPS test	Raw score	Corr. score	Norm. val. c-o	% pat. s.
Cognitive screening	MoCA score	25.74±2.51	25.74±2.51	≥ 18.29	4%
Attention and Executive functions	Digit Span Backward	4.39±1.03	3.83±1.08	≥3.29	13%
	Stroop test (RT-sec)	13.10±6.89	22.77±7.24	≤36.91	10%
	Stroop test (Error)	0.29±0.90	3.25±1.15	≤4.23	5%
	TMT A	34.74±13.41	42.30±15.28	≤93 s	0%
	TMT B	88.22±30.69	119.55±42.38	≤282 s	0%
Verbal memory	AVLT immediate recall	49.26±11.16	41.69±9.30	≥28.53	9%
	AVLT delayed recall	10.09±3.41	7.76±3.13	≥4.69	13%
	Naming to verbal description animate	7.91±0.42	7.91±0.42	≥4.46	0%
	Naming to visual description animate	7.17±0.94	7.17±0.94	≥3.61	0%
	Naming to verbal description concrete inanimate	8.87±0.87	8.87±0.87	≥7.33	0%
	Naming to verbal description abstract inanimate	9.13±0.69	9.13±0.69	≥6.69	0%
	Digit Span Forward	6.13±0.87	5.51±0.83	≥3.75	0%
Visuo-spatial memory	Corsi's Block Test	5.13±1.22	4.63±1.08	≥3.75	9%
	ROCF delayed recall	21.24±6.59	17.35±6.01	≥9.47	17%
Language	Associative Fluency Test	40.13±12.79	32.17±12.19	≥17.35	4%
	Category Words Fluency Test	50.57±9.94	44.87±9.37	≥25	0%
Visuo-constructional abilities	ROCF copy	33.76±3.56	32.51±4.27	≥28.88	4%
Depression, anxiety and stress	DASS-21 Depression score	5.65±4.82	5.65±4.82	≤9	30%
	DASS-21 Anxiety score	5.09±3.42	5.09±3.42	≤7	13%
	DASS-21 Stress score	8.22±4.88	8.22±4.88	≤14	17%
Fatigue	MFIS Total score	35.00±20.12	35.00±20.12	>12.3	74%
	MFIS Physical score	15.00±10.90	15.00±10.90	>2.4	74%
	MFIS Cognitive score	16.52±8.92	16.52±8.92	>3.5	83%
	MFIS Psychosocial score	3.48±3.76	3.48±3.76	>6.4	4%

Table 5.10: *Results of the neuro-psychological assessment in patients. Pathological values were mostly exhibited in terms of fatigue and depression. Moreover, the memory domain (both verbal and visuospatial) was frequently altered. (Abbreviations: Corr. score = corrected score; Norm. val. c-o = normal value cut-off; % pat. s. = percentage of pathological scores.)*

5.3.6 Correlations with clinical scales

The results of the exploratory correlation analysis performed with the altered graph-measures of the PATs group (global Modularity coefficient and Degree and Strength of the THL_R, in ON-restricted graphs) and corresponding individual clinical scores are summarized in table 5.11. Only the most significant results are reported, in terms of correlation coefficients - ρ and corresponding raw p-values.
The scores obtained in the Sniffin-Tests were found to be positively correlated with the Modularity coefficient (including age as covariate), with p-values reaching p=0.0095 for the threshold-test (*sniff-TH*) and p=0.024 for the total score (*sniff-TOT*). Two short-term verbal memory tests (*Auditory Verbal Memory Test* with immediate recall - AVLT (IMM) and the *description-based object naming* - Obj. Naming) were found to be negatively correlated with the Strength of THL_R (including age and education level as covariates), both with p=0.015. By correcting for multiple comparisons in this case, no significant correlation is observed, though interesting trends were highlighted. Linear correlations are plotted in figure 5.35 and 5.36.

Table 5.11: *Results of the correlations between altered graph measures (* indicates normalized measures) and individual results in clinical tests. Only most significant correlations are reported, even though none of the obtained p-values reached the p=0.05 of significance after multiple comparison correction.*

Clinical test	**Measure**	p-value	ρ
sniff-TH	Modularity c.	0.0095	0.59
	Modularity c.*	0.027	0.52
sniff-TOT	Modularity c.	0.032	0.51
	Modularity c.*	0.024	0.53
AVLT (IMM)	Strength (THL_R)	0.015	-0.59
Obj. Naming	Degree (THL_R)	0.017	-0.59
	Strength (THL_R)	0.015	-0.59

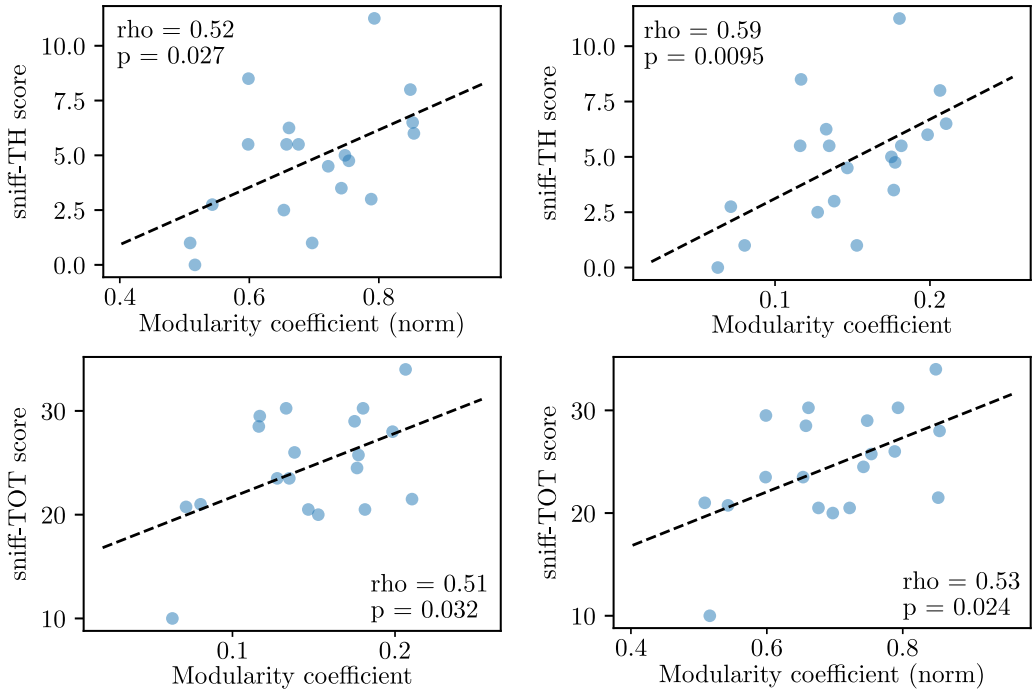

Figure 5.35: *Significant positive correlations between global Modularity coefficient (integral values) of the ON-restricted weighted graphs and scores in the Sniffin-Sticks' threshold (sniff-TH) and total (sniff-TOT) tests, for the subjects of he PATs group; results are shown for both normalized and absolute values of the graph measure.*

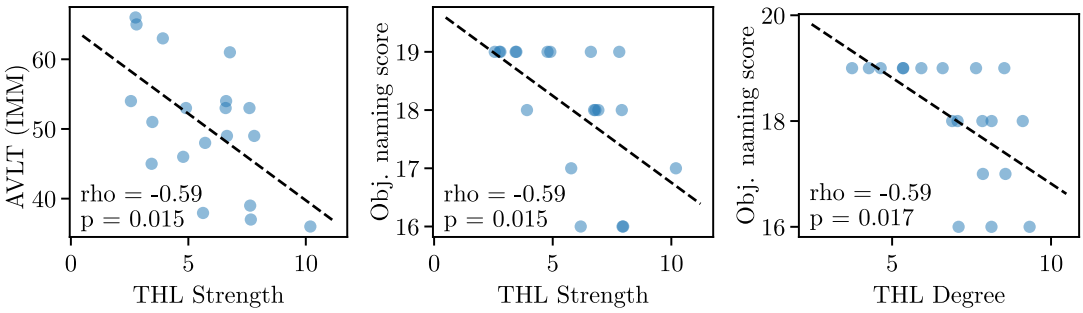

Figure 5.36: *Significant negative correlations between THL_R's altered measures (Strength and Degree) measured in the ON-restricted weighted graphs and scores in the cognitive tests (Obj. Naming and AVLT-IMM), for the subjects of the PATs group.*

Chapter 6

Discussion

Seed-based analysis

The main result obtained in the first part of the study (i.e. seed-based analysis) is that no significant differences in the connectivity of the 6 pre-established *core* olfactory ROIs with the rest of the brain was detectable between PATs and HCs groups, neither considering the seeds one at a time nor by using a single mask with all the seeds together; the difference which got closer to the statistical significance limit of corrected p-value = 0.05, involved the connectivity of the Oolf_{R} and a small cluster of voxels in the right parietal lobe (HC>PAT, p=0.063). The seed-based analysis conducted with the PCC (a *core* seed of the DMN) was performed as a validation of the methodology; also in this case no differences were detected between the connectivity patterns of the two groups of subjects (p>0.15).
A secondary goal of this part of the study was to obtain a probabilistic localization of the ON, as a result of the seed-based analysis performed with the 6 ROIs together; the example of the DMN in fact, showed that a meaningful localization of a major RSN is possible with a seed-based approach (in particular by applying a dual-regression with the core regions of the network, averaging the individual results and randomizing them in order to give a statistical relevance to the group-maps) and the results have a good correspondence with what is reported in literature (figure 5.1). However, in the case of the ON (in both versions, with spherical and anatomical input seeds) a statistically robust localization of the network could not be depicted, as within-group consistency of the individual spatial maps was too low. From a qualitative inspection of the individual maps, anatomical seeds seemed to produce stronger correlation maps, with a greater overlay between peaks of significance and grey matter and higher bilateral connectivity, but no improvements were observed in terms of group-averaged network localization.
To sum up, the failed attempt of localization of the ON is presumably attributable on one hand to the fact that this network is intrinsically "weak"

compared to the others major RSNs (in the sense that its internal correlation is weaker than, for example, that of the DMN) and on the other hand to the fact that core regions of the ON are placed in critical positions for EPI measurements, due to the presence of invasive artifacts and different types of noise. Besides, the results obtained by the analysis with separated seeds seem to indicate that no group-differences there exist, but it could also mean that the method wasn't sensitive enough to spot minor alterations.

Group-ICA

Among the results of the group-ICAs performed at different dimensions (30 - 50 - 100 - *undefined*) a number of ICs where selected as related to the ON (and then as potential candidates for the following dual-regression analysis). Components found at low dimensions were noticeably larger, involving wider regions of the brain and uncovering more correlations between spatially distant regions; given that the aim of this decomposition was to find components of the ON as large as possible, the (4) ICs from the 30-dimensions analysis were chosen.
The results of the group-comparison between individual maps (derived with the dual-regression of the 4 selected ICs) showed no alterations reaching the level of statistical significance $p<0.05$ after FWER correction. The most relevant alterations involved the IC2 (CINa, OFC and INSa), with a minimum corrected $p=0.11$ (PAT>HC), and the IC4 (INSa, middle temporal gyrus), with minimum corrected $p=0.12$ (HC>PAT).
Similarly to the seed-based analysis presented in the previous section, the group-ICA analysis was oriented toward two different objectives. The first was to identify the ON independent contribution to the total signal in terms of ICs, as decomposed by the group-ICA: though not in a unique component (precluding a proper localization of the network), ON-related activations were recognized in 4 different ICs (with IC2 being the most similar to a complete localization of the network). The second was to perform a group-comparison with the individual results of the dual-regression; consistently with the results of the seed-based analysis, no macroscopic alterations were detected in the connectivity of the core ON regions with the rest of the brain.

Graph analysis

The employment of graph-models to analyse the available data turned out to be the most sensitive method for detecting differences between the two groups of subjects. In particular the ON-restricted graphs showed some statistically significant alterations which could help explaining the clinical picture of the

PATs. On the other hand, it should be remarked that the ON-restricted graph analysis approach is unavoidably much influenced by prior assumptions and hypotheses (essentially for the choice of the ROIs forming the graph itself and for the choice of the metrics to be evaluated). However, the fact that some trends observed in the whole-brain graphs actually correspond to alterations of the ON-restricted graphs, is an encouraging fact and support the reliability of the obtained results.

ON-restricted graphs

Despite the high variability of the computed individual connectivity matrices, common patterns of connectivity could be identified and results of the global measurements performed on these graphs were generally in accord with the theoretical expectations. In particular, the Giant Component Size trend as a function of the density was observed to approach its maximum value with slightly lower slope with respect to the equivalent graphs with randomized topology: this can be interpreted as an implication of the non-trivial modular topology of the network, as it's often observed in brain functional networks. Another evidence pointing towards the same direction came from the comparison between the average Global Efficiency of "real" graphs and of randomized graphs, in which the latter was shown to be constantly higher. Another hallmark typical of these graphs is the so-called Small-World organization [94]: among the different metrics that could be adopted in order to evaluate this characteristic was chosen to use the one defined in [56] and results confirmed the hypothesis, showing an index substantially higher than 1.
By comparing the integral values of global measures (Giant Component size, normalized Global Efficiency, normalized Characteristic Path Length, normalized Modularity Coefficient, normalized Assortativity Coefficient and Small-Worldness) between the two groups, it was found a statistically significant alteration between the values of the Modularity coefficients ($p=0.019$, HC>PAT) and two noticeable trend in Global Efficiency and Characteristic Path lengths values ($p<0.053$, respectively PAT>HC and HC>PAT), though not formally significant. These observations (considering that Global Efficiency and Characteristic Path Length are essentially equivalent, as one measure represent the inverse of the other) suggest a generally higher level of macroscopic integration in the PATs graphs and a less pronounced modularity structure, with respect to those of the HCs group. The values measured for the Assortativity coefficient (in both PATs and HCs groups), though characterized by a large variability, showed a slight assortative behaviour at very small densities, progressively approaching zero. This could be attributable to the fact that many nodes were actually parts of single anatomical regions (e.g. the 5 regions of the Insula) and then were likely to have both strong mutual connections and similar "outer" connectivity; also, the fact that the considered graphs were generally ipsilateral

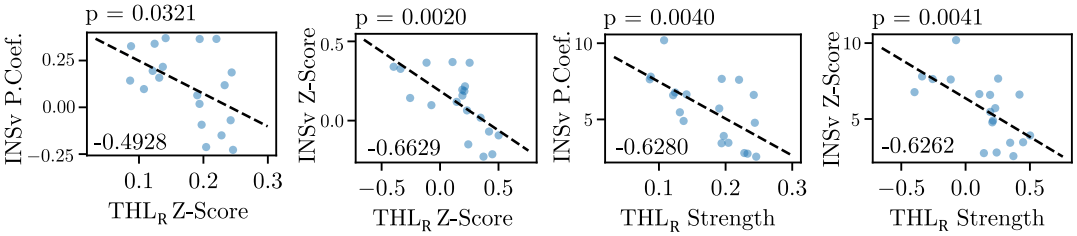

Figure 6.1: *Correlations between the individual values of some of the altered THL_R measures (Strength, Z-Score) and those of the $INSv_L$ (Participation coefficient, Z-Score), for the subjects of the PATs group.*

introduces a bias towards higher assortativity values (bilateral regions are likely to be strongly connected and simultaneously have similar connectivity distributions).
The analysis of topological properties of the graphs at a local (single-node) level highlighted some relevant differences between the two groups, among which the most significant involved the THL_R, the $aHIP_L$, the $INSv_L$ and the $CINa_L$; after correction for multiple comparisons, only two measures relative to the THL_R (Strength and Degree) survived and should be considered as statistically significant.
The THL_R of subjects in the PATs group appeared to be significantly more connected with other nodes, as Degree and Strength both indicates a general level of integration of the node in the network (it's worth noticing that a similar trend was observed in THL_L, hence seems to be a bilateral alteration). Furthermore, even though not strictly statistically relevant, the higher observed values of Participation coefficient and Z-Score of THL_R indicates that both the node centrality inside its module (*Sensory* module, according to [7]) and its intermodular connectivity were increased, making it a more *central* node in the network. On the other hand, both Participation coefficient and Z-Score of the $INSv_L$ (part of the *sensory* module) showed trends towards an opposite direction (reduced in PATs), so that it could be hypothesized some kind of compensation mechanisms involving the two nodes, at least at a modular level; this consideration is supported by the fact that some relevant correlations could be conserved between the altered measures of the two nodes, as shown in figure 6.1.

Results of the analysis conducted on the binarized versions of the same graphs, as expected, gave analogue results for most of the comparisons, though with a generally lower statistical significance; in this case the only alteration reaching a relevant significance (after correction for multiple comparisons) was the one involving the Degree of the THL_R. An exception was observed in the case of the Betweenness centrality and the Clustering coefficient of the $CINa_L$, for which p-values reached in the binarized version of the analysis were slightly higher than those of the weighted graphs.

The fact that weighted graphs, in the context of functional brain connectivity, with respect to their corresponding binary versions could potentially offer a richer description and, in particular, a greater sensitivity to pathological alterations is something which was already hypothesized [95] and our results seem to confirm it.
I should be also mentioned that with respect to the only other study the we are aware of, reporting a similar experimental attempt (the one from Esposito et Al. (2022) [6], previously introduced) a direct comparison of the results is not possible, as the ROIs chosen for building the graph are different (they didn't use an anatomical parcellation, but instead used spherical volumes in pre-defined positions); in particular, one of the main result they obtained regarded a ROI (4mm sphere) placed in the Anterior Piriform cortex, which wuold overlap with 3 different regions of the Brainettome Atlas, used for this work.

NBS

With the NBS analysis it was possible to explore differences between the two sets of graphs at a single-edge level. Results showed a cluster of statistically significant alteration (FWER corrected) mainly centered on the $THL_{R\text{-}L}$ (coherently with the results of the ON-restricted graph topology study) and strongly involving the $aHIP_R$, the INSai-a-v-p_R, the INSd-p_L and the $CINr_R$; furthermore, it was possible to quantitatively demonstrate that all the most altered connections (AS>1) involved the THL_R.

rsDPI algorithm

The results of the graph-analysis performed using the new ON ROIs did not differ from those obtained in the original version of the analysis. However, there are reasons to believe that the rsDPI intermediate additional step helped improving the quality of the data.
First of all, a significant average increase in raw-SNR after the application of the algorithm (considering the total group of subjects - PATs and HCs) was measured (+20.4%; $p < 0.0001$); however, it should be considered that this does not necessarily mean that an *effective*-SNR was increased as well, as the algorithm specifically targets the least correlated voxels of the ROI. On the other hand, the increased connectivity (on average) between the ROIs (i.e. increased group-average ROIs strength), was not obvious and could be considered a positive evidence as in general we expect a relatively high internal integration in the ON. Furthermore, the fact that such increase in connectivity was higher for the ROIs with lowest initial raw-SNR indicates that the algorithm mainly affects the most problematic regions, improving the coherence of the ROI volume on the functional data. The correlation observed between ROIs' average raw-SNR before the application of the algorithm and the relative raw-SNR variation, also represent an encouraging result in this direction.

These results indicates that the employment of an algorithm for ROIs finishing could help in those cases where problematic regions are studied (as the regions of the Piriform cortex and Orbitofrontal olfactory cortex were in our case) and a registration as precise as possible is required. In the particular case of our study, the fact that results of the graph-analysis weren't affected by the inclusion of this additional pre-processing step could mean that the registration of the ROIs onto the EPI was already very accurate, or at least not a source of macroscopic variability.

Whole-brain graphs

For what concerns the results of the analysis conducted on whole-brain weighted graphs, the considerations that can be made about the observed global measures' trends are similar to those of the ON-restricted graphs; some differences are observed in their higher values of normalized Modularity coefficients (attributable to the fact that it's a larger scale graph, likely to contain different specialized and functionally separated subnetworks).
The groups comparison of measures' integral values did not highlight any statistically significant alterations, neither at global nor at local level; however, while p-values of global comparisons were all far from the significance level, some of the local comparisons highlighted interesting trends of alterations (notice that in this case multiple-comparisons' correction was much more strict than in the ON-restricted case, due to the larger number of local measurements to be compared). In particular, some of the most relevant trends involved two sub-regions of the THL_R (mPFtha_r and tTtha_r of the Brainettome Atlas) and were consistent with the observations of the previous analyses (increased node centrality metrics: Degree, Participation Coefficient and Betweenness centrality).
The NBS analysis was repeated also on whole-brain networks, but no significant alteration was highlighted after FWER corrections.

Correlations with clinical scales

Some interesting correlations observed between the altered topological measures of ON-restricted graphs and clinical scores could help interpreting the results of this work, though keeping in mind that this last part was intended to be only an exploratory analysis.
In particular, the global Modularity coefficient (reduced in PATs) was observed to be positively correlated with the results of the olfactory assessment performed with the Sniffin' Sticks (in particular with olfactory threshold - $\rho = 0.52$; $p = 0.027$ - and total score - $\rho = 0.59;$, $p = 0.0095$); a plausible hypothesis could be that a less pronounced modular organization penalizes the ON of the subjects in the PATs group, as its ability of segregating specific

activities is less efficient; similar interpretations regarding altered Modularity in functional connectivity networks are actually quite common, as evidences of correlation between the level of functional segregation and various types of cognitive decline exists in literature (e.g. [96, 97, 98]).
On the other hand, different indexes of THL_R's node centrality (Degree, Strength) were negatively correlated with short-term verbal memory tests (AVLT (IMM) - $\rho = -0.59$, $p = 0.015$ - Obj. Naming - $\rho = -0.59$, $p = 0.015$). A possible speculative interpretation of these correlations could be built around the fact that the Thalamus is not directly connected to primary Olfactory structures, but instead is involved in higher processing (perception) of the odorant information together with the Orbito-frontal cortex [99]. Furthermore, considering that one of the most important contributions to the alteration of the overall THL_R Strength came from is connection with the $pHIP_L$ (as shown by the NBS), and considering that the hippocampal-thalamic interactions represent an important system for episodic memory [100], a dysfunctional thalamic connectivity might be responsible for the impact on memory.

Conclusions and future perspectives

In this work an experimental attempt of investigating the brain functional-connectivity characteristics of a group of patients suffering from persistent COVID-19-related neurological symptoms was presented. In particular, the major focus was on the study of the connectivity patterns of the core regions of the ON, made possible by the availability of high-quality rs-fMRI data. Among the three proposed approaches, the most significant results were found with the graph-theoretical modelling of data. In fact, from the comparison of the ON-restricted connectivity graphs of patients with those obtained from a matched control group of healthy subjects, an altered topological organization emerged, quantifiable in reduced values of global Modularity coefficient and a hyper-connection of the right Thalamus. Furthermore, by integrating these results with individual clinical scores it was possible to implement an exploratory correlation analysis, which helped the interpretation of the experimental observations.
The others two approaches implemented (*group-ICA* and *seed-based* analyses) did not highlight any statistically relevant alteration between the two groups, meaning that no significant alterations was detectable in the connections between the core ON regions and the rest of the brain (not contradicting the other results, as the thalamus was not part of the core ON areas).
The most important intrinsic limitation of the presented study is the relatively small number of subjects included. A great variability in fact is typically observed in the patterns of spontaneous correlations between brain activations, lowering the theoretically available signal-to-noise ratio. Furthermore, the fact that the ON-core regions are located in areas often affected by distortions, artifacts or signal-dropout, may have contributed to reduce the accuracy of the estimates. However, as this was the first reported study to provide a whole-brain graph-based analysis with a long-COVID-19 patients group, could eventually represent a starting point for future works.
Regarding the techniques adopted for the data analysis, it must be considered that the graph-based approach is implicitly based on a series of a-priori assumptions, which of course have an influence on the obtained results, such as the choice of the anatomical parcellation for nodes definitions, the definition

of functional connectivity metrics and the choice of the graph-topological measures to be evaluated (though from this point of view, all the choices made for this study were taken in accordance with the most reliable references found in literature). On the other hand, approaches such as the ICA-based techniques require few initial assumptions compared to graph analysis, but the sensitivity they offer for local and potentially subtle alterations is generally lower.
From a more general point of view it could be also considered that all these methods rely on the fundamental assumption of a static-functional connectivity, whereas some recent findings have suggested that assuming a dynamic behaviour of the spatial connectivity-patterns could offer a more appropriate description of brain resting-state observed activity [25, 101, 102]. Attempts to model this kind of dynamics in a graph-theoretical framework already have been reported, offering interesting results. The application of such models and the comparison of the results with those obtained with standard approaches could be a matter for future work, given the availability of relatively long rs-fMRI sequences with a good temporal resolution.

Bibliography

[1] P. Boaventura, S. Macedo, F. Ribeiro, S. Jaconiano, P. Soares, *Post-COVID-19 Condition: Where Are We Now?*. Life. **2022** Mar; 12(4): 517.

[2] M. S. Xydakis, M. W. Albers, E. H. Holbrook, et Al., *Post-viral effects of COVID-19 in the olfactory system and their implications*. Lancet Neurol. **2021** Sep; 20(9): 753-761.

[3] D. Yildirim, S. G. Kandemirli, D. E. Tekcan Sanli, O. Akinci, A. Altundag, *A Comparative Olfactory MRI, DTI and fMRI Study of COVID-19 Related Anosmia and Post Viral Olfactory Dysfunction*. Acad. Radiol. **2022** Jan; 29(1): 31-41.

[4] G. Douaud, S. Lee, F. Alfaro-Almagro, C. Arthofer, C. Wang, P. McCarthy, F. Lange, J. L. R. Andersson, L. Griffanti, E. Duff, S. Jbabdi, B. Taschler, P. Keating, A. M. Winkler, R. Collins, P. M. Matthews, N. Allen, K. L. Miller, T. E. Nichols, S. M. Smith, *SARS-CoV-2 is associated with changes in brain structure in UK Biobank*. Nature. **2022** Mar; 604: 697-707.

[5] I. I. Ismail, K. A. Gad, *Absent Blood Oxygen Level-Dependent Functional Magnetic Resonance Imaging Activation of the Orbitofrontal Cortex in a Patient With Persistent Cacosmia and Cacogeusia After COVID-19 Infection*. JAMA Neurol. **2021** May; 78(5): 609-610.

[6] F. Esposito, M. Cirillo, R. De Micco, G. Caiazzo, M. Siciliano, A. G. Russo, C. Monari, N. Coppola, G. Tedeschi, A. Tessitore, *Olfactory loss and brain connectivity after COVID-19*. Hum. Brain Mapp. **2022** Apr; 43(5): 1548-1560.

[7] T. Campbell Arnold, Y. You, M. Ding, X. Zuo, I. de Araujo, W. Li, *Functional Connectome Analyses Reveal the Human Olfactory Network Organization*. **2020** Jul; 7(4): 1–14.

[8] T. Murta, L. Hu, T.M. Tierney, U.J. Chaudhary, M.C. Walker, D.W. Carmichael, P. Figueiredo, L. Lemieuxa, *A study of the electro-haemodynamic coupling using simultaneously acquired intracranial EEG and fMRI data in humans*. Neuroimage. **2016** Nov; 142: 371–380.

[9] S. A. Huettel, A. W. Song, G. McCarthy, *Functional Magnetic Resonance Imaging, 3rd edition*. Sunderland (USA), Sinauer Associates, Inc. (2014).

[10] C. S. Roy, C. S. Sherrington, *On the Regulation of the Blood-supply of the Brain.* J Physiol. **1890** Jan; 11(1-2): 85-108.

[11] Al C. Ngai, K. R. Ko, S. Morii, H. R. Winn, *Effect of sciatic nerve stimulation on pial arterioles is rats.* J. Physiol. **1988** Jan; 254(1-2): 133-139.

[12] A. R. Nippert, K. R. Biesecker, E. A. Newman, *Mechanisms Mediating Functional Hyperemia in the Brain.* Neuroscientist **2018** Feb; 24: 73-83.

[13] P. T. Fox, M. E. Raichle, *Focal physiological uncoupling of cerebral blood flow and oxidative metabolism duvring somatosensory stimulation in human subjects.* Proc. Natl. Acad. Sci. US **1986** Feb; 83: 1140-1144.

[14] P. T. Fox, M. E. Raichle, *Nonoxidative glucose consumption during focal physiologic neural activity.* Science **1988** Jul; 241: 462-464.

[15] K. R.Thulborn, J. C. Waterton, P. M. Matthews, G. K. Radda, *Oxygenation dependence of the transverse relaxation time of water protons in whole blood at high field.* Biochimica et Biophysica Acta (BBA) **1982** Feb; 714: 265-270.

[16] S. Ogawa, T. M. Lee, A. S. Nayak, P. Glynn, *Oxygenation-sensitive contrast in magnetic resonance image of rodent brain at high magnetic fields.* Magn. Reson. Med. **1990** Apr; 14: 68-78.

[17] S. Ogawa, T. M. Lee, A. R. Kay, D. W. Tank, *Brain magnetic resonance imaging with contrast dependent on blood oxygenation.* Proc. Natl. Acad. Sci. USA. **1990** Dec; 87: 9868–9872.

[18] B. B. Zandbelt, T. E. Gladwin, M. Raemaekers, M. Buuren, S. F.Neggers, R. S.Kahn, N. F. Ramsey, M. Vink, *Within-subject variation in BOLD-fMRI signal changes across repeated measurements: Quantification and implications for sample size.* NeuroImage. **2008** Aug; 42(1): 196-206.

[19] S. H. Faro, F. B. Mohamed, *BOLD fMRI: A Guide to Functional Imaging for Neuroscientists.* New York (USA), Springer. (2010).

[20] P. Jezzard, P. M. Matthews, S. M. Smith, *Functional MRI: an introduction to methods.* (UK), Oxford University Press. (2001).

[21] D. K. Sodickson, *Tailored SMASH image reconstructions for robust in vivo parallel MR imaging.* Magn. Reson. Med. **2000** Aug; 44(2): 243-51.

[22] K P Pruessmann, M. Weiger, M. B. Scheidegger, P. Boesiger, *SENSE: sensitivity encoding for fast MRI.* Magn. Reson. Med. **1999** Nov; 42(5): 952-62.

[23] D. A. Feinberg, K. Setsompop, *Ultra-fast MRI of the human brain with simultaneous multi-slice imaging.* J. Magn. Reson. **2013** Apr; 229: 90-100.

[24] P. A. Bandettini, *Twenty years of functional MRI: The science and the stories.* NeuroImage. **2012** Aug; 62(2): 575-588.

[25] E. A. Allen, E. Damaraju, S. M. Plis, E. B. Erhardt, T. Eichele, V. D. Calhoun, *Tracking Whole-Brain Connectivity Dynamics in the Resting State*. Cerebral Cortex. **2014** Mar; 24: 663–676.

[26] J. S. Damoiseaux , S. Rombouts, F. Barkhof, P. Scheltens, C. J. Stam, S. M. Smith, C. F. Beckmann, *Consistent resting-state networks across healthy subjects*. Proc. Natl. Acad. Sci. **2006** Sep; 103(37): 13848-13853.

[27] V. Fonov, A. C. Evans, K. Botteron, C. R. Almli, R. C. McKinstry, D. L. Collins, *Unbiased average age-appropriate atlases for pediatric studies*. NeuroImage. **2011** Jan; 54(1) 313-327.

[28] K. Van Dijk, M. Sabuncu, R. L. Buckner, *The Influence of Head Motion on Intrinsic Functional Connectivity MRI*. NeuroImage. **2012** Jan; 59(1): 431–438.

[29] C. Triantafyllou, R. D. Hoge, L. L. Wald, *Effect of spatial smoothing on physiological noise in high-resolution fMRI*. NeuroImage. **2006** Aug ; 32(2): 551-558.

[30] M. J. Lowe, B. J. Mock, J. A. Sorenson, *Functional connectivity in single and multislice echoplanar imaging using resting-state fluctuations*. NeuroImage. **1998** Feb; 7(2): 119-151.

[31] C. F. Beckmann, *Modelling with independent components*. NeuroImage. **2012** Aug; 62(2): 891-901.

[32] A. J. Bell, T. J. Sejnowski, *An information-maximization approach to blind separation and blind deconvolution*. Neural Comput. **1995** Nov; 7(6): 1129-59.

[33] C. M. Bishop, *Pattern Recognition and Machine Learning*. (USA), Springer-Verlag. (2006).

[34] A. Hyvärinen, E. Oja, *Independent Component Analysis: Algorithms and Applications*. Neural Networks. **2000**; 13(4-5): 411-430.

[35] M. J. McKeown, S. Makeig, G. G. Brown, T. P. Jung, S. S. Kindermann, A. J. Bell, T. J. Sejnowski, *Analysis of fMRI data by blind separation into independent spatial components*. Hum. Brain Mapp. **1998**; 6(3): 169-88

[36] C. F. Beckmann, S. M. Smith, *Probabilistic Independent Component Analysis for Functional Magnetic Resonance Imaging*. IEEE Trans. Med. Imaging. **2004** Feb; 23(2): 137-52.

[37] L. Griffanti, G. Salimi-Khorshidi, C. F. Beckmann et Al., *ICA-based artefact removal and accelerated fMRI acquisition for improved resting state network imaging*. NeuroImage. **2014**; 95: 232–247.

[38] C. Rummel, R. K. Verma, V. Schöpf, E. Abela, M. Hauf, J. F. Zapata Berruecos, R. Wiest, *Time course based artifact identification for independent components of resting-state fMRI*. Front. Hum. Neurosci. **2013** May; 7.

[39] R. E. Kelly, G. S. Alexopoulos, Z. Wang, F. M. Gunning, C. F. Murphy, S. Shizuko Morimoto, D. Kanellopoulos, Z. Jia, K. O. Lim, M. J. Hoptman, *Visual inspection of independent components: defining a procedure for artifact removal from fMRI data.* J. Neurosci. Methods. **2010** Jun; 189(2): 233-45.

[40] L. Griffantia, G. Douauda, J. Bijsterboscha, S. Evangelisti et Al., Hand classification of fMRI ICA noise components. NeuroImage. **2017**; 154: 188-205.

[41] G. Salimi-Khorshidi, G. Douaud, C. F. Beckmann, M. F. Glasser, L. Griffanti, S. M. Smith, *Automatic denoising of functional MRI data: combining independent component analysis and hierarchical fusion of classifiers.* NeuroImage. **2014** Apr; 90: 449-68.

[42] L. Nickerson, S. M. Smith, D. Öngür, C. F. Beckmann, *Using Dual Regression to Investigate Network Shape and Amplitude in Functional Connectivity Analyses.* Front. Hum. Neurosci. **2017**; 11: 115.

[43] C. F. Beckmann, C. E. Mackay, N. Filippini, S. M. Smith, *Group comparison of resting-state FMRI data using multi-subject ICA and dual regression.* NeuroImage. **2009** Jul; 47: S148.

[44] Z. Shehzad, A. M. Clare Kelly, P. T. Reiss, D. G. Gee, K. Gotimer, L. Q. Uddin, S. H. Lee, D. S. Margulies, A. K. Roy, B. B. Biswal, E. Petkova, F. X. Castellanos, M. P. Milham, *The resting brain: unconstrained yet reliable.* Cereb. Cortex. **2009** Oct; 19(10): 2209-29.

[45] D. M. Cole, S. M. Smith, C. F. Beckmann, *Advances and pitfalls in the analysis and interpretation of resting-state FMRI data.* Front. Syst. Neurosci. **2010** Apr; 4(8).

[46] X.Shen, F.Tokoglu, X.Papademetris, R.T. Constable, *Groupwise whole-brain parcellation from resting-state fMRI data for network node identification.* NeuroImage. **2013** Nov; 82: 403-415.

[47] Y. Hu, X. Li, L. Wang, B. Han, S. Nie, *T-distribution stochastic neighbor embedding for fine brain functional parcellation on rs-fMRI.* Brain Research Bulletin. **2020** Sep; 162: 199-207.

[48] K. J. Friston,*Functional and effective connectivity: a review.* Brain Connect. **2011**; 1(1): 13–36.

[49] Z. S. Saad, S. J. Gotts, K. Murphy, G. Chen, H. Joon Jo, A. Martin, R. W. Cox, *Trouble at rest: how correlation patterns and group differences become distorted after global signal regression.* Brain Connect. **2012**; 2(1): 25-32.

[50] R. Mohanty, W. A. Sethares, V. A. Nair et Al., *Rethinking Measures of Functional Connectivity via Feature Extraction.* Sci. Rep. **2020** Jan; 10(1): 1298.

[51] J. Wang, X. Zuo, Y. He, *Graph-based network analysis of resting-state functional MRI.* Front. Syst. Neurosci. **2010** Jun; 4.

[52] M. Rubinov, O. Sporns, *Complex network measures of brain connectivity: Uses and interpretations*. NeuroImage. **2012** Sep; 52(1): 1059-1069.

[53] D. Watts, S. Strogatz, *Collective dynamics of 'small-world' networks*. Nature. **1998** Jun; 393: 440–442.

[54] V. D. Blondel, J. L. Guillaume, R. Lambiotte, E. Lefebvre, *Fast unfolding of communities in large networks*. J. Stat. Mech. **2008** Oct; P10008.

[55] G. Tononi, O. Sporns, G. M. Edelman, *A measure for brain complexity: Relating functional segregation and integration in the nervous system*. Proc. Natl. Acad. Sci. USA. **1994** May; 91: 5033-5037.

[56] M. D. Humphries, K. Gurney, *Network 'Small-World-Ness': A Quantitative Method for Determining Canonical Network Equivalence*. Proc. Natl. Acad. Sci. USA. **2008** Apr; 3(4): e0002051.

[57] M. P. van den Heuvel, S. C. de Lange, A. Zalesky, C. Seguin, B. T. Thomas Yeo, R. Schmidt, *Proportional thresholding in resting-state fMRI functional connectivity networks and consequences for patient-control connectome studies: Issues and recommendations*, NeuroImage. **2017** May; 152: 437-449.

[58] M. N. Hallquist, F. G. Hillary, *Graph theory approaches to functional network organization in brain disorders: A critique for a brave new small-world*. Network Neuroscience. **2018** Apr; 3(1): 1–26.

[59] S. Firestein, *How the olfactory system makes sense of scents*. Nature. **2001** Sep; 413(6852): 211-8.

[60] I. Croy, T. Hummel, *Olfaction as a marker for depression*. J. Neurol. **2017** Apr; 264(4): 631-638.

[61] E. T. Rolls, *The orbitofrontal cortex, food reward, body weight and obesity*. Soc. Cogn. Affect. Neurosci. **2021** Apr; nsab044.

[62] L. T. Seabrook, S. L. Borgland, *The orbitofrontal cortex, food intake and obesity*. J. Psychiatry Neurosci. **2020** Sep; 45(5): 304-312.

[63] J. Seubert, J. Freiherr, J. Djordjevic, J. N. Lundström, *Statistical localization of human olfactory cortex*. NeuroImage. **2012** Oct; 66: 333-342.

[64] M. J. Tobia, Q. X. Yang, P. Karunanayaka, *Intrinsic intranasal chemosensory brain networks shown by resting-state functional MRI*. NeuroReport. **2016** Mar; 27: 527-531.

[65] C. Georgiopoulos, S. T. Witt, S. Hallerc, N. Dizdar, H. Zachrisson, M. Engströmb, E. Larssond, *A study of neural activity and functional connectivity within the olfactory brain network in Parkinson's disease*. NeuroImage. **2019** Jul; 23: 101946.

[66] J. Lu, N. Testa, R. Jordan, R. Elyan, S. Kanekar, J. Wang, P. Eslinger, Q. X. Yang, B. Zhang, P, R. Karunanayaka, *Functional Connectivity between the Resting-State Olfactory Network and the Hippocampus in Alzheimer's Disease*. Brain Sci. **2019** Nov; 9: 338.

[67] A. Nalbandian, K. Sehgal, A. Gupta, et Al., *Post-acute COVID-19 syndrome*. Nat Med. **2021** Apr; 27(4): 601-615.

[68] J. K. Logue, N. M. Franko, D. J. McCulloch, et Al., *Sequelae in Adults at 6 Months After COVID-19 Infection*. JAMA Netw Open. **2021** Feb; 4(2): e210830.

[69] G. Moonis, R. Mitchell, B. Szeto, A. K. Lalwani, *Radiologic Assessment of the Sinonasal Tract, Nasopharynx and Mastoid Cavity in Patients with SARS-Cov-2 Infection Presenting with Acute Neurological Symptoms*. Ann. Otol. Rhinol. Laryngol. **2021** Nov; 130(11): 1228-1235.

[70] S. G. Kandemirli, A. Altundag, D. Yildirim, D. E. Tekcan Sanli, O. Saatci, *Olfactory Bulb MRI and Paranasal Sinus CT Findings in Persistent COVID-19 Anosmia*. Acad. Radiol. **2021** Jan; 28(1): 28-35.

[71] D. Güllmar, T. Seeliger, H. Gudziol, U. K. M. Teichgräber, J. R. Reichenbach, O. Guntinas-Lichius, T. Bitter, *Improvement of olfactory function after sinus surgery correlates with white matter properties measured by diffusion tensor imaging*. Neuroscience. **2017** Sep; 360: 190-196.

[72] J. Wang, P. J. Eslinger, R. L. Doty, E. K. Zimmerman, R. Grunfeld, X. Sun, M. D. Meadowcroft, J. R. Connor, J. L. Price, M. B. Smith, Q. X. Yang, *Olfactory deficit detected by fMRI in early Alzheimer's disease*. Brain Res. **2010** Oct; 1357: 184-194.

[73] G. Kobal, T. Hummel, B. Sekinger, S. Barz, S. Roscher, S. Wolf, *"Sniffin' sticks": screening of olfactory performance*. Rhinology. **1996** Dec; 34(4): 222-226.

[74] R. C. Oldfield, *The assessment and analysis of handedness: The Edinburgh inventory*. Neuropsychologia. **1971** Mar; 9(1): 97-113.

[75] Z. S. Nasreddine, N. A. Phillips, V. Bédirian, S. Charbonneau, V. Whitehead, I. Collin, J. L. Cummings, H. Chertkow, *The Montreal Cognitive Assessment, MoCA: a brief screening tool for mild cognitive impairment*. J. Am. Geriatr. Soc. **2005** Apr; 53(4): 695-9.

[76] M. Jenkinson, P. Bannister, J. M. Brady, S. M. Smith, *Improved Optimisation for the Robust and Accurate Linear Registration and Motion Correction of Brain Images*. NeuroImage. **2002** Oct; 17(2): 825-841.

[77] S. M. Smith, M. Jenkinson, M. W. Woolrich, C. F. Beckmann, T. E. J. Behrens, H. Johansen-Berg, P. R. Bannister, M. De Luca, I. Drobnjak, D. E. Flitney, R. Niazy, J. Saunders, J. Vickers, Y. Zhang, N. De Stefano, J. M. Brady, P. M. Matthews, *Advances in functional and structural MR image analysis and implementation as FSL*. NeuroImage. **2004**; 23(S1): 208-219.

[78] S. M. Smith, *Fast robust automated brain extraction*. Hum. Brain Mapp. **2002** Nov; 17(3): 143-155.

[79] A. A. S. Alahmadi, *Effects of different smoothing on global and regional resting functional connectivity*. Neuroradiology. **2021** Jan; 63(1): 99-109.

[80] FMRIB Software Library v6.0 guide. (accessed July 4th, 2022) `fsl.fmrib.ox.ac.uk/fsl/fslwiki/MELODIC`.

[81] FMRIB Software Library v6.0 guide - randomise tool. (accessed July 4th, 2022) `fsl.fmrib.ox.ac.uk/fsl/fslwiki/Randomise`.

[82] A. M. Winkler, G. R. Ridgway, M. A. Webster, S. M. Smith, T. E. Nichols, *Permutation inference for the general linear model*. NeuroImage. **2014** May; 92: 381-397.

[83] FreeSurfer software suite website, (accessed May 29th, 2022), `surfer.nmr.mgh.harvard.edu/`.

[84] L. Fan, H. Li, J. Zhuo, Y. Zhang, J. Wang, L. Chen, Z. Yang, C. Chu, S. Xie, A. R. Laird, P. T. Fox, S. B. Eickhoff, C. Yu, T. Jiang, *The Human Brainnetome Atlas: A New Brain Atlas Based on Connectional Architecture*. Cereb. Cortex. **2016** Aug; 26(8): 3508-3526.

[85] J. H. Wang, X. N. Zuo, S. Gohel, M. P. Milham, B. B. Biswal, Y. He, *Graph Theoretical Analysis of Functional Brain Networks: Test-Retest Evaluation on Short- and Long-Term Resting-State Functional MRI Data*. Proc. Natl. Acad. Sci. USA. **2011** Jul; 6(7): e21976.

[86] Brain Connectivity Toolbox reference guide, (accessed July 4th, 2022) `sites.google.com/site/bctnet/`

[87] S. Maslov, K. Sneppen, *Specificity and Stability in Topology of Protein Networks*. Science. **2002** May; 296(5569): 910-3.

[88] F. J. Massey, *The Kolmogorov-Smirnov Test for Goodness of Fit*. J. Am. Stat. Assoc. **1951**; 46(253): 68–78.

[89] E. Varangis, C. G. Habeck, Q. R. Razlighi, Y. Stern, *The Effect of Aging on Resting State Connectivity of Predefined Networks in the Brain*. Front. Aging Neurosci. **2019** Sep; 11: 234.

[90] Y. Benjamini, H. Yosef, *Controlling the false discovery rate: a practical and powerful approach to multiple testing*. J. R. Stat. Soc. **1995**; 57(1): 289–300.

[91] A. Zalesky, A. Fornito, E. T. Bullmore, *Network-based statistic: Identifying differences in brain networks*. NeuroImage. **2010** Dec; 53(4): 1197-1207.

[92] NBS Reference Manual V1.2, (accessed July 4th, 2022) `www.nitrc.org/projects/nbs/`

[93] M. Xia, J. Wang, Y. He *BrainNet Viewer: A Network Visualization Tool for Human Brain Connectomics*. Proc. Natl. Acad. Sci. USA. **2013** Jul; 8(7): e68910.

[94] O. Sporns, C. J. Honey, *Small worlds inside big brains*. Proc. Natl. Acad. Sci. USA. **2006** Dec; 103(51): 19219-19220.

[95] D. E. Meskaldji, E. Fischi-Gomez, A. Griffa, P. Hagmann, S. Morgenthaler, J. P. Thiran, *Comparing connectomes across subjects and populations at different scales*. NeuroImage. **2013** Oct; 80: 416-25.

[96] X. Chen, J. Necus, L. R. Peraza, R. Mehraram, Y. Wang, J. T. O'Brien, A. Blamire, M. Kaiser, J. P. Taylor, *The functional brain favours segregated modular connectivity at old age unless affected by neurodegeneration*. Commun. Biol. **2021** Aug; 4(1): 973.

[97] M. Ewers, Y. Luan, L. Frontzkowski, J. Neitzel, A. Rubinski, M. Dichgans, J. Hassenstab, *Alzheimer's Disease Neuroimaging Initiative and the Dominantly Inherited Alzheimer Network. Segregation of functional networks is associated with cognitive resilience in Alzheimer's disease*. Brain. **2021** Aug; 144(7): 2176-2185.

[98] M. Y. Chan, D. C. Park, N. K. Savalia, S. E. Petersen, G. S. Wig, *Decreased segregation of brain systems across the healthy adult lifespan*. Proc. Natl. Acad. Sci. USA. **2014** Nov; 111(46): E4997-E5006.

[99] L. Sela, Y. Sacher, C. Serfaty, Y. Yeshurun, N. Soroker, N. Sobel, *Spared and Impaired Olfactory Abilities after Thalamic Lesions*. J. Neurosci. **2009** Sep; 29(39): 12059-12069.

[100] J. P. Aggleton, S. M. O'Mara, S. D. Vann, N. F. Wright, M. Tsanov, J. T. Erichsen, *Hippocampal-anterior thalamic pathways for memory: uncovering a network of direct and indirect actions*. Eur. J. Neurosci. **2010** Jun; 31(12): 2292-307.

[101] M. Filippi, E. G. Spinelli, C. Cividini, F. Agosta, *Resting State Dynamic Functional Connectivity in Neurodegenerative Conditions: A Review of Magnetic Resonance Imaging Findings*. Front. Neurosci. **2019** Jun; 13: 657.

[102] S. S. Menon, K. Krishnamurthy, *A Comparison of Static and Dynamic Functional Connectivities for Identifying Subjects and Biological Sex Using Intrinsic Individual Brain Connectivity*. Sci. Reports. **2019** Apr; 9: 5729.